

HARDWARE AND SOFTWARE APPROACHES TO INCREASING  
ACCESSIBILITY OF NUCLEAR MAGNETIC RESONANCE IMAGING AND  
SPECTROSCOPY

A Dissertation

by

TRAVIS JAMES CARRELL

Submitted to the Graduate and Professional School of  
Texas A&M University  
in partial fulfillment of the requirements for the degree of

DOCTOR OF PHILOSOPHY

Chair of Committee,	Mary Preston McDougall
Committee Members,	Steven Wright
	Mariëlle Engelen
	Alexandra Walsh
Head of Department,	Mike McShane

May 2022

Major Subject: Biomedical Engineering

Copyright 2022 Travis James Carrell

## ABSTRACT

This work presents a number of projects for increasing accessibility to magnetic resonance imaging and magnetic resonance spectroscopy through hardware and software approaches. First, the feasibility of dynamic  $^{31}\text{P}$  MR spectroscopy for metabolic studies was assessed using a 1.0T extremity scanner (lower than clinical fields, less expensive) retrofitted with broadband capabilities and  $^{31}\text{P}$  array and transmit coil technologies. Metabolic parameters were evaluated in a healthy volunteer over the course of a foot flexion protocol. The second hardware approach involved creating a switchable three-element, triple-tuned array to demonstrate the range of nuclei over which the method could be applied. To further broadband accessibility, a multi-channel broadband receiver was evaluated for its utility for increasing the overall channel count capabilities with which single and multi-nuclear studies could be performed. The benefit of its data handling and reduction capabilities were demonstrated over the previous digitization card. Third, a longitudinally translatable 32-channel coil array and associated preamplifier unit were developed for the investigation of the potential for single-shot volume imaging. This approach, previously not investigated due to hardware limitations, was utilized to investigate the ultrafast MRI theory for a 32-ring/row by 32-element array. Finally, as a software approach to accessibility to multinuclear NMR, an open-source multi-channel magnetic resonance spectroscopy graphical user interface was established to utilize literature-based multi-channel combinations for improving data combination while minimizing spectral distortion. This tool can assist the user in selecting a combination

technique based on the available data for characterizing the system, such as additional  $^1\text{H}$  unsuppressed water scans, noise scans, or channel SNR. These projects present a step forward in increasing the accessibility to multi-nuclear magnetic resonance imaging and magnetic resonance spectroscopy.

## ACKNOWLEDGEMENTS

I would like to thank Dr. Mary McDougall, who served as both my committee chair and advisor and who was always willing to go to bat for me. Thank you for your guidance and support throughout the course of my tenure within graduate school and for allowing me to pursue teaching opportunities. I admire your teaching style and hope to emulate that in the classroom. I would also like to thank Dr. Steven Wright for his guidance within my research projects and learning opportunities through his classes. Additionally, I would like to acknowledge my remaining committee members, Dr. Mariëlle Engelen and Dr. Alexandra Walsh, who have provided me this opportunity to pursue my degree.

I would like to recognize my co-workers in the Nuclear Magnetic Resonance Laboratory, who were always a source of encouragement and those who I could go to bounce ideas off. I will always cherish the friendship of my lab mates, Matthew Wilcox, Romina del Bosque, Edith Valle Touche, and Joseph Busher.

I would like to acknowledge my family for their continued love, support, and encouragement throughout my entire life. Words cannot express how thankful that I am for y'all.

Lastly, I want to thank my wife, Rae Ann, for going through this journey with me. You have been a constant throughout all of the ups and downs of graduate school. Your love and support have helped me to accomplish this. I love you, Rae.

## CONTRIBUTORS AND FUNDING SOURCES

### **Contributors**

This work was supervised by a dissertation committee consisting of Dr. Mary McDougall and Dr. Alexandra Walsh of the Department of Biomedical Engineering, Dr. Mariëlle Engelen of the Department of Health and Kinesiology, and Dr. Steven Wright who maintains a joint appointment in the Department of Electrical and Computer Engineering and the Department of Biomedical Engineering.

The four-element receive array used in Chapter II.1 was built by Minyu Gu. The three-element triple-tuned array developed in Chapter II.2 was constructed in conjunction with Dr. Romina del Bosque. All data for Chapter II.3 was gathered with the aid from collaborators at the MRSL – Courtney Bauer and Dennis Kim. All imaging data for Chapter III.4.2 was gathered with aid from Dr. John C. Bosshard. The 1.0T magnet, Ultraview receiver, and Pentek receiver were all resources of the MRSL lab. All other dissertation work was conducted independently.

### **Funding Sources**

Graduate study was supported in part by research and teaching assistantships from Texas A&M University. Financial support for the research of Chapter II.1 and Chapter IV was provided by the Texas A&M University Seed Grant program. The acquisition of the 1.0T magnet and Ultraview receiver by Dr. Wright were supported from a grant from Samsung. Financial support for the research of Chapter III was provided by Ultrafast Imaging, LLC. The contents of this work are solely the responsibility of the authors and do not necessarily represent the views of these funding sources.

## NOMENCLATURE

MR	Magnetic resonance
MRI	Magnetic resonance imaging
MRSI	Magnetic resonance spectroscopic imaging
MRS	Magnetic resonance spectroscopy
NMR	Nuclear magnetic resonance
FID	Free induction decay
RF	Radiofrequency
SMA	SubMiniature version A connector type
BNC	Bayonet Neill-Concelman connector type
DC	Direct current
$Q_{l/u}$	Loaded/unloaded quality factor
T1	Spin-lattice/longitudinal relaxation time
T2	Spin-spin/transverse relaxation time
TE	Echo time
TR	Repetition time
Tx	Transmit
Rx	Receive
MRS�	Magnetic Resonance and Systems Laboratory
PCr	Phosphocreatine
Pi	Inorganic phosphate

ATP	Adenosine triphosphate
W	Watts
dB	Decibels
GUI	Graphical user interface
$\lambda$	Wavelength
$\omega$	Radial frequency
$B_0$	Static magnetic flux density
$B_1$	RF magnetic flux density
$B_1^+/B_1^-$	Excitation/reception RF magnetic flux density
BW	Bandwidth
DMA	Direct memory access
FID	Free induction decay
ADC	Analog-to-digital converter
TTL	Transistor-transistor logic
DDC	Digital down converter
I/Q	In-phase/quadrature signals
$F_s$	Sampling frequency

## TABLE OF CONTENTS

	Page
ABSTRACT .....	ii
ACKNOWLEDGEMENTS .....	iv
CONTRIBUTORS AND FUNDING SOURCES.....	v
NOMENCLATURE.....	vi
TABLE OF CONTENTS .....	viii
LIST OF FIGURES.....	xi
LIST OF TABLES .....	xv
CHAPTER I INTRODUCTION .....	1
I.1 Background and Motivation .....	1
I.1.1 Nuclear Magnetic Resonance.....	1
I.1.2 Radiofrequency Coils.....	4
I.1.3 Magnetic Resonance Spectroscopy & Imaging .....	7
I.1.4 Data Sampling.....	11
I.1.5 Processing of Array Data .....	13
I.1.6 MR Accessibility and Motivation .....	14
1.2 Specific Aims and Dissertation Organization .....	17
1.3 Dissertation Style .....	22
CHAPTER II RADIOFREQUENCY COILS FOR MULTI-NUCLEAR SPECTROSCOPY .....	23
II.1 Assessing the Feasibility of Dynamic <sup>31</sup> P MR Spectroscopy for Metabolic Studies with a 1.0T Extremity Scanner.....	23
II.1.1 Synopsis.....	23
II.1.2 Introduction.....	24
II.1.3 Methods .....	25
II.1.4 Results.....	36
II.1.5 Discussion.....	42
II.1.6 Conclusion .....	44



II.2 A Three-Element Triple-Tuned Array Implemented with Switchable Matching and Tuning.....	46
II.2.1 Synopsis.....	46
II.2.2 Introduction.....	46
II.2.3 Methods .....	47
II.2.4 Results and Discussion .....	49
II.2.5 Conclusion.....	51
II.3 Characterization of a Multi-channel Receiver for Broadband System.....	52
II.3.1 Synopsis.....	52
II.3.2 Methods .....	53
II.3.3 Results and Discussion .....	56
II.3.4 Conclusion.....	61
 CHAPTER III LONGITUDINALLY TRANSLATABLE 32-CHANNEL COIL RING AND PREAMPLIFIER UNIT FOR INVESTIGATION OF 32X32 VOLUME FAST MRI DATA ACQUISITION.....	 62
III.1 Synopsis .....	62
III.2 Introduction.....	63
III.3 Methods.....	63
III.4 Results and Discussion.....	74
III.5 Conclusion.....	85
 CHAPTER IV MULTI-CHANNEL MAGNETIC RESONANCE SPECTROSCOPY GUI (MCMRSGUI) .....	 87
IV.1 Synopsis .....	87
IV.2 Introduction.....	88
IV.3 Methods.....	90
IV.3.1 Data Loading.....	91
IV.3.2 Preprocessing .....	92
IV.3.3 Multi-channel Combination .....	92
IV.4 Results.....	96
IV.5 Discussion.....	100
IV.6 Conclusion .....	101
IV.7 Notes .....	102
 CHAPTER V CONCLUSION AND FUTURE WORK.....	 103
V.1 Contributions to the Field.....	103
V.2 Future Work .....	105
 REFERENCES .....	 108
 APPENDIX A .....	 123

A. 1 Protocol for $^{31}\text{P}$ & $^1\text{H}$ Patient Calf Test.....	123
A.1.1 Transmit coil tuning and placement .....	123
A.1.2 Receive coil placement.....	124
A.1.3 1st Stage Preamplifier.....	125
A.1.4 Second stage preamplifiers .....	126
A.1.5 Foot flexor stand placement .....	128
A.1.6 Calibration Verification Steps .....	128
A.1.7 Scan Parameters.....	134
A.1.8 Patient Preparation and Placement .....	136
A.1.9 Scan Protocol.....	138
A.1.10 Data Processing .....	141
A.2 Checklist for $^{31}\text{P}$ Protocol.....	143
APPENDIX B .....	149
B.1 Data Loading .....	149
B.2 Data Combination Tree .....	157
B.3 Data Exporting.....	159
B.4 Resetting of the Program .....	161
B.5 Accompanying Programs for Simulations.....	161

## LIST OF FIGURES

	Page
Figure 1. Digital down-conversion block diagram.....	12
Figure 2. ONI 1.0T extremity magnet.....	26
Figure 3. $\Delta B_0$ maps (ppm) of the 1.0T scanner.....	28
Figure 4. Circuit diagram of the transmit-only birdcage coil.....	30
Figure 5. Circuit diagrams of four-element array and comparison coils .....	32
Figure 6. Normalized spectra of the $^{31}\text{P}$ physiological concentration phantom.....	38
Figure 7. <i>In vivo</i> data from healthy volunteer. ....	42
Figure 8. Circuit diagrams of triple-tune coils and bias networks. ....	48
Figure 9. Bias distribution board.....	48
Figure 10. Top and Bottom views of the triple-tuned switchable array.....	50
Figure 11. $S_{11}$ reflection measurements .....	50
Figure 12. Time domain FIDs for clock stability .....	57
Figure 13. In phase time domain FID .....	57
Figure 14. Frequency domain plots of Pentek receive channels. ....	60
Figure 15. Circuit diagram and physical dimensions of the receive array design. ....	64
Figure 16. Circuit diagram of the preamplifier module .....	66
Figure 17. Picture of preamplifier box with components mounted.....	66
Figure 18. Labeled and assembled preamplifier module .....	67
Figure 19. Magnet flange plate for RF isolation and coil/preamplifier translation access (magnet-side shown). ....	68
Figure 20. Full configuration of the 32-element ring setup. ....	71
Figure 21. Flange plate connections.....	72

Figure 22. PIN diode drive box and flange plate. ....	73
Figure 23. Depth sensitivity map of an isolated test coil measured with a small pickup loop (OD = 8 mm). ....	81
Figure 24. Birdcage T/R images obtained with the receive array detuned. ....	82
Figure 25. Transverse images from all 32 array elements of a uniform canola oil phantom. ....	83
Figure 26. Transverse slice, sum of squares reconstruction of a canola oil phantom. ....	83
Figure 27. Sagittal images from all array elements of a uniform canola oil phantom. ....	84
Figure 28. Sagittal slice, sum of squares reconstruction of a canola oil phantom. ....	85
Figure 29. Combination method decision tree. ....	94
Figure 30. McMRSGUI front panel. ....	97
Figure 31. Mean distortion as a function of simulated noise. ....	98
Figure 32. The standard deviation of the distortion as function of the simulated noise level. ....	99
Figure 33. The mean SNR as a function of simulated noise. ....	99
Figure 34. Transmit coil cable attachment guide. ....	124
Figure 35. Proper receive coil insertion and balun cover attachment to the transmit coil. ....	125
Figure 36. Receive coil and preamplifier box attachment guide. ....	126
Figure 37. Second stage preamplifiers with respective low and high pass filters. ....	127
Figure 38. Proper coil attachment with limiters shown. ....	127
Figure 39. Front panel view of the Pulse Sequence_Case_structure.vi. ....	129
Figure 40. CSV file for a 300 us pulse duration. ....	130
Figure 41. Ultraview card control vi. ....	131
Figure 42. Ultraview 'ReadandGraph.vi' controls for zooming out (left) and selecting a region to which to zoom (right). ....	132

Figure 43. Pulse sequence settings for the steady state acquisitions with a long TR of 30000 ms and 90 degree tip angle. ....	134
Figure 44. Ultraview card control vi. ....	135
Figure 45. Proper taping and placement of cod liver on patient's leg. ....	137
Figure 46. Matlab script for post signal post-processing script. ....	142
Figure 47. Proper placement of cod liver oil pill. ....	145
Figure 48. Data input loading options for pre-processing and multi-channel combination options.....	150
Figure 49. "Starting" structure used to initially load in data into the pre-processing menu or data-combination. ....	151
Figure 50. jMRUI TextFile format for export option.....	151
Figure 51. Individual channel selection for pre-processing. ....	152
Figure 52. Batch Process option becomes available after data is loaded into the program and will guide the user through a short series of questions.....	153
Figure 53. X-axis adjustment options of MHz and parts-per-million. ....	155
Figure 54. The file subtraction function allows for a single file to be subtracted from a file to remove a macromolecule or baseline distortion.....	155
Figure 55. Processed structure information that is stored by the program.....	156
Figure 56. Multi-channel spectroscopy combination method decision tree logic utilized within the McMRSGUI. ....	157
Figure 57. Decision tree for determination of noise correlation between channels. ....	158
Figure 58. Question dialog for determination of 1H data availability. ....	159
Figure 59. The "Export Matlab Data" button exports the loaded data and any associated pre-processing or combination steps for traceability. ....	160
Figure 60. The "Export jMRUI Data" button exports individual acquisition data within a jMRUI Textfile format. ....	160
Figure 61. The clear button cleans out the information stored within the app structure. ....	161

Figure 62. Example complex covariance matrix of size Num_channels x Num_channels. ....	162
Figure 63. Example covariance matrix shown in the .txt format .....	162
Figure 64. Weighting factors for S/N <sup>2</sup> method saved in a Num_channel x Num_acquisitions matrix.....	163

## LIST OF TABLES

	Page
Table 1. Coil component values and part numbers .....	31
Table 2. Quality factor of different receive coils. ....	37
Table 3. Coil performance of physiological concentration $^{31}\text{P}$ phantom .....	39
Table 4. Comparison between combining Lorentzian peaks with and without alignment of the peaks. ....	40
Table 5. Q-factor results for the isolated triple-tuned elements and that of a single-tuned element as well as coupling measurements of the array coils per frequency. ....	51
Table 6. Experimental parameters for tests used to evaluate the receiver cards. ....	56
Table 7. Receiver card comparison of SNR and Linewidth across different dates.....	58
Table 8. Comparison of wideband and narrowband with varying decimation levels. ....	59
Table 9. Component values and part numbers for circuit elements of the 32-element array. ....	65
Table 10. Component and part numbers for preamplifier module circuit diagram.....	67
Table 11. Imaging parameters used to characterize performance of array. ....	70
Table 12. Gain measurements for the 32 mounted and assembled preamplifiers. ....	75
Table 13. Summary of average, standard deviation, and worst-case scenarios for $S_{11}$ , loaded Q-factors, coupling measurements, decoupling, and active detuning...	76
Table 14. Raw data for the $S_{11}$ and loaded Q-factors. ....	77
Table 15. Raw data for geometric decoupling of nearest and next nearest neighboring coils.....	78
Table 16. Raw data for preamplifier decoupling and active detuning .....	79
Table 17. Parameters for simulation of two Lorentzian peaks and coil element scaling factors. ....	95

Table 18. Scan parameters for the shimming calibration.....	129
Table 19. Scan parameters for performing the steady state acquisition with 12 averages and a TR of 30 sec. ....	134
Table 20. Calibration settings for phantom calibration test. ....	143
Table 21. LabVIEW and Ultraview settings for averaging test. ....	144
Table 22. LabVIEW and Ultraview settings for TR of 30 second experiment. ....	144
Table 23. LabVIEW and Ultraview settings for baseline portion of protocol. ....	146
Table 24. Timing protocol for patient protocol. ....	147



# CHAPTER I

## INTRODUCTION

### I.1 Background and Motivation

#### I.1.1 Nuclear Magnetic Resonance

The phenomenon behind nuclear magnetic resonance is dependent upon nuclei that possess an uneven number of protons and neutrons. This imbalance in the nucleus creates a quantum mechanical property known as a spin angular momentum (S) that influences the energy states at which the associated spins orient themselves when present in an external magnetic field [1]. The number of spin-states can be determined by Equation I.1 [2]. As all nuclei discussed in this work possess  $\frac{1}{2}$  spin nuclei, the remaining description of NMR resonance will assume a two-spin state system.

$$N_{states} = 2I + 1 \quad \text{Eq. I.1}$$

The spinning of the nucleus also creates a magnetic dipole moment about its axis that when placed in an external magnetic field, creates a precession of the nucleus around the external magnetic field. This precession is performed at a frequency (f), called the Larmor frequency, that is dependent upon the gyromagnetic ratio,  $\gamma$ , and the static magnetic field ( $B_0$ ), as shown in Equation I.2 [3]. The gyromagnetic ratio is unique for different nuclear isotopes due to the particular proton mass and charge, ultimately providing different frequencies at which nuclei resonate.

$$f = \gamma B_0 \quad \text{Eq. I.2}$$

The aforementioned two-spin energy states align either parallel or antiparallel when an external, static magnetic field is present. As described with Zeeman splitting and Boltzmann's distribution, a slight excess of net spins will exist in the lower energy state aligned with the magnetic field [4]. This slight excess provides the foundation of the thermal equilibrium magnetization,  $M_0$ , from which the NMR signal will be derived. The thermal equilibrium magnetization, as shown in Equation I.3 [5], depends on the total number of nuclei ( $N$ ), the gyromagnetic ratio, Planck's constant ( $h$ ), the static magnetic field strength, the absolute temperature ( $T$ ), and the Boltzmann constant ( $k$ ).

$$M_0 = N \left( \frac{\gamma^2 \hbar^2 B_0}{4\pi^2 kT} \right) \quad \text{Eq. I.3}$$

To detect the net magnetization,  $M_0$ , that is aligned with the much stronger  $B_0$  field, an RF perturbation at the Larmor frequency of the nuclei of interest ( $B_1^+$ ) must be applied in an orientation that rotates the spins into the transverse plane from the  $B_0$  direction. Assuming conventional MR notation of  $B_0$  orientation in the z-direction, the resulting signal in the transverse plane ( $M_{xy}$ ) will be influenced by the extent of the angle which the spins are tipped ( $\alpha$ ) by the  $B_1^+$  pulse according to Equation I.4.

$$M_{xy} = M_0 \sin(\alpha) \quad \text{Eq. I.4}$$

Spins that are tipped into the transverse plane become distinguishable from the static magnetic field, as they continue to precess at the Larmor frequency. The transverse orientation of the  $M_{xy}$  vector is short lived due to the  $T_1$  and  $T_2$  relaxation methods that are inherent to the substance and its environment. The  $T_1$  relaxation relates to the longitudinal relaxation of the main magnetization vector due to a return of the spins to thermal equilibrium [6]. Energy exchange between the neighboring spins through

collisions and dissipation of heat results in the gradual return of the spins to the equilibrium along the z-axis exhibited before the  $B_1$  field was applied. The  $T_1$  relaxation constant is defined as the time for the  $M_0$  regrowth to reach approximately 63% of the overall magnetization, which recovers in an exponential fashion. The second relaxation method or the  $T_2$  relaxation method is related to spin-spin interactions from the molecular positioning of nuclei with different neighboring combinations of the two different energy states and their local magnetic environment [6]. As they are spinning at slightly different rates due to their neighboring nuclei, the transverse magnetization vector begins to dephase following the initial transverse tip. This will quickly result in overall phase incoherence. The  $T_2$  relaxation constant is defined as the time for the transverse magnetization to fall to approximately 37% of its starting value. Together, the  $T_1$  and  $T_2$  relaxation rates provide characteristic mechanisms for the identification of the local environment of the spins.

The net magnetization vector, as defined in Equation I.3, represents the maximum signal contribution that is available for an NMR experiment. In analyzing its major contributing components, the gyromagnetic ratio, number of nuclei, and magnetic field strength are the main signal-influencing factors, provided that the sample is at room temperature. Therefore, increasing the scanner field strength, which is not feasible for most MR scanners, or viewing a different nucleus with a larger gyromagnetic ratio are the only options for increasing the net available signal. This has repercussions for X-nuclei, or non- $^1\text{H}$  nuclei, which have lower gyromagnetic ratios when compared to  $^1\text{H}$  [7]. Additionally, the concentration of NMR-active isotopes of X-nuclei present in the body

are often several orders of magnitude smaller when compared to the abundance of hydrogen. Therefore, the remaining major variable, the number of nuclei, also presents a challenge for X-nuclei detection.

### **I.1.2 Radiofrequency Coils**

Radiofrequency (RF) coils are an integral part of the MR experiment as they are the mechanism from which RF energy is transmitted to ( $B_1^+$ ) and received ( $B_1^-$ ) from the body. As discussed in section I.1.1, the nuclear precession of spins is distinguishable from the main magnetic field following the  $B_1^+$  pulse that pushes the spins into the transverse plane. The subsequent time-varying signal can be detected by an RF coil through Faraday induction, provided the coil is tuned to the frequency of precession and oriented in such a way to detect the transverse signal. The time-varying magnetic flux induces an electromotive force (EMF) in the coil that is detectable as a voltage at the terminals of the coil [8]. Thus, RF coils are the mechanism by which the nuclear spins are both excited from equilibrium and monitored as they return to equilibrium.

While an RF coil can be used as both a transmitter and receiver or transceiver, benefits can be had by dedicating specific but separate transmit and receive coils [9]. Large volume coils are typically used as transmitters due to their ability to create a more homogeneous  $B_1^+$  field, uniformly exciting the region of interest. Due to their large size, they cannot always be located near the sample of interest, effectively reducing their sensitivity due to receiving noise from their entire volume. A dedicated receive coil benefits from a smaller footprint that can be more closely positioned to the sample and only “sees” noise from its smaller sensitivity region with the noise ideally being generated

from only the sample [10]. As receive coils are commonly loops, their sensitivity falls off radially away from the center of the coil, which is beneficial for signal localization but not for generating a uniform  $B_1^+$  signal. Therefore, with proper detuning networks to utilize the combination of a transmit and receive coil, the benefits of a uniform transmit field from a volume coil and the higher sensitivity and localization from a receive coil can lead to an improved received signal from the body.

To further enhance signal reception, an array of dedicated receive elements specifically conformed to the anatomy of interest can be constructed so as to obtain the field-of-view (FOV) coverage of a single large coil with the increased sensitivity of small coils [11]. The level of signal enhancement is determined by several factors, specifically coupling between coils, filling factor of the array, and resistive losses from additional decoupling coil components. Interelement coupling between receive array coils' introduces correlated noise between elements, thereby introducing noise that is not random and will not average to the benefit of the signal-to-noise ratio (SNR) [12]. The extent to which the array conforms to the geometry of interest directly correlates to the obtainable signal from the region. In fact, coils that don't directly contribute to the region should not be considered when combining the channels in post-processing. With the addition of more receive array elements, additional components for active and/or passive detuning (in the case of an originally geometrically detuned transmit/receive pair) and preamplifier decoupling (for an array design that can no longer benefit solely from geometric detuning) are required. Active detuning elements require a parallel inductor and capacitor (LC) trap tuned to resonate at the Larmor frequency of interest [13], introducing an additional lossy

inductor to the circuit. Preamplifier decoupling networks typically require a minimum of at least a single inductor in addition to several capacitors to achieve the requisite impedance transformation required to minimize inductive coupling between array elements [14]. Thus, the design and construction of arrays must be carefully performed to minimize losses in order to realize the full benefit of the array.

Due to the varying receptivity's and *in vivo* concentrations of NMR-active nuclei, the increased receive sensitivity afforded by RF array coils is often required to interrogate X-nuclei, or non- $^1\text{H}$  nuclei [15]. Coupled with the needs of  $B_0$  shimming, relating X-nuclei information to a specific anatomical reference, or correlation to complimentary spectroscopy, double tuning or even triple-tuning of coils or coil systems is often required. Enabling additional and complimentary information without the need for patient, phantom, or coil setup movement is beneficial for minimizing experimental errors and reducing overall time in the scanner. The addition of multi-tuning circuitry comes at the cost of adding additional components, resulting in a lower efficiency for the coil system. Due to the nature of the optimization problem, one or more frequencies will suffer from quality factor losses depending on how the network is designed [16]. Varied methods have been utilized for accomplishing this feat [17-20], but the design choice is dependent upon the overall experimental setup and required sensitivity and localization for each nucleus. Through the careful design and selection of an array, the sensitivity decrease from multi-tuning of the coils can be offset to enable detection of multi-frequency data for a better understanding of underlying physiologies or sample content.

### **I.1.3 Magnetic Resonance Spectroscopy & Imaging**

The time-varying NMR signal detected by an RF coil as the nuclear spins return to equilibrium is known as a free induction decay (FID), due to the exponential decay of the signal from  $T_2$  dephasing and magnetic field inhomogeneities perturbances [6]. Variations in the frequency content from the main Larmor frequency is the main source of information for both magnetic resonance imaging (MRI) and magnetic resonance spectroscopy (MRS), although each method approaches these variations in different ways. The Fourier Transform is utilized for both methods to present the MR frequency content in an understandable manner: either in a 1D frequency spectrum (MRS) [21] or a 2D-Fourier transformed image (MRI) [22].

MRS is unique in that it relies on the chemical environment of the nucleus to provide differences in the frequency content. Shielding of the nucleus from the electron cloud introduces a slight shift in the overall precession of the nucleus away from the Larmor frequency [23]. The extent of the shift is based on the presence of electronegative compounds, pi bonding, and hydrogen bonding in the chemical environment [23, 24]. Therefore, most MRS studies are performed with a known reference signal to which all other compounds are referenced within the Fourier-transformed spectrum via their chemical shift value,  $\delta$ , as provided on a parts per million (ppm) frequency scale [23, 25].

Following identification of the compound based on its shift, the MRS signal can be quantified via finding the area underneath the curve. Several methods, such as linear combination model fitting [26-28] and peak fitting [29, 30], are commonly used for identifying and quantifying compounds. This quantification is relative unless a known

reference concentration providing a different peak than what is found in the sample is available to compare calculated areas under the curve. Therefore, studies either utilize a reference compound within the sensitive region of the coils or compare relative ratios of compounds within the spectrum [30]. Prior knowledge of metabolic processes can be utilized to further glean information from *in vivo* spectra when viewed over time, such as the calculation of the intracellular pH using the Henderson-Hasselback equation relating the position of phosphocreatine and inorganic phosphate in  $^{31}\text{P}$  studies [31, 32].

As the MRS experiment can determine differences in compounds based on their chemical shift, the main concerns in MRS studies are the source of the signal or localization and achieving enough signal to distinguish it from the noise. Localization can come from two means: gradient localization accompanied by specialized pulse sequences or localization based on the sensitivity and positioning of RF coils. Techniques, such as STEAM [33], PRESS [34], semi-LASER [35], EPSI [36], and ISIS [37], all utilize gradients to localize the MR signal to a single voxel or series of voxels. Along with accompanying  $^1\text{H}$  localization images, the spectral voxel can be correlated to a specific region of the anatomy for analysis. These techniques are routinely used at magnetic field strengths of 1.5T and above due to the increased net magnetization attainable at higher field strengths to compensate for minimizing the number of available nuclei through localization [32]. In cases where voxel-level localization is not required, RF surface coils and their inherent sensitivity patterns can be utilized for a degree of localization in MRS experiments. Careful placement and design of the coils must be maintained to ensure that



the signal is indeed coming from the region of interest. Pulse and acquire techniques are commonly used in these setups to maximize the attainable signal.

MRI varies from MRS in that the frequency content is intentionally varied and phased with known magnetic field gradient patterns to correlate frequency to position. To demonstrate this mechanism, the frequency of the spins within a homogeneous magnet must be considered. As they are experiencing the same uniform magnetic field strength, all the spins will be at the Larmor frequency ( $f_L$ ). The addition of a linear z-directed gradient during a finite-bandwidth  $B_1^+$  pulse ( $f_L \pm BW/2$ ) serves as a way of exciting a slice within the sample due to the augmenting of the magnetic field [38]. The Larmor frequency of the spins within the slice are linearly, but slightly varied based on the change in the magnetic field. Following the excitation of the slice, gradients and/or additional pulses are used to reverse the transverse dephasing that began after the  $B_1^+$  was applied [39, 40]. The transverse phase coherence will return in the form of an echo but with a lessened amplitude due to the irreversible, random interactions between some of the nuclei [39]. During signal digitization and as the nuclear spins are coming back into phase, a single linear gradient in the x- or y-oriented direction is applied for frequency encoding of the signal [41]. This causes the frequencies at different sides of the sample to be acquired at different frequencies that can be directly correlated to spatial dimensions based on the strength of the gradient. The repetition of the process with different pulsed variations in the remaining cardinal direction's gradient creates phase differences in the digitized signals through a process known as phase encoding [42]. The extent of the levels of the x- and y-oriented gradients are determined by imaging parameters, such as the field-of-view,

image matrix size, and sample bandwidth. The time-domain digitized signals acquired with different phase encode steps are arranged into a matrix forming what is formally known as k-space [43]. The k-space matrix is transformed into the image domain using a two-dimensional inverse Fourier transform [22].

By nature of the nuclear magnetic resonance progression after the initial  $B_1^+$  pulse, the nuclear spins proceed to become phase incoherent very quickly. Any other interactions that are applied within the system aside from the excitation pulse or rephasing pulse increase the dephasing of the spins and noise in the system. Use of the fast-switching gradients that provide frequency and phase encoding are not immune to sourcing additional influences on the spins. A detrimental side effect of gradients used for pulsed magnetic gradient fields that aren't properly shielded or pulse-compensated is the development of magnetically induced eddy currents in the conducting structures of the magnet, resulting in resolution degradation, misregistration, loss of SNR, and phase changes [44]. Despite this ever-possible side effect, the use of fast switching gradients has widely been accepted by the MR field and is integrated within most modern pulse sequences for their ability to quickly manipulate nuclear spins without the deposition of RF energy.

As briefly demonstrated in the previous description of fast-switching gradient use and loss of phase coherency, the MR experiment is a balance of experimental parameters that have tradeoffs. As briefly mentioned in Section II.1.2, RF coils can provide a means of localizing the signal to a position. With arrays, coils that are located closer to the source of signal will have a stronger signal than an element of the array that is further away.

Knowledge of the coil locations can therefore lead to expedited acquisition with the increased localization information elicited from coils, effectively reducing the required information needed to fill k-space. Pulse sequence techniques that utilize this method for include SMASH [45], GRAPPA [46], and SENSE [47]. Speeding up the acquisition with coil localization provides an overall faster imaging time but at the expense of the signal-to-noise ratio (SNR). Resolution and localization are inversely related to SNR. EPI [48] and other gradient-based refocusing techniques drastically reduce image acquisition time but require strong, fast-switching gradients to traverse K-space. The added audible noise from the vibrations created by the pulsed Lorentz force reduces patient comfort within the bore [49]. Thus, the proper selection of RF array coils, pulse sequence, and imaging parameters must be carefully chosen to maximize the SNR, minimize the overall scan time, and obtain adequate resolution to evaluate the condition at hand.

#### **1.1.4 Data Sampling**

The frequencies at which MR signals are located are often on the order of 10s to 100s of megahertz, depending on the magnetic field strength and Larmor frequency. To directly sample these frequencies at or above the Nyquist rate [50], the data sizes can often be quite large and difficult to manage or store. Methods for addressing this include undersampling and mixing the signal to baseband before digitization. Undersampling requires knowledge of the bandwidth of the signal that is to be expected, as hardware filters are used to filter out out-of-bandwidth signal to prevent undesired aliasing signals from shifting down to the intended aliased frequency. Hardware systems, such as super heterodyne receivers, have been developed to “mix” the high frequencies down to a lower

frequency that can be more easily sampled with a smaller rate [51]. In newer systems, some of the functions for mixing and filtering are performed in the digital domain due to high-speed analog-to-digital converters (ADCs). Digital down-converters (DDCs) utilize mixers and sine and cosine signals produced from a direct digital synthesizer (DDS) to shift the now quadrature signal to baseband before filtering [52]. A lowpass filter is then applied to both signals to remove out of band noise and reject the sum frequency image, as shown in Figure 1. During this step, the filter can be used to decimate or remove certain data points, based on the level of decimation, to reduce the overall data file size. This method produces two channels of signal typically labeled as I (cosine path) and Q (sine path) data.

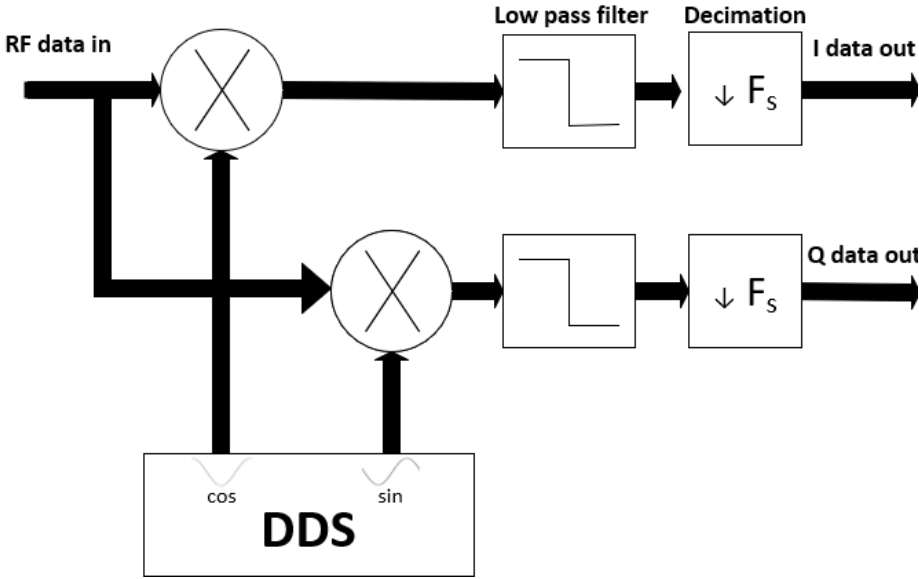


**Figure 1. Digital down-conversion block diagram.**

The block diagram demonstrates the mixing of the radiofrequency (RF) signal with the DDS sinusoids, filtering of the digitized signal, and subsequent decimation.

For multi-channel systems that have limited digitization ports, frequency-division multiplexing is a potential method for expanding the overall channel count capabilities [53]. This method requires additional hardware preamplifiers, mixers, and intermediate filters for each coil channel before being combined, digitized, and down converted to reduce the overall data size. The maximum channel count is dependent upon the total digitization ports and the associated number of DDC subchannels of the receiver card. For example, if a coil array with 32 elements was to be used, the receiver card could theoretically only need four digitization ports with each port possessing an 8-subchannel DDC. The associated front-end components could become bulky for higher channel counts but would enable multi-channel data acquisition with a single digitization card.

### **I.1.5 Processing of Array Data**

To achieve the full potential of phased arrays, individual channel data needs to be optimally phased and combined in post-processing to provide an improved result [11, 54]. In theory, each separately digitized channel will require a complex weighting coefficient that can be applied in post-processing before combination with the other channels. The selection of these complex weighting coefficients is dependent upon the goal for the reconstruction. Generally, the SNR is the parameter being optimized for the reconstruction, as this should reflect the signal being detected. It is important to consider if the combination method is adding bias to the data, which results in signal distortion. Roemer, in his seminal work on phased arrays, put forth a method to achieve the optimal weights [11], but in practice, the experimental measurements needed to reproduce the theoretical optimum are difficult to obtain. For imaging applications, the sum-of-squares

method [11, 54, 55], singular value decomposition (SVD) [56], and sensitivity maps [11, 47] have all been utilized to determine the weighting coefficients. Different weighting factors are required at different voxels due to the spatial dependence upon the optimal weights. Spectroscopy applications have different weighting schemes, such as SNR weighting [54, 57], whitened singular value decomposition (WSVD) [58], and adaptively optimized combination (AOC) [59], with some methods requiring additional noise scans or water reference scans to best combine array data. The selection of combination method for either spectroscopy or imaging ultimately comes down to the available SNR per channel, availability of additional information from noise scans or reference maps, the desired parameter that is being interrogated (certain region of the spectrum or image), and whichever method introduces minimal bias to the reconstruction. As the theoretical optimum as posited by Roemer may not always be achievable, it is beneficial for researchers to have multiple methods available as some methods will perform better under particular experimental parameters.

### **I.1.6 MR Accessibility and Motivation**

The progression in the development of an imaging modality has two paths that must run their course. The first involves rapid expansion and successive sophistication. This can be seen in the MR field after the development of the first nuclear magnetic resonance experiments by Bloch and Purcell in the 1940s [6, 60, 61]. MR spectroscopy studies were utilized to analyze a host of compounds and chemicals [62-65]. The advent of superconducting magnets increased the pace at which these studies were performed. Lauterbur provided a boost to the NMR field with the discovery that images could be

obtained with the method [66, 67]. MRI brought the expansion and utility of the method to the clinical setting with a further refinement to more homogeneous and stronger magnets with increasing bore size. Increased  $^1\text{H}$  coil counts with up to as many as 128 coils have been documented only a few decades following the demonstration of array coils by Roemer [68-72]. Work today in evaluating the intricacies of the methods are still being carried out to expand MR capabilities that already include multiple contrast mechanisms for soft tissue [6, 73, 74], diffusion and fluid flow assessment [74, 75], functional measurements of brain activity [76], and chemical and metabolic activity monitoring to name just a few [77, 78].

While active work into the newer and successive refinement of the field are still required, the second path of improving accessibility to the methods that already exist is important for overall use of the modality. This has been an area where the MR field has been limited. Moving the method away from the clinical setting where stronger and bigger magnets are present has proved challenging. MR spectroscopy has been greatly utilized by chemists but in magnets with field strengths upwards of 20T [79-82], while clinical full-body MRI scanners range in field strengths from 1.5T to 7T [83, 84]. Two studies in 2010 and 2011 found that the average cost for 1.5T scanners to be bought and sited in the U.K. averaged around \$1.5M U.S. dollars [85-87]. That brings the cost of a full-body clinical scanner to roughly one million U.S. dollars per Tesla, making the method cost prohibitive for non-clinical entities. Moving to cheaper magnets would provide better accessibility from a cost perspective. Therefore, the feasibility of performing X-nuclei

spectroscopy with a more cost-effective extremity scanner in a non-clinical setting was tested in this work.

The clinical setting for MRS and MRI have primarily relied on  $^1\text{H}$  due to its increased signal content and sensitivity. Hardware capabilities for multi-channel, X-nuclei are just now becoming available at some clinical sites, enabling complimentary information to  $^1\text{H}$  to be accessible with the increased sensitivity of array coils. The lack of X-nuclei hardware for enabling disease identification and classification has been a limiting factor for MRS, which isn't covered by Medicare and Medicaid [88]. Thus, demonstrating X-nuclei utility with the benefit of arrays and associated hardware is an important step for promoting acceptance of the method. For this reason, the aforementioned X-nuclei spectroscopy study utilized an add-on coil system and broadband transceiver system to evaluate *in vivo*  $^{31}\text{P}$  metabolism. Expanded capabilities with a different receiver card for future X-nuclei studies was also assessed.

Additionally, the reduction of scan times for full-body imaging is needed to increase throughput of MR systems to decrease the cost and benefit a larger population. MRI is the premier soft tissue imaging modality aside from ultrasound but is often hindered from long scan times due to the low sensitivity nature of the method. Techniques for fast MRI, such as SMASH [45], SENSE [47], PILS [89], GRAPPA [46], and EPI [48], have made major improvements in scan time through utilizing undersampling techniques and array coil geometries to reduce the volume of data required for image reconstruction. Further reduction of scan times from the order of 10s of minutes would drastically improve availability of the magnets, add the benefit of improved patient satisfaction with less time



spent in the bore, and enable longitudinal full-body scanning studies for health evaluation. Hardware for theory evaluation regarding single-shot echo, full-body imaging was developed in an effort to realize the potential of this game-changing improvement for MRI.

As the field is moving towards the increased reliance upon multi-channel arrays for signal acquisition, reduction of reliance on commercially-driven software for analyzing this form of data will be important for researchers. Reproducibility and traceability of data processing to ensure good scientific rigor is important for all spectroscopy data. Open-source communities have been distributing work for this type of off-site analysis but have mainly focused on quantifying the spectroscopy data that has already been combined by their specific MR vendor. Therefore, an open-source software was developed for multi-channel, MRS combination that provides multiple literature-based combination techniques along with a decision tree matrix for helping identify which technique is most appropriate regarding the available information and noise characteristics of the data to prevent spectral distortion. An accompanying simulation to the combination software can be utilized to determine approximate SNR values at which increasing levels of spectral distortion begins. Together, these methods can aid researchers in producing more reliable spectra for quantification.

## **1.2 Specific Aims and Dissertation Organization**

This work describes several projects pertaining to hardware and software approaches to further increase accessibility of nuclear magnetic resonance imaging and spectroscopy. While the approaches described thus far focus on specific aspects of coil

design, clinical evaluation, and an open-source software for spectroscopy data processing, they provide a foundation for further expansion of MRI and MRS to expand the capabilities of these methods. The overall goal of this work is to present engineering solutions and techniques that increase the accessibility of MRI and MRS through RF coil design and software approaches.

Guided by this goal, this dissertation is organized to present the requisite background information to understand the relevant topics within the following chapters relating to this research's specific aims:

- Aim 1: Design, construct, and evaluate multi-channel, multi-nuclear coils and capabilities for NMR spectroscopy
- Aim 2: Design and construction of a 32-channel  $^1\text{H}$  coil ring for the application of fast MRI data acquisition with a 32x32 array
- Aim 3: Development of an open-source, magnetic resonance spectroscopy software for multi-channel spectroscopy data combination method evaluation

Chapter I introduces some requisite background information regarding the underlying principles behind nuclear magnetic resonance and how this phenomenon enables the methods of magnetic resonance spectroscopy and imaging. The utility and distinction between the two methods was discussed in terms of the type of information that can be gleaned from one over the other, in addition to how each method's signal is obtained. The concept of signal localization using electronic gradients or through spatial proximity from radiofrequency coils was discussed. The role of the radiofrequency coil as

the transmitter and receiver in the MR experiment was detailed. The extension of using multiple radiofrequency coils in the form of an array and the benefits of the increased sensitivity over a larger field of view were discussed with regards to improving x-nuclei detection. Next, a brief overview was provided of data sampling and how modern sampling architectures can reduce data sizes while acquiring more channel counts worth of data. Following data acquisition, radiofrequency array data requires combination methods to obtain a single either images or spectra with increased sensitivity. An overview of some of the required information and techniques was presented. The overall motivation for this for work involving MR accessibility was then described. The progression and direction of the field were discussed with some key areas of this work highlighted in terms of improving accessibility. The final portions of this chapter describe the dissertation style and brief overviews of the upcoming chapters.

Chapter II.1 describes a work detailing the evaluation of the feasibility of obtaining dynamic  $^{31}\text{P}$  spectroscopy from a 1.0T extremity magnet that had been retrofitted with broadband transceiver capabilities, a  $^{31}\text{P}$  coil system, and a foot flexion system for enabling exercise protocols. It details the methodology for design choices associated with the construction and evaluation of the transmit and receive coils, along with a comparison of the receive array with a large, single element of same overall size. To demonstrate the utility of x-nuclei capabilities with an extremity scanner, a healthy volunteer underwent the exercise protocol. This test demonstrated that literature-supported metabolic tracking factors, such as the phosphocreatine recovery constant and underlying pH, could be quantified with this system. Overall, this demonstration of obtaining x-nuclei

spectroscopy with a scanner outside of the clinical setting is an important step in providing wider availability to this useful diagnostic tool.

Chapter II.2 details the design and benchtop testing of a three-element, triple-tuned array that was implemented with a switchable matching and tuning system. As RF coils are typically only single-tuned, multi-nuclear data acquisition requires the replacement of separate coils for each nucleus, potentially inducing error from coil or patient movement. This system was designed using active PIN diodes to obtain switching capabilities between three different frequencies, all from the adjustment of a single external switch. Although this test was limited to benchtop testing and to an array configuration that could be geometrically detuned, it demonstrated that an array could be multi-tuned with this method, providing an option for coil designers looking for a method to multi-tune an array.

Chapter II.3 focuses on the evaluation of a broadband receiver module for increasing the capabilities of a broadband transceiver system. An SNR benchmark comparison was performed using the current receiver card and the new receiver module. Functionality of the new receiver module, such as the ability to decimate data and its influence on reconstituting the original data and multichannel, multi-frequency capabilities, were explored to demonstrate advantages and experimental possibilities that were opened due to use of the card.

Chapter III describes the design, construction, and evaluation of a 32-element, ring array for the testing of a fast MRI theory requiring a 32x32 element array. The simplified array was designed, along with the associated preamplifier decoupling module, to be translatable within the bore for a 32-step translation experiment, effectively acquiring

signal from all the positions of a 32-ring array. The coil and preamplifier module construction are thoroughly described along with the benchtop coil characterization. The benchtop data includes scattering parameters of the array, quality factors, preamplifier decoupling, and active detuning. Imaging data demonstrating the functioning of the array is included. A protocol detailing the experimental setup for a 32-step translation experiment, which was outside of the scope of this dissertation, was included for future testing of the system. This experimental setup enables the testing of a fast MRI theory that has implications for drastically reducing the time for whole body imaging.

Chapter IV details an open-source software that was developed to enable the processing and combination of array data before the quantification of the data. As experiments with array coils are becoming more common, the ability to test different combination techniques to best represent the data is necessary for researchers. This program provides a graphical user interface with built-in options for preprocessing and phasing of the data before the combination of channel data with literature-recognized combination methods. Export data types are built-in for further processing with previously published quantification software's. An accompanying simulation for spectral distortion aids in identifying SNR levels of combined spectra at which spectral distortion begins to increase.

The final dissertation chapter represents the dissertation conclusion. The implications and significance of the discussed projects with regards to the field of MRI/MRS are reiterated. Future applications and potential next steps are addressed for the specific projects.

### **1.3 Dissertation Style**

The formatting style used for reference citations and table/figure titles follows that of *Magnetic Resonance in Medicine*. The chapter organization of this dissertation follows the Traditional Style Format as delineated by the Texas A&M University Office of Graduate and Professional Studies and the Department of Educational Psychology. Chapters II.1 and IV present manuscripts formatted and intended for publication. Chapter II.2 – III follow a structured format which consists of the following sections: introduction, methods, results and discussion, and conclusion. References for all chapters of the dissertation are included at the end of the dissertation.

## CHAPTER II

### RADIOFREQUENCY COILS FOR MULTI-NUCLEAR SPECTROSCOPY

#### **II.1 Assessing the Feasibility of Dynamic $^{31}\text{P}$ MR Spectroscopy for Metabolic Studies with a 1.0T Extremity Scanner**

##### **II.1.1 Synopsis**

The feasibility of conducting *in vivo* non-localized  $^{31}\text{P}$  Magnetic Resonance Spectroscopy (MRS) with a 1.0T extremity scanner and the potential to increase accessibility of this important diagnostic tool for low cost applications is revisited. This work presents a custom transmit-only quadrature birdcage, four-element receive coil array, and spectrometer interfaced to a commercial ONI 1.0T magnet for enabling multi-channel, non- $^1\text{H}$  frequency capabilities. A custom, magnetic resonance compatible plantar flexion-extension exercise device was also developed to enable exercise protocols. The coils were assessed with bench measurements and  $^{31}\text{P}$  phantom studies before an *in vivo* demonstration. In pulse and acquire spectroscopy of a phantom, the array was found to improve the signal-to-noise ratio (SNR) by a factor of 1.31 and reduce the linewidth by 13.9% when compared to a large loop coil of the same overall size. *In vivo* testing results show that two averages and a four second repetition time for a temporal resolution of eight seconds was sufficient to obtain phosphocreatine recovery values and baseline pH levels aligned with expected literature values. Initial *in vivo* human skeletal muscle  $^{31}\text{P}$  MRS allowed successful monitoring of metabolic changes during an 18-minute exercise protocol. Adding an array coil and multinuclear capability to a commercial low-cost 1.0T

extremity scanner enabled the observation of characteristic  $^{31}\text{P}$  metabolic information, such as the phosphocreatine recovery rate and underlying baseline pH.

### **II.1.2 Introduction**

$^{31}\text{P}$  MRS offers a unique noninvasive method to investigate *in vivo* metabolism and further improve our understanding of many disease processes. Through the quantification of phosphocreatine (PCr), inorganic phosphate (Pi), and adenosine triphosphate (ATP) compounds, metabolism can be observed from  $^{31}\text{P}$  spectra. Understanding *in vivo* human  $^{31}\text{P}$  spectra includes interests in skeletal muscle energetics, neuromuscular disorder, cerebral phosphorylated metabolites, coronary heart disease and metabolic characteristics in tumors [77, 90-94]. In many of these studies, observing  $^{31}\text{P}$  spectra over time is required to monitor energetics. The relatively low concentrations of phosphorus in the body paired with the need for a highly homogeneous magnet make  $^{31}\text{P}$  spectroscopy challenging. Hence, despite some efforts and success at performing  $^{31}\text{P}$  spectroscopy at 1.5T [91, 94-96], most current  $^{31}\text{P}$  spectroscopy is performed on high field 3.0T and ultra-high field 7.0T systems [97-101].

In addition to the cost of high field scanners, higher-order active shimming significantly improves the B0 homogeneity and achievable minimum linewidth but at the expense of the necessary hardware and associated software needed to accompany the magnet. Obtaining clinically relevant  $^{31}\text{P}$  spectra without the need for high field scanners and/or complex and expensive shimming capabilities would increase the accessibility and thus the potential utility of the method.



Extremity nuclear magnetic resonance (NMR) scanners, which usually have low (<0.5T) or medium (0.5-1T) field strength, are low-cost research and/or clinical diagnostic instruments. They are gaining increasing popularity among hospitals and are very useful to image upper and lower extremities [102]. They are seldom used for MR spectroscopy, however, not only because of their low field strength but also because manufacturers do not provide sequences, coil hardware, and/or the spectrometer does not support non- $^1\text{H}$  spectroscopy. This work presents a transmit-only volume coil and a multi-element receive-only array combined with a custom, prototype NMR spectrometer that adds non- $^1\text{H}$  frequency and multi-channel receive support for an extremity magnet to overcome these limitations in sensitivity and supporting front-end hardware. As the extremity magnet was designed for imaging and was not shimmed to the level typically required for spectroscopy, it was felt that there may be additional benefit obtained in the linewidth since each coil sees a smaller region, presumably with a narrower linewidth. Our objective was to investigate whether clinically relevant  $^{31}\text{P}$  spectra could be obtained in the human calf at 1.0T using a low-cost extremity magnet, enabling the possibility of  $^{31}\text{P}$  spectroscopy outside of the clinical setting. A preliminary version of this work has been presented [103].

## **II.1.3 Methods**

### **II.1.3.1 Design Considerations**

All experiments were performed using a 21 cm bore, ONI Medical Systems 1.0T extremity magnet, shown in Figure 2, installed in the Texas A&M University Magnetic Resonance System Lab. The magnet system was designed to provide detailed  $^1\text{H}$  images

of the foot, ankle, knee, arm, etc. The ONI system included passive shimming installed during installation, linear X, Y, and Z gradient coils, and no high order electronic shims. The ONI system provided  $^1\text{H}$  imaging protocols and a single  $^1\text{H}$  Tx/Rx channel.



**Figure 2. ONI 1.0T extremity magnet.**

A custom plantar flexion-extension exercise device for MR exercise experiments and protocols is shown. A pulley and bucket (not shown) attach to the foot pedal (circled in blue) for custom weight to be used on a per-subject basis.

To aid in the design and placement of the array, the static magnetic field of the 1.0T magnet was mapped to explore any potential adjustments or compensations that could be made in the experimental setup. Although this approach assumes that the static field remains the same between evaluation with the hydrogen coils and separate placement of the  $^{31}\text{P}$  coils which could not be concurrently placed in the bore due to size constraints, large inhomogeneities can be avoided and the patient and coil system can be better

positioned within the magnet. The mapping can also provide an estimate of the potential variance in linewidth between array elements, ideally minimized for more straightforward quantification of the combined spectra.

To characterize the static magnetic field, the 16-rung ONI commercial  $^1\text{H}$  volume birdcage (diameter = 17.8 cm, length = 16.5 cm) was used to acquire two sets of axial and coronal multi-slice gradient echo images with echo times of 10 and 30 ms and a repetition time of 2100 ms, from a cylindrical copper sulfate solution phantom (diameter = 9 cm, length = 17 cm, ONI PN: 2000-0006). Each scan acquired 60 slices with a slice thickness of 2 mm with no gaps. The field-of-view (FOV) and matrix size were 160 mm x 160 mm and 128 x 128, respectively. The three linear gradient shims were used to minimize the image volume's  $\Delta B_0$  before the multi-slice images were obtained. Following phase unwrapping and subtraction of the phase images, the  $\Delta B_0$  field maps were calculated using Equation II.1,

$$\Delta B_0 = \frac{\Delta\varphi}{\gamma\Delta TE} \quad (\text{Eq II.1})$$

where  $\Delta\varphi$  is the phase difference between images with different echo times,  $\gamma$  is the gyromagnetic ratio, and  $\Delta TE$  is the difference in echo times of the images [104]. Examples of the  $\Delta B_0$  field maps are shown in Figure 3 with the magnetic field standard deviation denoted over the region anticipated for coil size and placement. This was considered sufficient for  $^{31}\text{P}$  spectroscopy given the minimum spacing between peaks of interest is several parts per million (ppm) [105].

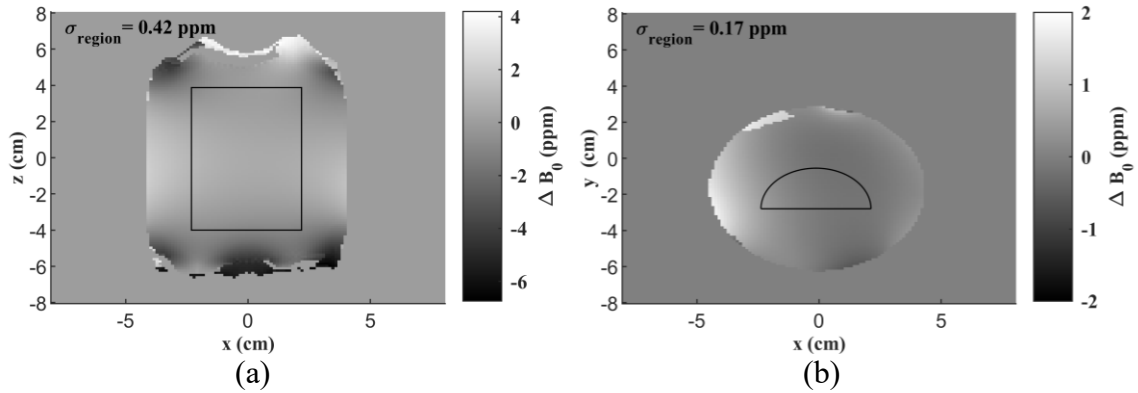


**Figure 3.  $\Delta B_0$  maps (ppm) of the 1.0T scanner**

The central coronal slice (a) and central axial slice (b) of the phantom. The standard deviation was taken over a 4.5 cm x 7.88 cm rectangular region in the coronal map and a semi-circle with a radius of 2.25 cm in the axial slice, reflecting approximate coil sensitivity patterns for both size and placement of the coils.

### II.1.3.2 Spectrometer and RF Coils

A broadband NMR spectrometer previously built in-house was used to enable transmission and reception at the  $^{31}\text{P}$  frequency [106]. For non-localized spectroscopy experiments, the pulse sequence was generated and controlled through a LabVIEW environment. For transmission, a hard pulse excitation was used and fed to a conventional 500 W broadband amplifier (CAP1075-500, Communication Amplifiers LLC, Terrell, TX). In receive mode, the coils were connected to a two-stage amplification system with the first stage including a MITEQ low noise amplifier (AU-1583) and the second stage a Mini-Circuits amplifier (GALI-74+). A Mini-Circuits low pass filter (BLP-21.4+) and high pass filter (ZFHP-1R2-S+) were used for anti-aliasing filters directly before digitizing the signal using a 16-bit, 4-channel high-speed digitizer card (AD16-250x4-8GB-155T, Ultraview Corp, Berkeley CA).

The transmit coil was a 16-rung low pass quadrature birdcage with a diameter of 17.8 cm and a rung length of 16.5 cm. The rungs and end-rings were milled on copper-clad flexible FR4 boards and mounted on acrylic tubing. A schematic of the coil is shown in Figure 4 and all part values and numbers are shown in Table 1. The birdcage was shielded with 1 oz. copper-clad FR4 mounted on a 3D printed ABS plastic cylinder (OD = 21.6 cm). Active detuning of the birdcage was achieved with a PIN diode in series with each tuning and matching network in order to open-circuit the coil during receive at two rungs 90 degrees apart [9]. The birdcage was matched and tuned to 17.24 MHz with an unbalanced network at each feed. Can baluns were used to suppress common mode currents [107]. An in-house built 3 dB quadrature combiner with an insertion loss of 0.6 dB was used for driving the quadrature ports [108], and a biasing signal of +5/-15V DC from a PIN diode driver was used to tune/detune the transmit coil during signal transmission and reception.

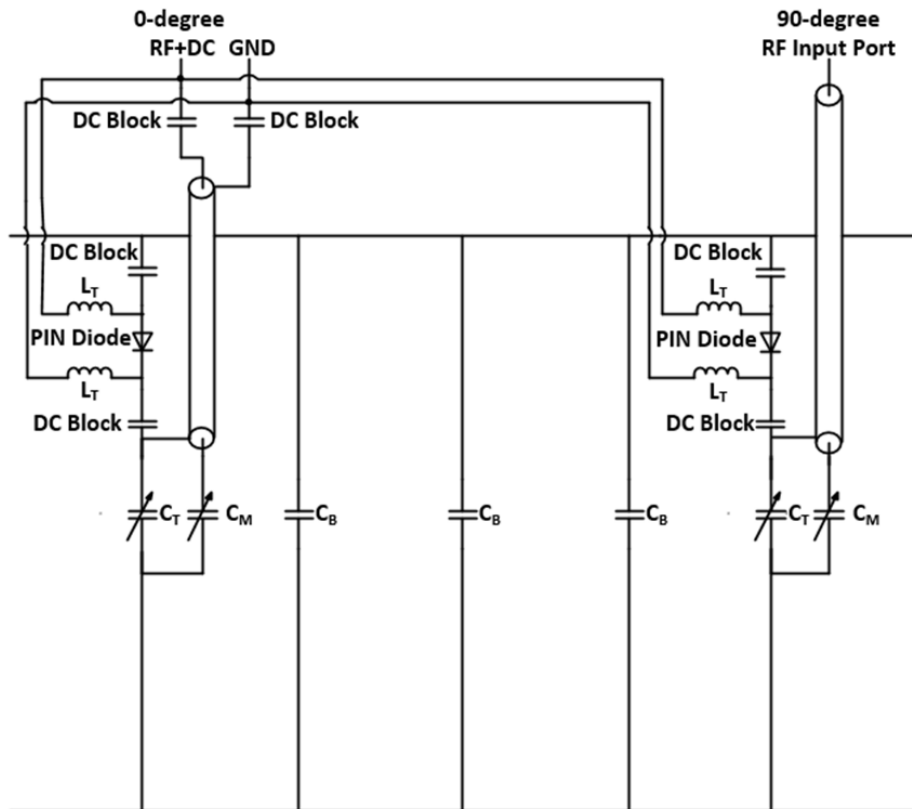


Figure 4. Circuit diagram of the transmit-only birdcage coil.

**Table 1. Coil component values and part numbers**

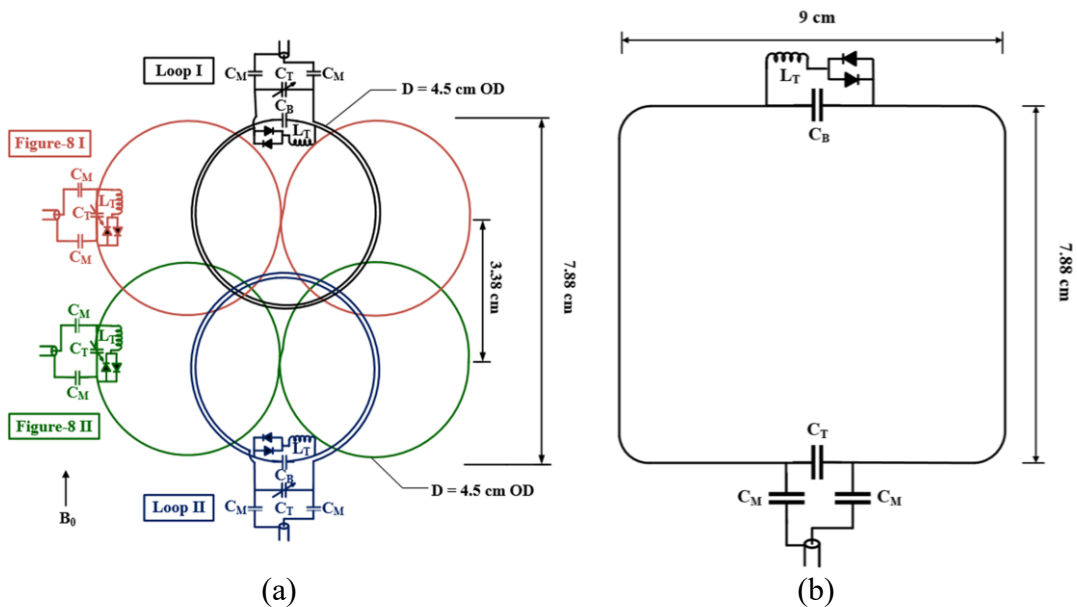
Component	Transmit Coil <sup>1</sup> (pF/nH)	Loop Coils <sup>2</sup> (pF/nH)	Figure-8 Coils <sup>3</sup> (pF/nH)	Comparison Coil <sup>4</sup> (pF/nH)
C <sub>T</sub>	(200-255)	(285-300)	(335.5-350)	716
C <sub>M</sub>	(44-99)	47	39	120
C <sub>B</sub>	229	820		716
L <sub>T</sub>	15,000	(65-101)	270	(83 – 128)
DC Block	6,800			

Fixed Capacitor	Variable Capacitor	Inductor	Diode
Passive Plus 1111C <sup>1,2,3,4</sup>	Voltronics NMAT55HVE <sup>1</sup>	Coilcraft 1812CS <sup>1</sup>	MACOM MA4P7441F- 1091T <sup>1</sup>
TDK, CGA 1000V <sup>1</sup>	Sprague Goodman SGC3S200NM <sup>4</sup>	Coilcraft 164 <sup>2,4</sup>  Coilcraft 2222SQ <sup>3</sup>	ON Semiconductor MBD701 <sup>2,3,4</sup>

All capacitances are show in pF while inductances are shown in nH. Note that values shown in parenthesis are tunable within the listed range either due to the value of the tunable component or combined with a fixed element. The part number and corresponding coil are denoted by superscripts.

The four-element receive array consisted of two figure-8 and loop sets (outer diameter = 4.5 cm) with their centers offset by 3.38 cm as shown in Figure 5. The design was etched 0.5 cm into the bottom side of a 3D printed sled (radius = 7.35 cm, aperture angle = 133°) for ease of construction with 21 AWG copper magnet wire and to ensure patient isolation from the circuitry. The sled’s design raised the center of the receive coil elements 2.5 cm away from the surface of the birdcage coil into the homogeneous region found from the previously described  $\Delta B_0$  maps. The two loops were constructed with two turns of wire after this was found to provide improved performance over a single loop [109]. The additional length of wire required the use of an additional distributed capacitor. Passive detuning traps were included on all receive elements. A balanced



**Figure 5. Circuit diagrams of four-element array and comparison coils**  
 (a) 4-element array configuration consisting of the loop and figure-8 coil pairs with associated passive detuning circuitry and match/tune networks. (b) Single, large comparison coil utilized for comparison to the four-element array.

configuration was used for both the figure-8 and loop coils to match and tune them to 17.24 Mhz. Can baluns were attached to each receive channel.

An advantage of this four-element configuration is that the two loop coils could be overlapped for decoupling, and the two figure-8 coils could similarly be positioned to decouple them from each other and from the loops. This enabled the use of off-the-shelf 50-ohm low-noise preamplifiers rather than low-impedance decoupling preamplifiers.

For comparison purposes, a single loop coil with overall dimensions equivalent to the four-element array was constructed, as detailed in the schematic in Figure 5. Passive



detuning traps were utilized to detune the coil during signal transmission. The coil was matched and tuned to 17.24 MHz with a balanced match configuration.

The coils were assessed on the bench by measuring the  $Q$ ,  $S_{11}$ , and  $S_{12}$  using an Agilent E5071C network analyzer. The -7 dB method was used for measuring the  $Q$  with and without a phantom [110]. Measurements for the receive coils were taken with the receive coils mounted in the transmit coil.

### **II.1.3.3 Phantom Design**

A cylindrical  $^{31}\text{P}$  physiological concentration phantom (length = 13.5 cm, diameter = 7.5 cm), used to simulate *in vivo* human skeletal muscle with PCr, Pi, and three ATP peaks, was made with 34 mmol/L phosphocreatine, 8.1 mmol/L ATP, 4.6 mmol/L Pi [111]. 0.5 mg sodium azide was added to prevent bacterial growth and the subsequent faster decay of the respective  $^{31}\text{P}$  compounds in the phantom. The conductivity and pH of the phantom were 0.95 S/m and 7.07, respectively, with the pH closely matching that of resting muscle [111]. Signal averaging was required with use of this phantom to accurately distinguish the  $^{31}\text{P}$  compounds from the baseline noise. Therefore, a second cylindrical phantom was constructed for testing and calibration that did not require averaging. The calibration phantom consisted of 85% phosphoric acid, which provided a strong, singular inorganic phosphate spectral peak observable with only one acquisition.

### **II.1.3.4 NMR Protocols**

The specific parameters used for the spectroscopy scans were as follows: excitation frequency = 17.24 MHz, repetition time = 4 s; sampling rate = 50 MSPS/channel for 4 channels; acquisition time = 0.512 s. All data was directly stored, and then later

digitally demodulated in MATLAB® in the Fourier domain to remove all points except the 5120 points surrounding the center frequency, reducing computation time during post-processing.

A 90° tip angle was found with a 300 μs pulse duration,  $V_{0-P} = 180$  V. Shimming with the linear gradient coils was then manually performed to either simultaneously minimize the linewidth of both Loops I and II, as denoted by Figure 5 for the array or the single receive element, depending on the transmit/receive configuration. When performing comparison tests of the array and single element receive coil, the shim values were minimized for each receiver system, and the same placement in the bore was used for both the single element receive coil and the array. Comparisons of the signal-to-noise ratio (SNR) and linewidths of the array and the single, large receive element were performed using the <sup>31</sup>P physiological phantom, specifically observing the PCr peak, using two averages with a repetition time of 30 seconds to ensure full relaxation.

Following shimming and power calibration, the tip angle was set to approximate the Ernst angle for PCr at 1.5T for a 4 s repetition time (Ernst angle = 59°) [112, 113]. This resulted in a 205 μs pulse duration or 16.6 mW average power per cycle, which was used for the *in vivo* experiment to increase the steady-state SNR.

After completing the calibrations, a healthy female volunteer underwent four consecutive scans to determine the feasibility of obtaining clinically relevant spectra from the gastrocnemius/soleus muscle group using our experimental setup. For the purposes of obtaining a T1 partial saturation correction factor, the first scan utilized the 205 μs pulse duration for twelve acquisitions with a repetition time of 30 seconds [114]. The repetition

time was then reduced to 4 seconds, four dummy scans were run to allow for steady state magnetization to be reached, and then data was collected at rest for six minutes. The volunteer was then directed to apply and maintain plantar flexion against a custom non-magnetic foot flexion stand with a pulley and bucket system weighted with 15 lb. for the duration of six minutes. Spectra were acquired during the six-minute exercise and for six minutes following the exercise to capture the metabolic recovery. The study protocol was approved by the Texas A&M University Institutional Review Board (IRB Number: 2016-0748F) and written consent was obtained from the participant.

#### **II.1.3.5 Data Processing**

Following digital demodulation, data from each channel were individually averaged in the time domain using a moving average of length 2, zero-padded to 15,360 points, and then were manually phased with zero-order and first-order phase corrections. The PCr peak was utilized as a reference point for aligning the frequency content of each channel before combination. Multi-channel data was then combined with the SNR weighting combination method recommended in [57, 115], which multiplied each channel's spectra by a weighting factor equal to its SNR divided by the square root of the sum of the SNR square of all channels. The SNR was calculated as the peak height of PCr divided by the standard deviation of the noise located in the range of 60 ppm to 160 ppm from PCr (0 ppm), where there were no discernable peaks. Data were exported to jMRUI for peak quantification with the time-domain fitting routine, AMARES [29, 116].

Within the AMARES algorithm, all peaks were fitted as Lorentzian peaks. Prior knowledge relationships reflecting J-coupling interactions, such as identical amplitude for

the respective doublets of  $\alpha$ -ATP and  $\gamma$ -ATP and the amplitude ratio of 1:2:1 for the triplet of  $\beta$ -ATP, were implemented according to the method described by Deelchand et al. in their protocol [105]. The zero-order and first-order phases were constrained to between  $-20^\circ$  to  $20^\circ$  and  $-5$  ms to  $5$  ms, respectively. The linewidth estimation parameter for the Pi, PCr, and the ATP metabolites was set to 8-10 Hz, 5-7 Hz, and 5-20 Hz, respectively, after finding that these parameters minimized the residual spectra obtained from subtracting the estimated fitted spectra from the original spectra and maintained the ratio of the Cramér-Rao lower bound per amplitude for all metabolites below a level of 20%, ensuring that the variance of unbiased estimators and attainable precision of the model were within a conservative threshold [117].

Corrections for T1 partial saturation of the PCr and Pi metabolites were made by multiplying the ratio of the respective fitted amplitude for the long TR (30 s) and the short TR (4 s) resting data sets by the fitted amplitude of the three short TR sets (baseline, exercise, and recovery) [114]. pH was calculated using the Henderson-Hasselbach equation relating the chemical shift between PCr and Pi [31]. A mono exponential curve was utilized for fitting the PCr recovery time constant [118].

## **II.1.4 Results**

### **II.1.4.1 Bench Measurements**

As seen in Table 2, the  $Q_{UL}/Q_L$  ratio is close to 1 for both the loop and figure-8 coils, indicating coil noise dominance. This is common for low field, small surface coils, as shown by Kumar et al. [119], but also presents an area where improvements can be

made. As would be expected, the 9 cm x 7.88 cm large coil had the largest  $Q_{UL}/Q_L$ , indicating that it was more sensitive to sample-induced noise.

**Table 2. Quality factor of different receive coils.**

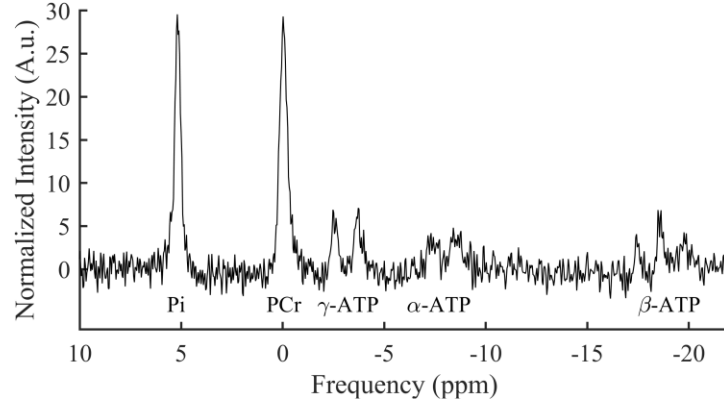
Coil	$Q_{UL}$	$Q_L$	$Q_{UL}/Q_L$
Loop I	163	153	1.06
Loop II	151	138	1.08
Figure-8 I	150	151	0.99
Figure-8 II	156	155	1.00
9 cm × 7.88 cm comparison coil	146	115	1.26

*Q* measurements of the different coil configurations were taken with ( $Q_L$ ) and without ( $Q_{UL}$ ) the  $^{31}P$  physiological concentration phantom.

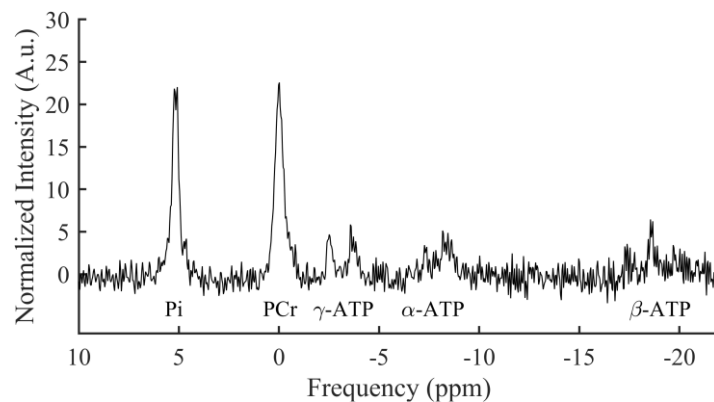
Coupling between the receive array figure-8 coils, loop coils, figure-8 and loop set I, and figure-8 and loop set II was -16.6 dB, -15.4 dB, -34.9 dB, and -18.6 dB, respectively.

#### II.1.4.2 Physiological Concentration $^{31}P$ Phantom Spectra

Figure 6 shows the spectrum resulting from the averaging of two acquisitions with a long TR of the physiological concentration phantom acquired from the array as compared to the single large comparison coil. The PCr SNR and linewidth of each channel and single large coil are shown in Table 3. The first loop, figure-8 set had a higher SNR than the second loop, figure-8 set. The array combination method provides a weighted influence for the overall combined spectra. This is seen with the combined linewidth in Table 3 being less than that of Loop I, even though Loop I had the highest SNR. Thus, the overall SNR is improved while the linewidth sees more of a weighted averaging effect.



(a)



(b)

**Figure 6. Normalized spectra of the  $^{31}\text{P}$  physiological concentration phantom**  
 (a) S/N weighting method combination of the 4-element array, (b) single large comparison loop. Data is shown with two averages and is normalized based on the standard deviation of the noise from the range of 60 ppm to 160 ppm.

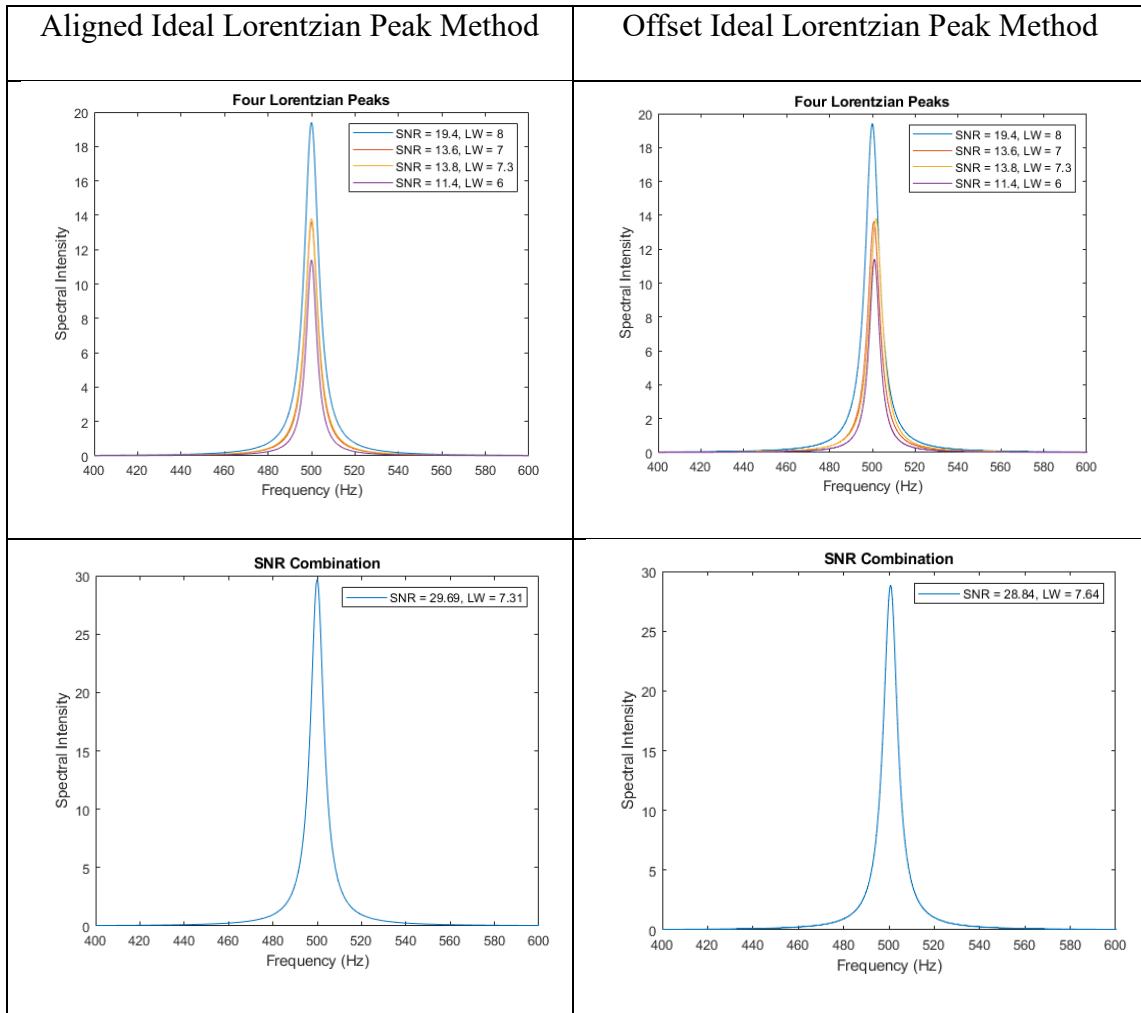
Additionally, aligning the frequency content of the individual channels presents an improvement in both SNR and linewidth, as seen in Table 4. This indicates that both aligning the frequency content of the individual channels and having a weighted combination allows the array to compensate for inhomogeneities in the  $B_0$  field for an

improved spectrum. In comparison to the single large surface coil, the SNR achieved by the array was 1.31 times higher and the linewidth reduced by 13.9%.

**Table 3. Coil performance of physiological concentration  $^{31}\text{P}$  phantom**

	PCr SNR	PCr LINEWIDTH (Hz)
Loop I	$19.4 \pm 0.9$	$8.0 \pm 0.4$
Figure-8 I	$13.6 \pm 0.4$	$7.0 \pm 0.5$
Loop II	$13.8 \pm 0.9$	$7.3 \pm 0.5$
Figure-8 II	$11.4 \pm 0.7$	$6.0 \pm 0.7$
SNR Combined Array	$29.8 \pm 1.1$	$7.4 \pm 0.5$
Comparison Coil	$22.7 \pm 1.7$	$8.6 \pm 0.3$

**Table 4. Comparison between combining Lorentzian peaks with and without alignment of the peaks.**



### II.1.4.3 In Vivo Spectra

A stack plot over the course of the entire 18-minute protocol was generated using a sliding window over two averages and 5 Hz line broadening applied after channel combination for easier visualization (Figure 7). The plot shows the characteristic decrease in PCr and increase in Pi at the beginning stage of the local exercise [77, 120]. The



resulting AMARES fit of the amplitudes of PCr and Pi, shown in Figure 7 after multiplication by the T1 partial saturation correction factors of 1.53 for PCr and 1.24 for Pi and normalized by the resting PCr average, show the progression of the two metabolites throughout the course of the exercise and recovery protocol with error bars representing the Cramer-Rao bounds. The mean and standard deviation of the Cramer-Rao bounds for Pi were  $8.93 \pm 2.79\%$  of the amplitude with a max bound of 15.89%, while bound values for PCr were  $2.25 \pm 0.26\%$  of the amplitude with a max of 2.96%. The resting mean pH of  $7.04 \pm 0.02$  was within reported literature values for a healthy individual [120]. Although the actual PCr/Pi ratio for the resting states, shown in Figure 7, is not conclusive, a distinct change is evident and less variance of the PCr/Pi ratio was observed during the exercise portion of the protocol compared to the resting stages due to the increasing concentration of the Pi metabolite during this period. The fitting of a mono exponential curve to the PCr recovery showed a recovery time constant of 32 seconds, which was within the healthy cohort range as denoted in an experts' consensus paper by Meyerspeer et al. [32]. Slight, exercise-induced acidosis, as determined by a drop in pH of approximately 0.3, was observed by the end of exercise, indicating a more complex fitting mechanism might be appropriate.

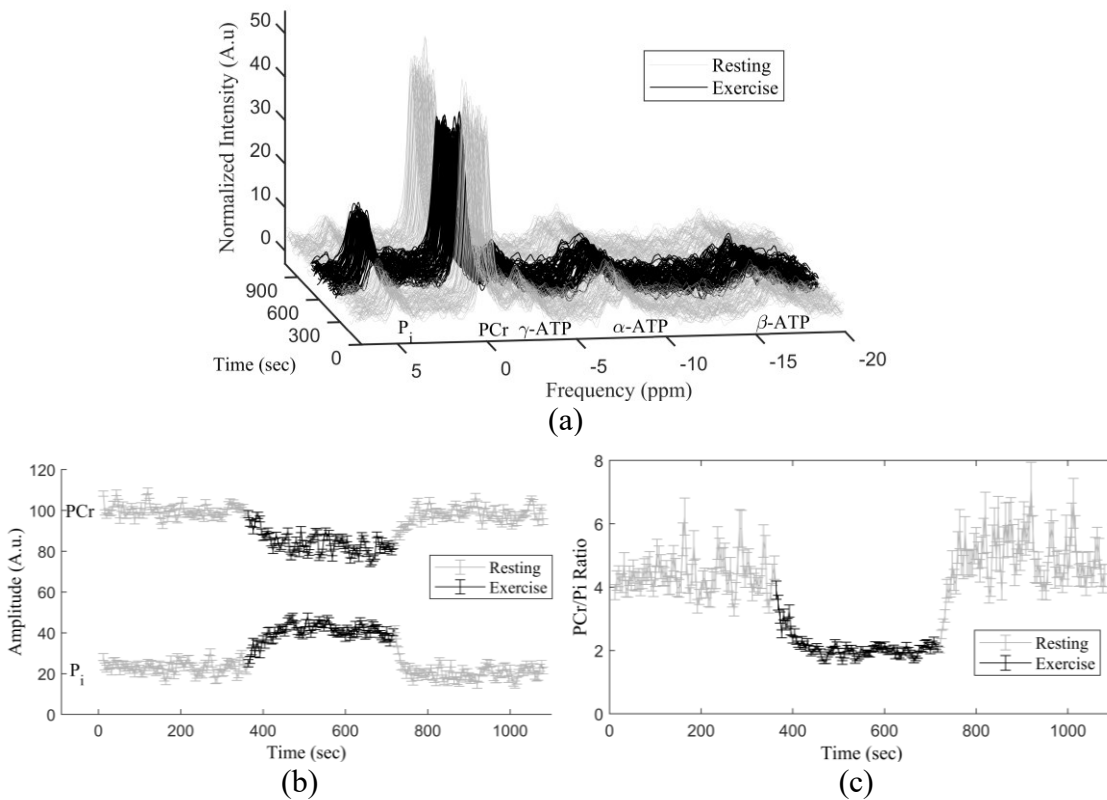


**Figure 7. *In vivo* data from healthy volunteer.**

(a) Stack plot showing spectra obtained from the gastrocnemius/soleus muscle group during the baseline, exercise (black), and recovery stages of the exercise protocol. A 2-average sliding window average and 5 Hz line broadening was used for each data visualization with spectra normalized to the standard deviation of the noise from the range of 60 ppm to 160 ppm. (b) The progression of the T1 partial saturation corrected PCr and Pi peak amplitude results for all phases of the protocol normalized to the resting PCr signal intensity. (c) PCr/Pi ratio calculated during the phases of the protocol.

## II.1.5 Discussion

### II.1.5.1 Coil Performance

To explore the non- $^1\text{H}$  spectroscopy capabilities of the ONI 1.0T extremity magnet, a four-element receive array was used to increase the SNR and minimize the

linewidth in comparison to a single element receive coil. In our previous work, a more significant improvement was observed between the four-element array and the comparison coil [103]. In that work, the first order shimming was performed solely with the array coil, optimizing the linewidth across the two loop coils. Shim settings were not changed when switching to the single comparison coil. The shimming methodology was changed for this work to individually shim with the single large comparison coil for the data obtained with the comparison coil and then to shim with the array for data obtained with the array. Because the comparison coil covered a larger area than the array elements used for shimming, this provided a fairer comparison between the two configurations. The array has its highest sensitivity in the middle of its footprint, corresponding to a smaller more homogeneous part to the magnet. The benefit of having smaller coils with the array is seen by having smaller regions over which to shim and improved linewidth for the combined spectrum.

As was recorded in Table 2, sample noise dominance was not the case for this particular setup. Therefore, SNR improvements potentially could be obtained with thicker wire or printed circuit boards. This geometry did provide the highest channel count and relative localization to the gastrocnemius/soleus muscle group without the need for decoupling preamplifiers. Although the SNR improvement was not as high as desired, the improvement from the four-element array enabled fewer averages and therefore a temporal resolution below the recommended 10 second threshold for observing metabolic dynamics [32, 121]. The benefits of using an array for this type of application with respect to SNR and linewidth should only increase with higher channel counts.

### II.1.5.2 In Vivo Quantification Challenges

Based on the variance of the PCr/Pi ratio during the resting states, the use of the 1.0T magnetic field strength neared the low end of the sensitivity limit for reliable fitting of all metabolites except for PCr. The almost doubling of SNR of Pi during the exercise period enabled better fitting during this portion of the protocol. Further improvement of the SNR for Pi and the ATP metabolites was considered through different scan parameters, but calculations showed that reducing the repetition time to one second would further increase the data volume and provide as little as 3% SNR gain per unit of time for Pi, even with the tipping angle adjusted to the Ernst angle for the new repetition setting [122].

### II.1.6 Conclusion

The feasibility of using a 1T extremity scanner for *in vivo* dynamic  $^{31}\text{P}$  spectroscopy has been demonstrated through the acquisition of  $^{31}\text{P}$  spectra from a healthy volunteer using a custom four-element array and associated hardware. The experimental hardware enabled a temporal resolution of eight seconds to obtain spectra with sufficient SNR to detect metabolic changes in exercising muscle from  $^{31}\text{P}$  MRS. This study indicates a promising future for the use of low-cost platforms for *in vivo*  $^{31}\text{P}$  spectroscopy studies, a deviation from most work currently performed [32].

Additional optimizations regarding data acquisition, such as repetition time and pulse sequences, and data processing techniques for increasing the SNR, will be pursued. To further probe achievable signal levels for the extremity scanner, dual-tuned  $^1\text{H}$  and  $^{31}\text{P}$  coils are being developed in order to utilize the nuclear Overhauser effect [123]. The increased  $^{31}\text{P}$  signal and capabilities for anatomical imaging without having to move the

patient will benefit data analysis and enable better correlation to the underlying physiology through the selection of coils with sensitivity profiles nearest the target tissue. Whereas the current receive array design was chosen for its number of channels and use of standard 50-ohm low noise preamplifiers, alternative configurations of receive coils employing preamplifier decoupling preamplifiers could provide increased utility. The reduction of coil losses could immediately and practically be achieved through utilizing printed circuit board traces or thicker wire. Additionally, cooling structures with liquid nitrogen or helium could offer more complex improvements. As these cooled technologies are further developed, it is feasible that their cost and complexity would be reduced and enable widespread use within coil design, especially at lower field strengths [124, 125]. Adjustment of the exercise protocol to induce a greater PCr depletion without the presence of exercise-induced acidosis would benefit fitting of recovery constants.

The protocol utilized for the *in vivo* patient study can be found in Appendix A.

## **II.2 A Three-Element Triple-Tuned Array Implemented with Switchable Matching and Tuning**

### **II.2.1 Synopsis**

This work describes a geometrically decoupled three-element array triple-tuned for  $^1\text{H}$ ,  $^{13}\text{C}$ , and  $^{31}\text{P}$  at 3T implemented with switchable matching and tuning using PIN diodes. These particular nuclei were chosen to demonstrate the frequency range of the method, but the approach is extendable to any nuclei of interest. Although the Q of the coils was degraded by the switching network, the use of PIN diodes enabled straightforward tuning and development.

### **II.2.2 Introduction**

The inherently low signal-to-noise (SNR) of non- $^1\text{H}$  imaging and spectroscopy studies have led to the development of specialized techniques and hardware to overcome these limitations, including the use of multi-nuclear array coils. Several methods have been used to tune coils to multiple frequencies: the use of traps [17, 18], varactor diodes in parallel with fixed capacitors [126], and switching mechanisms through the use of MEMS or PIN diodes [19, 20, 127-130]. MEMS and PIN diodes for switching applications have been compared for Q, power handling, and loss [131, 132], and although MEMS technology is improving and shown to be a viable option for different MR applications [133], costs of these devices and size of the footprint required could potentially limit their use in array coils requiring multiple switches. Thus, this work describes a geometrically decoupled three-element array triple-tuned for  $^1\text{H}$ ,  $^{13}\text{C}$ , and  $^{31}\text{P}$  at 3T implemented with switchable matching and tuning using PIN diodes. These three nuclei were chosen to

demonstrate the flexible frequency range of the method, but the approach is extendable to any nuclei germane to the scientific study of interest.

### **II.2.3 Methods**

Three 47 mm diameter loops were made of 18 AWG nylon-coated copper wire (8049, Belden) with “jumpers” at coil intersections. Each loop was attached to a double-sided copper clad FR4 board containing switching circuitry. The switching circuitry consisted of fixed (1111C, Passive Plus) and variable (SGC3S, Sprague Goodman) matching/tuning capacitors for each frequency, PIN diodes (MA4P7470F, M/A-COM), and RF chokes (1812LS, Coil Craft), detailed in Figure 8. A category 5 cable bundle with six DC lines was attached to each coil to allow switching between the three frequencies of interest at 3T: 32.13 MHz ( $^{13}\text{C}$ ), 51.72 MHz ( $^{31}\text{P}$ ), and 127.74 MHz ( $^1\text{H}$ ). Each DC cable bundle was connected to two DC lines, corresponding to the  $^{31}\text{P}$  and  $^{13}\text{C}$  frequencies, coming from the “bias distribution board”, as shown in Figure 8 and Figure 9. Each DC line had an RG174 co-axial cable (7805, Belden) with a BNC connector (031-315-RFX, Amphenol) connected to the power supply, an RF choke, and a current-limiting resistor (CRCW0402 Series, Vishay). Each DC line on the bias distribution board was independently controlled to switch between the three frequencies for each element. When all DC lines were connected to the power supply, all PIN diodes were biased to match and tune each coil to the  $^{13}\text{C}$  frequency;  $^{31}\text{P}$  tuning and matching was achieved by disconnecting the  $^{13}\text{C}$  DC lines; DC current was removed for matching and tuning to the  $^1\text{H}$  frequency.

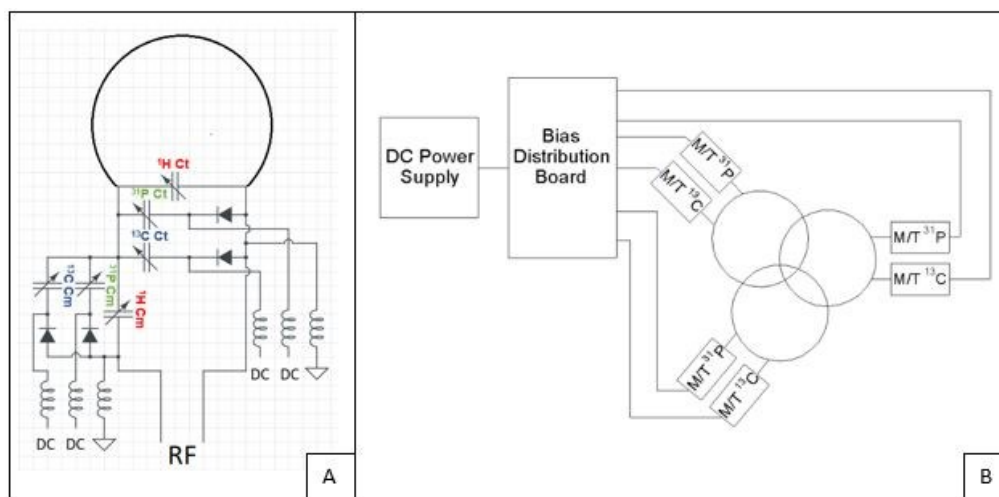


**Figure 8. Circuit diagrams of triple-tune coils and bias networks.**

(A) Circuit diagram for a single, triple-tuned loop coil. The  $^1\text{H}$  frequency configuration utilizes an unbalanced match/tune network and does not require any DC current or PIN diodes. DC current activation of only the  $^{31}\text{P}$  ports enables the  $^{31}\text{P}$  match/tune capacitor to become in parallel with the  $^1\text{H}$  capacitors. Activation of both the  $^{31}\text{P}$  and  $^{13}\text{C}$  DC lines enables the coil to be tuned/matched to the  $^{13}\text{C}$  frequency. (B) System diagram for the array elements and associated bias distribution board and DC power supply.

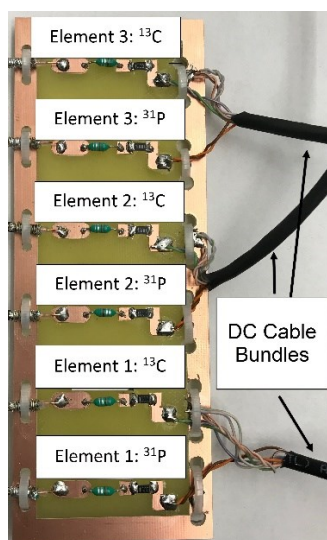


**Figure 9. Bias distribution board**

DC current is input to the board (left) and then run through a choke and 100 Ohm resistor. A category 5 cable bundle with six 24 AWG wires was used to carry DC to the respective  $^{13}\text{C}$  and  $^{31}\text{P}$  match/tune switching circuits for each coil.



Each element was matched and tuned separately, and all three were mounted on an acrylic former and positions adjusted for decoupling. Single-tuned coils for each frequency were created for comparison. Benchtop measurements of  $S_{21}$  coupling,  $S_{11}$ , and Q measurements were obtained using an Agilent Technologies Network Analyzer (E5071C).

#### II.2.4 Results and Discussion

The constructed three-element array and switching networks are shown in **Error! Reference source not found.** Matching and tuning for each element at each frequency was better than -20.1 dB, as shown in **Error! Reference source not found.** A video of the coils switching frequencies is available at <https://youtu.be/rvtAmE41-L0>. The switching mechanism enabled straightforward tuning at the different frequencies and limited additional coil resonances. Q measurements, shown in Table 5, reveal a significant loss in Q for the triple tuned coils. The drop in Q pertaining to all three frequencies can be attributed to the additional circuitry needed for switching. Coupling measurements reflect that the positioning of the array coils was optimized for the  $^1\text{H}$  frequency. Although the circuit path for  $^{31}\text{P}$  and  $^{13}\text{C}$  was similar to that of  $^1\text{H}$ , the additional circuit path needed for the capacitors could be the cause for the increased coupling at these two frequencies.

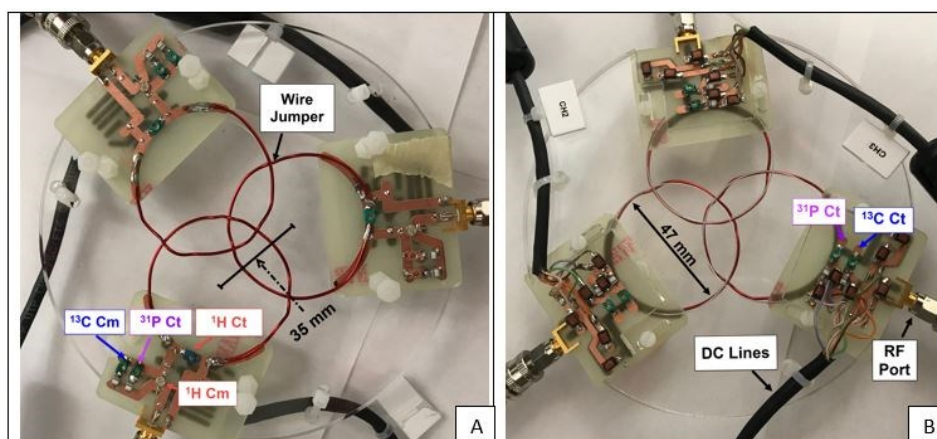


**Figure 10. Top and Bottom views of the triple-tuned switchable array**

The top view of the array shows the variable matching and tuning capacitors for the  $^1\text{H}$  frequency, and the variable match capacitors and PIN diodes for the  $^{31}\text{P}$  frequency and the  $^{13}\text{C}$  frequency. (b) The bottom view of the array shows the variable tuning capacitors and PIN diodes for the  $^{31}\text{P}$  frequency and the  $^{13}\text{C}$  frequency, all the RF chokes and DC lines for the switching network, and the RF port for each element.

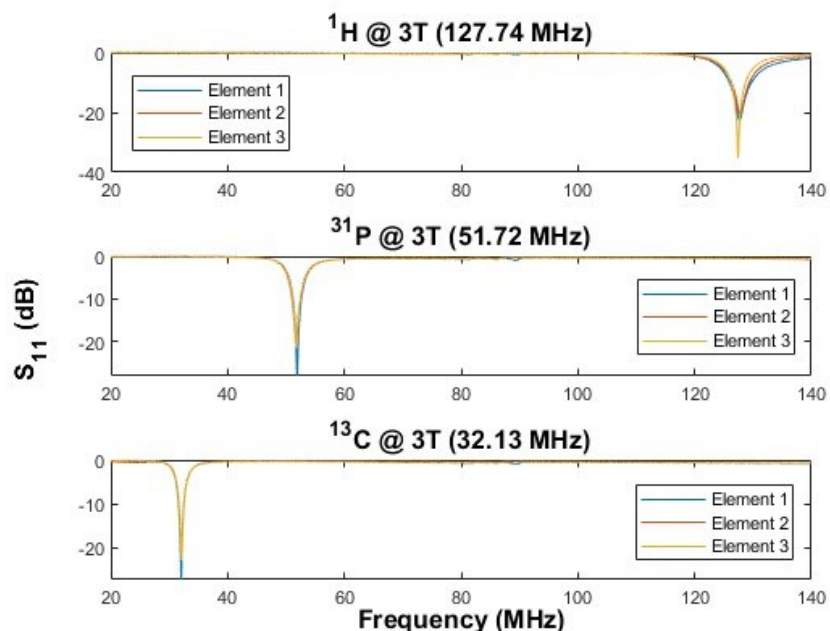


**Figure 11.  $S_{11}$  reflection measurements**

$S_{11}$  reflection measurements are shown for each element and frequency with all three elements positioned in the final array design.

**Table 5. Q-factor results for the isolated triple-tuned elements and that of a single-tuned element as well as coupling measurements of the array coils per frequency.**

Frequency	Q - Factor				Coupling		
	Element 1	Element 2	Element 3	Single Tuned Coil	$S_{12}$	$S_{13}$	$S_{23}$
$^1\text{H}$	28	30	29.3	94.9	-29	-23.5	-26.3
$^{13}\text{C}$	30.6	29.1	27.5	165	-14.2	-19.6	-16.2
$^{31}\text{P}$	27.7	29.5	29.1	95.1	-14.4	-20.1	-16.6

## II.2.5 Conclusion

A three-element triple-tuned switchable phased array coil design was demonstrated with benchtop measurements. Inter-element coupling was sufficient between the different channels. The use of PIN diodes enabled straightforward tuning and development, but this was achieved at the expense of the Q of the coils. In its current form, the increase in sensitivity achieved with the array is essentially canceled by the loss in Q. Therefore, future directions include exploring ways to improve the Q, such as using an inductor in series with the PIN diode to tune to the  $^1\text{H}$  frequency as suggested by Choi [128]. Optimizations for the number of breaks and size of the coil can also be performed to influence the Q at different frequencies [129]. Following optimizations, imaging and spectroscopy studies will be performed to validate benchtop performance and the use of switchable, triple-tuned phased array coils.

## **II.3 Characterization of a Multi-channel Receiver for Broadband System**

### **II.3.1 Synopsis**

This work describes the characterization of a Pentek 78862 multi-channel receiver for use with a broadband transceiver system to increase multi-channel, multi-frequency capabilities. Due to the wide span of frequencies at which NMR signals from different nuclei are obtained and the low sensitivity of the method, transceiver hardware must possess good broadband performance and still be able to provide multi-channel capabilities to benefit from the extra sensitivity that array coils provide. In comparison tests with the current receiver, the Pentek 78862 provided comparable SNR with output files that were 16 times smaller due to its DDC function. The 8-channel channelizer functionality expands the theoretical acquisition limit from 4 channels up to 32, provided the signals are at different frequencies bands and can be split amongst the four input ports of the card. The added functionality of this card greatly benefits data acquisition through the multi-channel capabilities, data throughput from smaller data files, and eases post-processing data handling times and burden.

### **II.3.2 Introduction**

Due to the varied gyromagnetic ratios of NMR-active nuclei and different magnetic field strengths at which magnetic resonance experiments are performed, the frequency span at which MRI/MRS are performed can vary by 10s or 100s of MHz's when considering interrogating different nuclei. This places a difficult requirement on the hardware that is responsible for both transmitting and receiving signals at the respective MR frequency, especially when considering that MRI/MRS is typically considered a low

sensitivity method. Maintaining good broadband performance without the introduction of noise within the frequency bandwidth of interest can be difficult and consequently detrimental to obtaining quality results. Standard clinical MR scanners have utilized narrowband transmitters and multi-channel receivers for  $^1\text{H}$  interrogation, as it benefits from the largest gyromagnetic ratio and natural abundance. Limiting a scanner to a single nucleus makes hardware development easier but drastically impedes the amount of information that can be gained from additional nuclei. The adoption of broadband transceivers is increasing, but most scanners still don't have the number of broadband channels that  $^1\text{H}$  currently enjoys. Efforts by the MRSL group to address this issue have involved developing frequency translation units to utilize the multiple  $^1\text{H}$  channels for other nuclei [134] and by creating a portable transceiver system that provides multi-channel transmit and receive capabilities [106].

This work details the characterization of an alternative multi-channel receiver card for use with the aforementioned portable receiver system to expand multinuclear capabilities and improve data handling and throughput.

## **II.3.2 Methods**

### **II.3.2.1 Receiver Cards for Comparison**

The receiver board that was originally incorporated into the broadband spectrometer was the Ultraview AD16-250x4 (Ultraview Corp, Berkeley, CA), which provided input four channels that could be sampled at a rate between 40 and 250 MS/s.

The comparison receiver board was the Pentek 78862, which provides four analog input channels that can sampled at a rate of 200 MS/s. This board provides DDC

capabilities and 8-channel multiplexing with additional multi-band DDC capabilities for each channel. The Pentek acquisition card maintains two paths for signal acquisition: a wideband and a narrowband pathway. The wideband pathway is limited to decimation levels from 2 to 32, while the narrowband pathway can decimate data from 16 to 1024. The bandwidth of the output data is adjusted based on the decimation level according to Eq. II.3.1, where  $F_s$  is the sampling frequency and  $D$  is the decimation level.

$$BW = 0.8 * \frac{F_s}{D} \quad \text{Eq. II.3.1}$$

### II.3.2.2 Characterization Tests

A  $^{31}\text{P}$  spectroscopy experiment performed on the 1T ONI scanner was utilized for the experimental setup for phase stability tests, SNR, and linewidth comparison purposes. The same coil setup described in Chapter II.1 was utilized for this experiment. For phase stability and direct comparison purposes between the two cards, only a single receive coil (Loop 1 in Figure 5) was used to minimize the amount of data required for processing and to reduce data combination complexity. Phase stability tests were performed by setting different repetition times of the MR experiment and acquiring multiple acquisitions to ensure the resulting FIDs were in phase. For direct comparison tests, a noise only scan (Scan 1) was acquired before running a scan to obtain data with signal (Scan 2) from the first acquisition card. Then the two scan process was repeated with the second acquisition card following a time frame, such as 30s – 1 min, to allow for signal  $T_1$  regrowth to its fully relaxed state. Note: all cables were kept the same up to the point where the cable coming from the coil was directly attached to the specific receiver. Data was also gathered

synchronously with both cards using a 3 dB splitter (Minicircuits, ZSC-2-1), but this method appeared to negatively influence the results obtained with the Ultraview card when compared to data received with the Ultraview card without the use of a splitter. Therefore, sequential testing of the different cards was utilized as the method of choice.

The spectral SNR was measured as the peak height (Scan 2) divided by the standard deviation of the noise in the region of the excitation bandwidth of the pulse (Scan 1). The linewidth was defined as the bandwidth at the full width half maximum of the peak.

Following the direct comparison tests, the functionality of the broadband system, such as decimation and the ability to receive multiple sub-band frequencies on the same channel were tested. Decimation was tested using the  $^{31}\text{P}$  MR experimental setup and the wideband and narrowband functions of the Pentek card. Tuning of the narrowband sub-channels to the target frequencies was adjusted through a vector within the header file of the narrowband code. The 8-channel channelizer was tested with a single channel digitization experiment using the broadband transceiver system, specifically the AD9959 card, to generate two sinusoidal frequencies that were combined using a combiner (Minicircuits, ZFSC-4-1-S+) before sub-channel digitization with sub-channels 2 and 7.

Experimental parameters for all the different functionality and comparison tests are shown in Table 6.

**Table 6. Experimental parameters for tests used to evaluate the receiver cards.**

Test	Phase Stability (Pentek <sup>1</sup> )	SNR & Linewidth Comparison (Pentek <sup>1</sup> & Ultraview <sup>2</sup> )	Decimation Tests (Pentek <sup>1</sup> )	Multi-frequency sub-band and different channels
Phantom/Signal Source	85% phosphoric acid phantom	85% phosphoric acid phantom	85% phosphoric acid phantom	Broadband Transceiver (AD9959)
Sampling Type/Rate (MHz)	Decimation = 32, Rate = 50 MS/s	Decimation = 32 <sup>1</sup> , Rate = 50 MS/s <sup>1,2</sup>	Wideband decimation = 32 Narrowband decimation = 32, 128	Narrowband decimation = 64 Rate = 120 MS/s
F <sub>C</sub> (MHz)	17.24325	17.24325	17.24325	17.24, 42.57
LO (MHz)	17.2429	17.2429 <sup>1</sup>	17.2429	
T <sub>acq</sub> (s)	0.512	0.512	0.512	0.005
TR (s)	5, 30	30	30	N/A
N <sub>avg</sub>	1	4	4	1
N <sub>transients</sub>	4	4	4	0
Pulse type	Hard	Hard	Hard	Hard
Pulse duration (μs)	300	300	300	5000

### II.3.3 Results and Discussion

#### II.3.3.1 Phase Stability Tests

The initial configuration of the Pentek acquisition card resulted in a clock drift that became increasingly pronounced for longer repetition times, as shown in Figure 12. As signal averaging is performed in the time domain, phase stability of signals between different acquisitions is critical to achieve the  $\sqrt{N}$  SNR improvement with N transients. Adjustment of the `adcgatesrc` variable, which represents the ADC gate source, from expecting a gate source signal to a TTL signal for triggering was required to prevent clock



drift. The resulting in phase acquisitions are shown in Figure 13. Averaging of the four acquisitions provided an SNR improvement of 1.97, which more closely matches the expected theoretical improvement of 2.

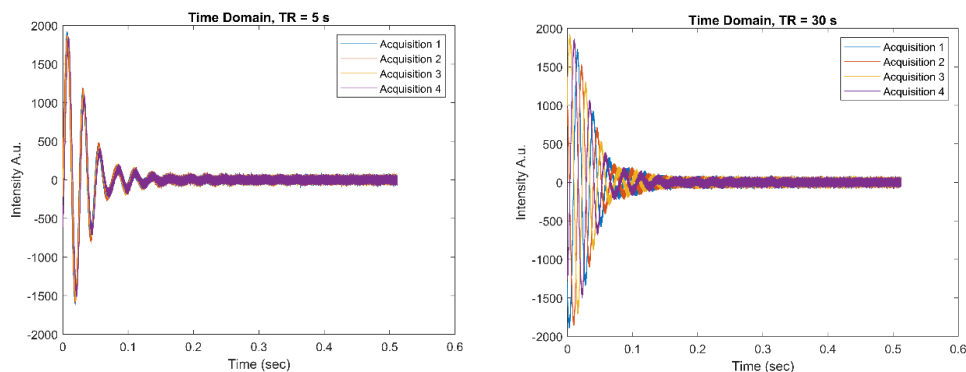


**Figure 12. Time domain FIDs for clock stability**

The time domain FIDs shown in each graph are the result of the acquisition of four different TR cycles. As the TR is increased, the signals steadily become more out of phase, as is evident by ability to distinguish the different colors for the FIDs plotted on top of one another.

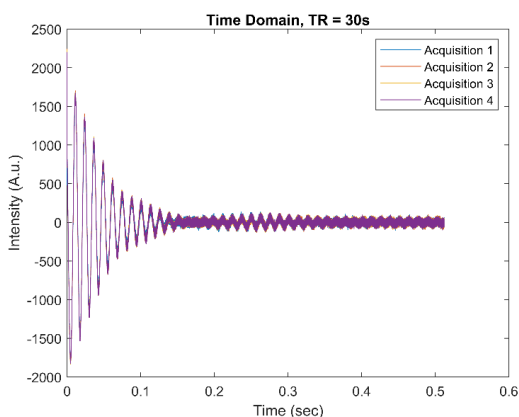


**Figure 13. In phase time domain FID**

Following the adjustment of the `adcgatesrc`, the time domain FIDs are now in phase with one another and show an increase according to the square root of the number of averages.

### II.3.3.2 Direct Comparison of Two Acquisition Cards

Several experimental trials were acquired to increase confidence in the comparison. As can be seen based on Table 7, the SNR had some slight variation based on the day that the data was acquired. Typically, the linewidth was larger for the Pentek data, which is thought to be due to the filter utilized during the decimation process. The values of the FIR filter were not adjusted during this testing but could be modified to provide a broader passband region. Overall, the SNR of the Pentek was within 1-3% of that of the Ultraview, which was deemed acceptable. Further investigation into improving the linewidth could be pursued through adjustment of the FIR filter settings.

**Table 7. Receiver card comparison of SNR and Linewidth across different dates**

Date	Receiver	Signal	Noise	SNR	Linewidth (Hz)
9/13	Ultraview – Direct sampling	6.36e9	510,626	12,455	5.63
	Pentek – wideband decimation 32	1.60e8	12,482	12,841	6.89
9/11	Ultraview – Direct sampling	6.89e9	537,044	12,820	5.58
	Pentek – wideband decimation 32	1.57e8	12,376	12,665	6.92

The difference in size of the data files that were created between the two cards was quite large. The Ultraview card, which was only able to directly sample the data, created file sizes on the order of 200.7 MB for an acquisition time of 0.512 s sampling at a rate of 50 MS/s. In comparison, the Pentek file size for the same conditions but with a decimation level of 32 was only 12.5 MB (data file size is only 16 times smaller due to acquisition of

I/Q data). This has large implications for data throughput during a clinical trial. In Chapter II.1, the repetition time was unable to be brought lower than 4 seconds for the selected experimental parameters due to data throughput. This prevented a lower repetition time from being used, which could have benefited the SNR through using a different Ernst angle tip and more averages [112, 122]. Calculations showed that an improvement of 3% and 1.4% for the Pi and PCr compounds, respectively, could have been had per unit of time by reducing the TR to 1 second. Therefore, the Pentek acquisition card provides better utility in terms of data throughput and storage when compared to the Ultraview acquisition card, especially when considering that the highest decimation setting was not even used for the direct comparison methods.

### II.3.3.3 Decimation and Multi-frequency Functionality Tests

A major difference in use between the wideband and narrowband pathway is determined by the filters that are applied to the data. A single FIR filter is utilized for the wideband pathway, while the narrowband undergoes an additional filtering pathway. The influence of the second stage of filtering is shown in Table 8 where the narrowband result with the same decimation level as the wideband function had at least a 1.5 times improvement in SNR with a similar linewidth. This improvement was primarily due to the additional filtering of noise and smaller bandwidth resulting from decimation.

**Table 8. Comparison of wideband and narrowband with varying decimation levels.**

Band and decimation selection	Signal	Noise	SNR	Linewidth (Hz)
Wideband – decimation = 32	1.30e+08	12481	10,437	8.33
Narrowband – decimation = 32	1.14e+08	6707	17,031	8.28
Narrowband – decimation = 128	2.92e+07	1591	18,390	8.09

The 8-channel channelizer function enabled successful isolation of the 17.24 and 42.57 MHz sinusoidal signals on sub-channels 2 and 7, respectively. The frequency domain plots are shown in Figure 14. Although this demonstration only highlights the use of a single channel's channelizer ability for two frequencies, this has implications for the total number of achievable channels that can be simultaneously received with this receiver. With the addition of frequencies shifters and appropriate filters and signal combiners, the Pentek card provides the capabilities to acquire up to 32 channels of data at a time at a single frequency or subdivided into various other frequencies. This would benefit simultaneous or interleaved multi-channel, multi-nuclear MR studies.

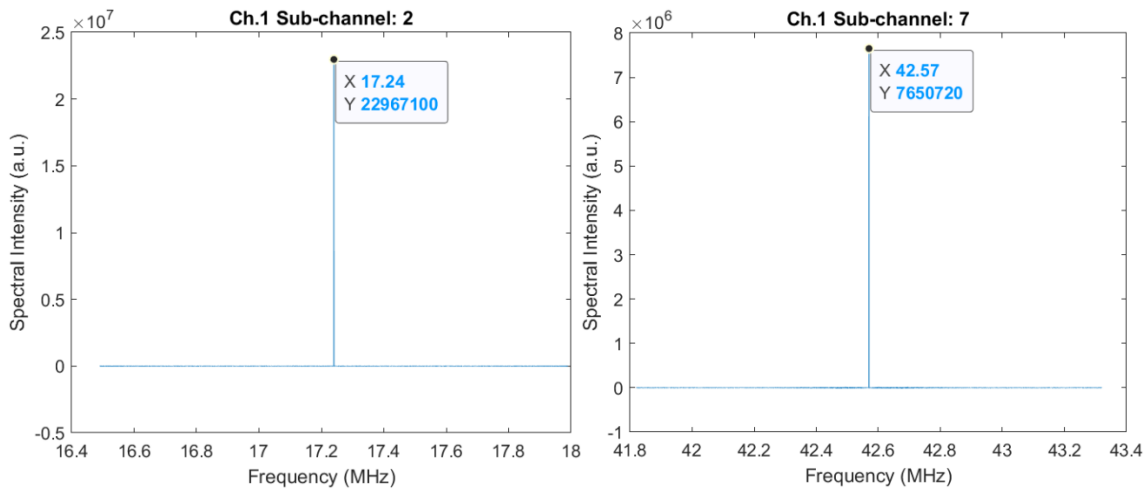


**Figure 14. Frequency domain plots of Pentek receive channels.** Frequency domain plots of sub-channels 2 and 7 acquiring  $^{31}\text{P}$  and  $^1\text{H}$  frequencies at 1T.

### **II.3.4 Conclusion**

The Pentek was able to be configured to properly work in sequence with the broadband transceiver system. In comparison tests with the Ultraview AD16-250 acquisition card, the Pentek 78862 data acquisition provided comparable SNR, albeit producing a spectrum with a larger linewidth. The ability to decimate the data using the DDC enabled for drastically smaller output files, easing the post-processing data handling. The 8-channel channelizer DDC function demonstrates the capabilities to acquire up to 32 channels of data at different frequencies, provided the data is combined in to the four input channels using external combination/frequency shifting hardware. Future work with this project involves adjusting the programmable FIR filters to determine if improvements to the linewidth could be made.

CHAPTER III  
LONGITUDINALLY TRANSLATABLE 32-CHANNEL COIL RING AND  
PREAMPLIFIER UNIT FOR INVESTIGATION OF 32X32 VOLUME FAST MRI  
DATA ACQUISITION

**III.1 Synopsis**

This work presents the instrumentation associated with a simplified design of a single, ring array composed of 32 overlapping rectangular coil elements and an associated add-on, radial preamplifier module to enable the physical longitudinal translation of the ring to mimic the full realization of the originally proposed 32 x 32 high density array configuration by Hutchinson and Raff. The performance of the array and associated preamplifier module were evaluated by benchtop measurements and through imaging of a homogeneous canola oil phantom. Benchtop measurements indicated good decoupling of the individual array elements, both through geometric and preamplifier decoupling metrics. Transverse images showed adequate active detuning and that the array provided sensitivity in the middle of the phantom, despite the small size of the individual coils. This system will provide a means to validating Hutchinson and Raff's theory through a 32-translation step experiment, which could have implications for obtaining full body imaging through a single echo acquisition thereby decreasing imaging time by orders of magnitudes.

## **III.2 Introduction**

“Parallel imaging” exploits the distinct spatial sensitivity patterns of multiple receiver coils to reduce MRI scan times [45]. The reduction in scan time stems from foregoing some steps of the filling of k-space, either through coil sensitivities and locations or through undersampling techniques. Operating at the ultimate acceleration of a single echo based on coil localization, however, has been explored only with surface planar imaging [69] despite the first theoretical prediction by Hutchinson and Raff for massively parallel MRI [135, 136]. The ultimate realization of this concept for three-dimensional imaging has ground-breaking implications, but up to this point, physical realization of the concept has not been implemented due to hurdles involved with depth sensitivity, signal-to-noise ratio, and decoupling of the dense array required for verification of the theory. Additionally, the task of elucidating spatial information from two different directions from array information with only a single slice selection gradient is daunting. This work presents the instrumentation associated with a simplified design of a single ring array composed of 32 overlapping rectangular coil elements and an associated add-on, radial preamplifier module to enable the physical longitudinal translation of the ring to mimic the full realization of the originally proposed 32 x 32 high density array configuration.

## **III.3 Methods**

### **III.3.1 Coil Design**

The 32 overlapping rectangular coils (length = 17.5 mm, width = 6.2 mm, overlap = 0.43 mm, trace width = 1 mm) were constructed on flexible, double-sided FR4

PCB's with ½ ounce copper. The boards were mounted on the inside of an acrylic former (ID: 16.51 cm). 24 AWG wire (8022, Belden) “jumper” wires were used on the outward facing coils for fine tuning of geometric decoupling between neighboring coils. A matching network designed by Reykowski et al. and shown in Figure 15, consisting of two shunt tuning capacitors ( $C_t$  and  $C_p$ ), a series matching capacitor ( $C_m$ ), and a series inductor ( $L$ ) were used to enable matching and tuning of the coils with the use of low noise preamplifiers [14]. The addition of a shunt PIN diode after the matching network enabled active detuning of the coils. Component values and part numbers are shown in Table 9. A half-wavelength of RG 174 cable (7805, Belden, length = 42 cm) connected the coils to the preamplifier box. Bazooka baluns comprised from 5 mm polyethylene tubing encased in a 24.5 cm length of metal braid sheathing were attached to each cable shield to prevent common mode currents and to minimize cable coupling with the transmit coil [137].

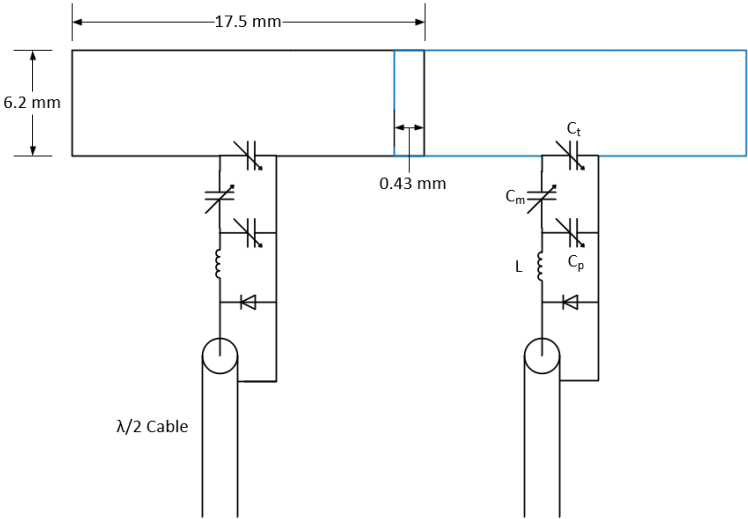


**Figure 15. Circuit diagram and physical dimensions of the receive array design.**



**Table 9. Component values and part numbers for circuit elements of the 32-element array.**

Component	Value	Part Numbers
$C_T$	18 pF + 1-5 pF	Passive Plus, 0505C180JP151X Johanson, 9702-1
$C_M$	1-5 pF	Johanson, 9702-1
$C_P$	18 pF (some elements required 20 pF)	Passive Plus, 1111C180JP152X (1111C200JP152X)
L	25 nH	Coil Craft, 0908SQ-25NGLC
Diode	N/A	MACOM, MA4P7470F-1072T

### III.3.2 Preamplifier Module Design

Modular boxes each containing a low noise preamplifier (WMA4R7A-R5, WanTcom) and associated circuitry for DC voltage protection and regulation were radially positioned within the box using acrylic formers. +10 VDC (0.6A) was supplied by an external power supply to the preamplifier module where it was distributed by a single fanout board to power each preamplifier box. A 100 mA bias signal for each of the active detuning networks was distributed from a fanout board containing a DC limiting resistor (36  $\Omega$ , Vishay) and an RF choke (1  $\mu$ H 1812CS, Coil Craft) on each line. Active detuning bias lines were connected to the coil and preamplifier input lines using a tee connector (Centric RF). The active detuning bias signal was provided by a PIN diode driver [138] that supplied a -5V forward bias and a +12V reverse bias signal to the receive elements during transmit and receive, respectively. A circuit diagram of the entire preamplifier module is shown in Figure 16. A mounted preamplifier board and associated components within a preamplifier box are shown in Figure 17 with the labeled components and their

associated part numbers shown in Table 10. The assembled preamplifier module is shown in Figure 18.

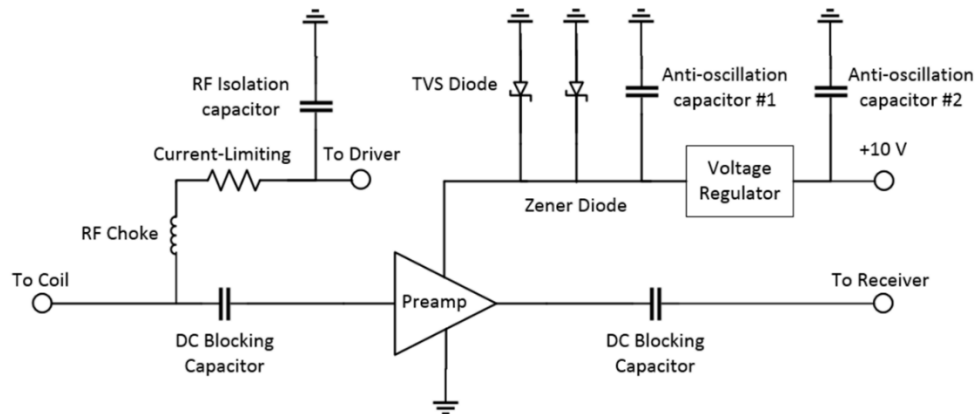


**Figure 16. Circuit diagram of the preamplifier module**

The active detuning and DC voltage regulation protection are also shown in the circuit diagram .

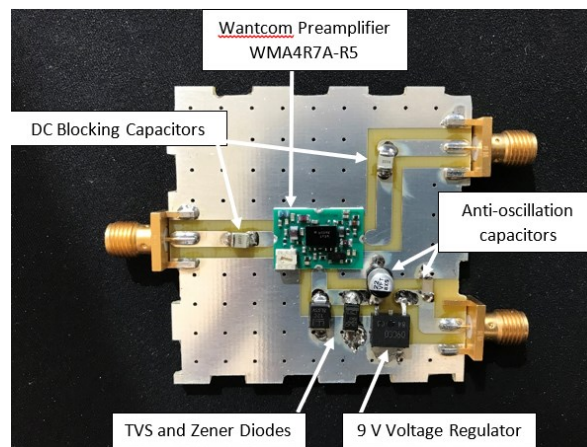


**Figure 17. Picture of preamplifier box with components mounted**

**Table 10. Component and part numbers for preamplifier module circuit diagram.**

Component	Part Number
Preamplifier	WanTcom, WMA4R7A-R5
DC Blocking Capacitors	Passive Plus, 1111C222JP101X
TVS Diode	Littelfuse, P6SMB12CA
Zener Diode	Vishay, BZG03C10-M3-08
9 V Voltage Regulator	ROHM Semiconductor, BA09CC0FP-E2
Anti-oscillation capacitor #1	Panasonic, EEE-FT1V220AR
Anti-oscillation capacitor #2	Vishay, VJ1206Y105KCXAT

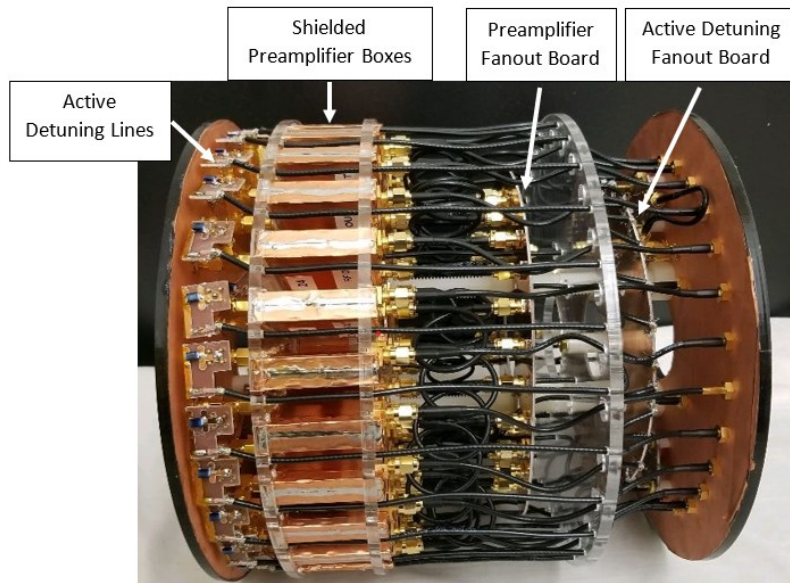


**Figure 18. Labeled and assembled preamplifier module**

### III.3.3 Magnet Flange Plate

To enable access into the bore for translation of the combined preamplifier module and coil system, a flange plate for the 40 cm, 4.7T magnet was designed (Figure 19). It consists of a double-sided copper FR4 board with 32 SMB-to-SMB connectors, 3 BNC-to-BNC connectors, copper mesh for RF isolation, 2 in copper pipe waveguide, and holes for attachment to the magnet. The copper pipe waveguide enables a rod attachment from

the preamplifier box to extend beyond the magnet for translation of the coil/preamplifier system. The three holes in the outer acrylic line up with the bolts that extend from the magnet bore, enabling tightening of the flange plate to the surface of the magnet with wing nuts.

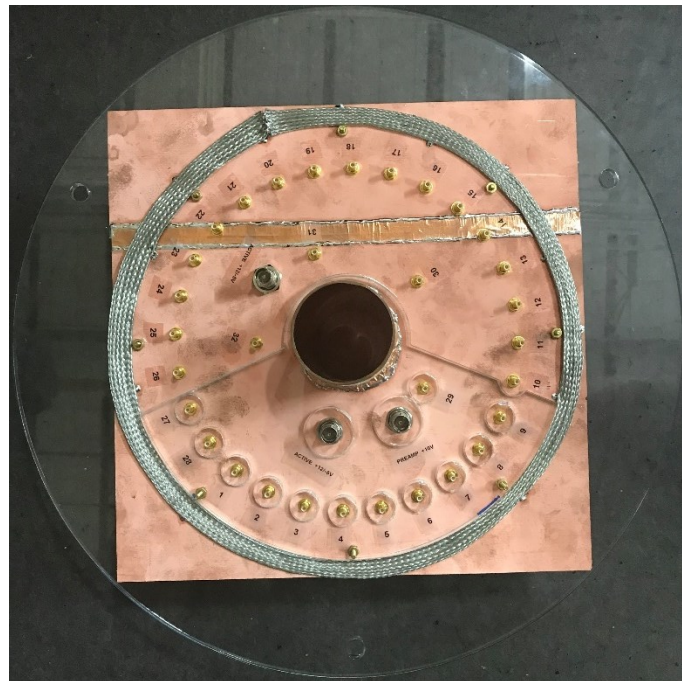


**Figure 19. Magnet flange plate for RF isolation and coil/preamplifier translation access (magnet-side shown).**

### **III.3.4 Preamplifier and Coil Benchtop Testing**

The gain of the individual preamplifiers was tested following integration of all 32 preamplifiers into the preamplifier module. Tests were performed using a HP 7970B noise figure meter calibrated to 200 MHz and utilized four averages per acquisition.

Benchtop measurements of  $S_{11}$ ,  $S_{21}$ , and  $Q$  measurements were obtained using an Agilent Technologies Network Analyzer (E5071C). Geometric decoupling of neighboring coils was adjusted under matched conditions using a canola oil phantom, which lightly loaded the coils. Active detuning and preamplifier decoupling levels were tested by lightly coupling a well-decoupled,  $S_{21}$  double-loop probe (loop OD = 1 cm) to each individual coil and testing under either  $50\Omega$  terminated conditions or connecting the coils to the preamplifier module for the respective detuning or decoupling bias. An iterative process of adjusting the active detuning with the  $C_p$  capacitor and trimming the  $\lambda/2$  cable to length to tune the preamplifier decoupling was performed while maintaining coil matching and tuning to  $50+j*0 \Omega$ . Coupling between the birdcage transmit coil and receive system was visually assessed by monitoring the  $S_{11}$   $Q$  of the birdcage while the receive system's position was adjusted within the birdcage coil [110]. A  $S_{21}$  depth sensitivity measurement was performed with an 8 mm (OD) probe and an isolated coil.

### **III.3.5 Experimental Setup and Sequence**

The experiment was performed using a 40 cm bore, 4.7T Varian Inova scanner. Utilizing a bandpass  $^1\text{H}$  birdcage as a T/R coil, the power calibration was performed on a cylindrical canola oil phantom (OD = 12 cm) to determine the requisite power to obtain a  $90^\circ$  tip angle. This value was utilized as a reference to determine the influence of the receive array and active detuning efficacy when present and detuned. Transverse and sagittal, T/R images were obtained with the birdcage with the receive array present and detuned using the scan parameters listed in Table 11. After validating the active detuning, the experiment was adjusted to use the birdcage as a transmit only coil and the 32-element

coils were utilized to receive. The 64-channel receiver system previously built by the MRSL was utilized for signal digitization [139]. The transverse and sagittal images were repeated with the changed configuration. Reconstruction of the array acquired data was performed using the sum of squares method [11].

**Table 11. Imaging parameters used to characterize performance of array.**

Slice Orientation	Transverse	Sagittal
Sequence	Ssems rxg	Ssems rxg
TR (ms)	1000	100
TE (ms)	30	30
FOV (mm)	150x150	200x200
Slice thickness (mm)	2	2
Matrix Size	256x256	256x256
Pulse duration ( $\mu$ s)	4000	4000
Pulse power (dB)	47/53	47/53

The preamplifier module and receive coil system were designed to be translated within the magnet bore. Modifications were made to push the associated transmit coil in conjunction with the receive system. The experimental setup and sequence are detailed below for the full translational experiment mimicking the 32x32 array:

1. Position the phantom bottle and its associated acrylic spacers within the volume transmit birdcage so that the bottle is concentric with the birdcage.
2. Place the birdcage within the magnet (56.2 cm from the magnet flange face (non-magnet room side) to the parallel face of birdcage).
3. Attach translation rod to movement control system and slide the preamplifier/coil system into the magnet until the ½” nylon rods extending from the receiver system

butt up against the face of the transmit coil (this will ensure that the translation during the experiment will only need to be directed into the magnet). The three triangular ramps located at the end of the acrylic piece nearest the coils will need to be positioned on the bottom and will help raise the receive system within the transmit birdcage coil during initial setup. The ½” nylon rods position the receive coils within the homogeneous region of the birdcage and where minimal adjustments are required for tuning of the birdcage. Figure 20 shows a top view of the system without the transmit coil present.

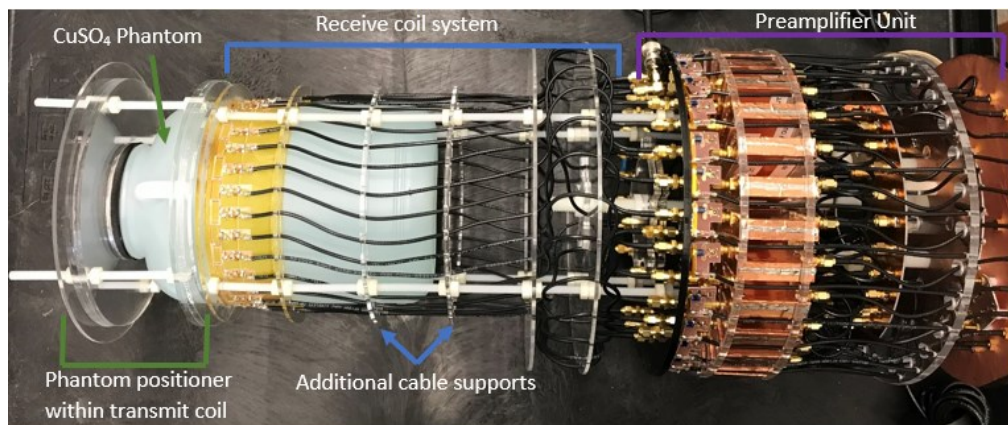


**Figure 20. Full configuration of the 32-element ring setup.**

Testing configuration for coil tuning, matching, active detuning, and preamplifier decoupling. The receive coil system is attached to the preamplifier unit to enable translation of the entire coil and preamplifier unit as a system. Note: bazoooka baluns and ½” nylon rods not shown here.

4. Slide the flange plate on the outside of the guiding/translation rod and then attach the cables to the flange plate connectors according to matching labels (1-32 → 1-

32, Active +12V/-5V → Active +12V/-5 V, Preamp +10V → Preamp +10V). The cables will be oriented as shown in Figure 21 for the two extremes of the translation experiment. The helix pattern ensures that the cables have enough overall length to traverse the required 15 cm translation and still compress for the starting state of the experiment. This ensures that the SMB connections will not undergo undue stress or tension. More importantly, this enables the experiment to be performed within the homogenous region of the magnet.

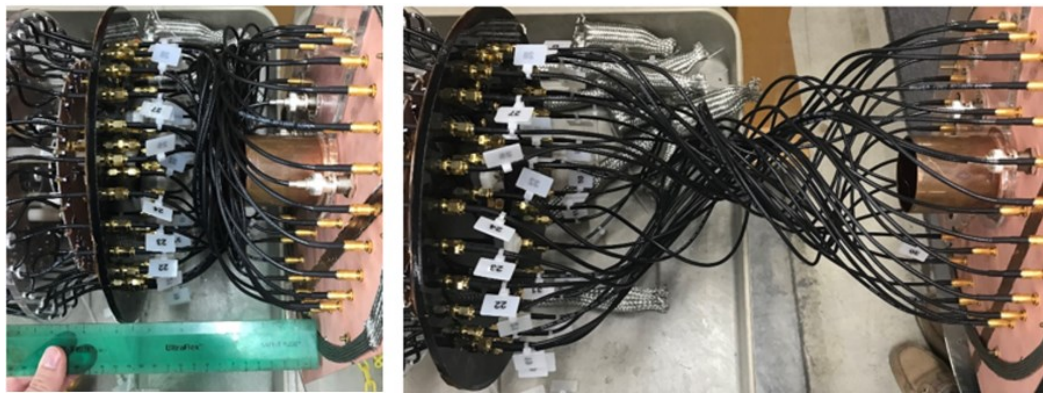


**Figure 21. Flange plate connections.**

(Left) Beginning experimental position with cables in the compressed state. (Right) Ending experimental positioning with preamplifier unit translated farthest into the magnet.

5. Fasten the flange plate to the magnet.
6. Connect SMB connectors on the outside of the flange plate to receiver system (Ch. 1-32), DC power supply (+10V to Preamp +10V BNC connection point – the power supply should read +10V for 0.65A), and PIN diode driver box (Output 1-16 → Active +12V/-5V, Output 17- 32 → Active +12V/-5V BNC connection



ports). Connections between the PIN diode driver box and the flange plate can be found in Figure 22. The controller switch of the PIN diode driver should be switched to “Dynamic” for TTL control (TTL = 5V for coil tuned state, TTL = 0 for coildetuned state). The PIN diode driver was designed to supply 1.6A per output channel with voltage states of +12/-5V.

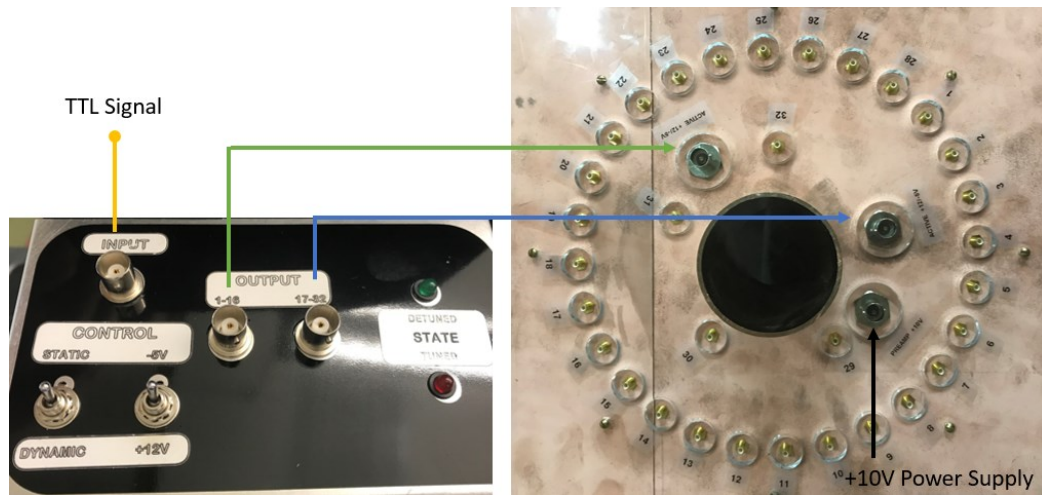


**Figure 22. PIN diode drive box and flange plate.**

(Left) Front view of the PIN diode driver box with input TTL port and two output ports labeled with connections. (Right) The outward facing view of the flange plate with its associated BNC ports and connections denoted.

7. Begin the 32-translation step experiment over the 14 cm z-directed homogeneous region of the magnet, where for each physical translation a set of images will be acquired from the 32-elements.

## **III.4 Results and Discussion**

### **III.4.1 Benchtop Measurements**

The results from testing the gain of the preamplifiers after integration of all 32 preamplifiers into the preamplifier module are shown in Table 12. The average gain and associated standard deviation amongst the preamplifiers were  $28.62 \pm 0.12$  dB. The WanTcom preamplifiers were rated for a noise figure of 0.40-0.50 dB.

**Table 12. Gain measurements for the 32 mounted and assembled preamplifiers.**

<b>Preamplifier</b>	<b>Gain (dB)</b>
1	28.45
2	28.8
3	28.7
4	28.7
5	28.8
6	28.7
7	28.7
8	28.8
9	28.8
10	28.4
11	28.7
12	28.6
13	28.6
14	28.7
15	28.6
16	28.4
17	28.6
18	28.6
19	28.5
20	28.6
21	28.7
22	28.6
23	28.6
24	28.6
25	28.5
26	28.6
27	28.7
28	28.3
29	28.6
30	28.6
31	28.6
32	28.6
Average	28.62
St. Dev	0.12

A summary of the important receive coil metrics is shown in Table 13. The raw data is represented in Table 14-16 The coils were well matched and tuned with a high

quality factor (Q) average of 100.4. The lowest Q was likely due to inductive coupling between the cables of coils 25 and 31, as the cable for coil 31 required spiraling within the outer ring of cables to accommodate the  $\lambda/2$  length of cable and the more rigid bazooka balun. Nearest and next-nearest neighbor coupling was sufficient for matching and tuning of the coils without the need for preamplifier decoupling of neighboring coils provided that this experimental setup was only a single ring of 32 elements. Additional rings of 32-elements would require preamplifier decoupling of surrounding coils to take  $S_{11}$  matching and tuning and  $S_{21}$  coupling measurements. An average of 21.4 dB of preamplifier decoupling and 26.2 dB of active detuning was achievable with the selected network and coil design.

**Table 13. Summary of average, standard deviation, and worst-case scenarios for  $S_{11}$ , loaded Q-factors, coupling measurements, decoupling, and active detuning.**

	$S_{11}$ (dB)	$Q_{\text{loaded}}$	Nearest Neighbor Coupling (dB)	Next-nearest Neighbor Coupling (dB)	Preamplifier Decoupling (dB)	Active Detuning (dB)
Average	-30.9	100.4	-21.5	-24.3	21.4	26.2
Standard Deviation	4.6	7.99	1.27	4.14	1.42	1.45
Worst- Case	-22.5	76	-18.9	-19.6	19.2	22.6

**Table 14. Raw data for the  $S_{11}$  and loaded Q-factors.**

<b>Coil Number</b>	<b><math>S_{11}</math> (dB)</b>	<b><math>Q_{\text{loaded}}</math></b>
1	-41.2	101.3
2	-33.1	100.6
3	-27	101.3
4	-22.5	108.2
5	-31.2	112.8
6	-24.4	97
7	-32.7	95.7
8	-29.3	104.3
9	-33.7	107.2
10	-30.3	109.4
11	-33.7	98
12	-28.4	107.6
13	-29.1	108.6
14	-38.1	109.1
15	-30.5	99.9
16	-34.5	103.3
17	-27.8	94
18	-32.4	98.4
19	-26.9	98.6
20	-30.1	92.2
21	-32.6	96.5
22	-34.8	99.7
23	-34.5	103.7
24	-23.2	101.3
25	-40.5	76
26	-26.1	96.3
27	-30.4	105
28	-39.4	102.7
29	-29.8	107.3
30	-31	104.5
31	-25.2	76.2
32	-26.5	97.5

**Table 15. Raw data for geometric decoupling of nearest and next nearest neighboring coils.**

<b>Nearest Neighbor Coupling</b>			<b>Next Nearest Neighbor Coupling</b>		
Coil 1	Coil 2	Coupling (dB)	Coil 1	Coil 2	Coupling (dB)
1	2	-21.9	1	3	-19.6
2	3	-20.5	2	4	-21
3	4	-21.1	3	5	-26.6
4	5	-22.7	4	6	-22.5
5	6	-19.6	5	7	-22.4
6	7	-20.2	6	29	-23.3
7	29	-22	7	8	-27.1
29	8	-19.8	29	9	-28.3
8	9	-22.9	8	10	-23
9	10	-21.9	9	11	-20.7
10	11	-20.4	10	12	-22.7
11	12	-22.3	11	13	-21.2
12	13	-22.3	12	14	-21.9
13	14	-20.9	13	30	-20.2
14	30	-23.4	14	15	-29.5
30	15	-20.9	30	16	-31.3
15	16	-22.3	15	17	-22.7
16	17	-20.6	16	18	-24.1
17	18	-23.3	17	19	-20.8
18	19	-20.7	18	20	-24.6
19	20	-19.8	19	21	-20.1
20	21	-22.8	20	31	-21.4
21	31	-20	21	22	-30.5
31	22	-22.6	31	23	-30
22	23	-22.5	22	24	-22.2
23	24	-23.1	23	25	-23.5
24	25	-23.4	24	26	-21
25	26	-21.2	25	27	-22.7
26	27	-20.7	26	28	-24.3
27	28	-19.9	27	32	-23.5
28	32	-22.6	28	1	-26.1
32	1	-18.9	32	2	-39.1

**Table 16. Raw data for preamplifier decoupling and active detuning**

<b>Coil Number</b>	<b>Valley Value (dB)</b>	<b>Peak Value (dB)</b>	<b>Preamplifier Decoupling (dB)</b>	<b>Active Detuning Valley (dB)</b>	<b>Active Detuning (dB)</b>
1	-53.8	-32.4	21.4	-57.1	24.7
2	-53.6	-33.1	20.5	-60.1	27
3	-57.5	-33.5	24	-60.9	27.4
4	-55	-33.7	21.3	-61.8	28.1
5	-54.4	-32.9	21.5	-58	25.1
6	-56.3	-33.2	23.1	-60.9	27.7
7	-53.2	-33.5	19.7	-59.5	26
8	-53.1	-33	20.1	-60.7	27.7
9	-54.3	-33.4	20.9	-59.1	25.7
10	-57.5	-33.3	24.2	-62	28.7
11	-54.7	-33.2	21.5	-59.4	26.2
12	-54.7	-32.9	21.8	-60.8	27.9
13	-54.8	-33.1	21.7	-58.9	25.8
14	-54.2	-33.1	21.1	-57.7	24.6
15	-56.8	-33.2	23.6	-58	24.8
16	-54.5	-33.2	21.3	-57.1	25.2
17	-53.1	-32.7	20.4	-58.6	24.4
18	-56.1	-33.3	22.8	-61.6	25.3
19	-57.4	-33	24.4	-60.3	28.6
20	-54.7	-33.2	21.5	-59	27.1
21	-52.3	-32.9	19.4	-59.5	26.1
22	-54.3	-32.9	21.4	-60.2	26.6
23	-54.2	-32.9	21.3	-60.1	27.3
24	-53.4	-33.4	20	-59.2	26.7
25	-53.9	-33.2	20.7	-55.7	26
26	-53	-33.1	19.9	-59.7	22.6
27	-55.8	-33.2	22.6	-57	26.5
28	-52.7	-33.5	19.2	-60	23.5
29	-54.8	-33.1	21.7	-58.5	26.9
30	-52.2	-32.9	19.3	-57.7	25.6
31	-53.1	-33.2	19.9	-60.6	24.5
32	-56	-33	23	-57.1	27.6

Initial testing of the active detuning, which was monitored by visual inspection of the Q of the birdcage, was complicated by the presence of severe coupling between the  $\lambda/2$  cables (without bazooka baluns) and the birdcage rungs. Baluns were added on the cables to create a high impedance on the cable shield at the  $^1\text{H}$  frequency. This enabled the translation of the array into the birdcage up to the point where the majority of balun entered the birdcage before substantial de-Qing was observed. Additionally, the tuning of the birdcage was influenced by the amount of copper added within the birdcage volume, as could be expected. To prevent the need for retuning of the birdcage for each translation step of the receive coil within the birdcage, the experimental design was shifted to physically translate both the receive and transmit coils as one unit around the stationary phantom. This better prevented the need for retuning and mitigated the chance of the receive array from de-Qing the birdcage differently on different physical translations. This was of utmost importance as the amount of power was desired to be similar for each of the 32 translation steps to best mimic the presence of 32 rings of 32 elements.

The  $S_{21}$  depth sensitivity profile, shown in Figure 23, shows the sensitivity profile of an isolated coil element. This reflects that the coil will be much more sensitive to signal sources within the first few centimeters and have limited sensitivity at greater depths.



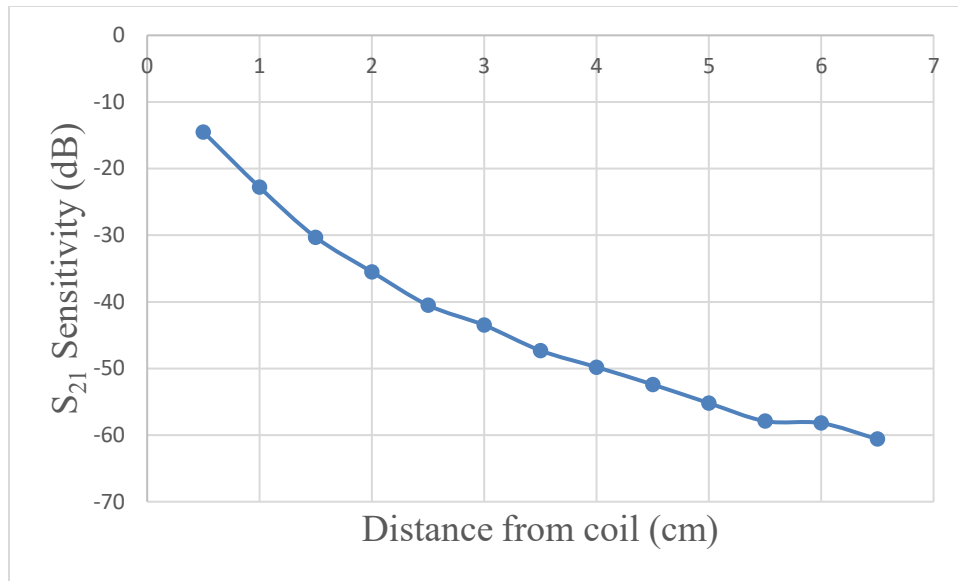


**Figure 23. Depth sensitivity map of an isolated test coil measured with a small pickup loop (OD = 8 mm).**

### III.4.2 Imaging Measurements

The initial power required to achieve a 90° tip with the birdcage was 100W, as measured by the power amplifier. With the presence of the detuned receive array with bazooka baluns on the cables, a 90° tip was still achievable but with 140W output from the power amplifier. Although there was an increase in power required, this can be attributed to the amount of copper and minor shielding that was introduced by the coils themselves and the match/tune networks. Initial testing with the detuned array present but without the bazooka baluns on the cables couldn't achieve a 90° tip. The birdcage T/R images, shown in Figure 24, show uniform homogeneous slices from the phantom. The lack of overtipping artifacts where the receive coils were present reveals that the active

detuning of the receive elements effectively detuned the coils during transmit and cable coupling was not an issue.

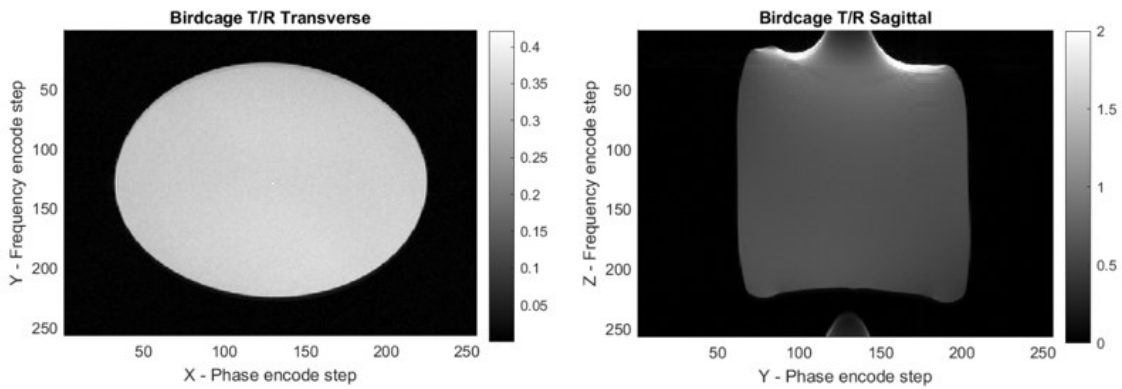


**Figure 24. Birdcage T/R images obtained with the receive array detuned.**

The transverse images from the receive coils are shown in Figure 25, and the sum of squares reconstructed image is shown in Figure 26. This shows that all channels were working and that the combined contribution from all the channels was able to resolve signal from the middle of the phantom. Being able to demonstrate depth sensitivity into the middle of the phantom was a major concern of the design due to the small size of the coils required based on Hutchinson and Raff's initial theory [136]. Therefore, this was a necessary result for further exploration of their theory.

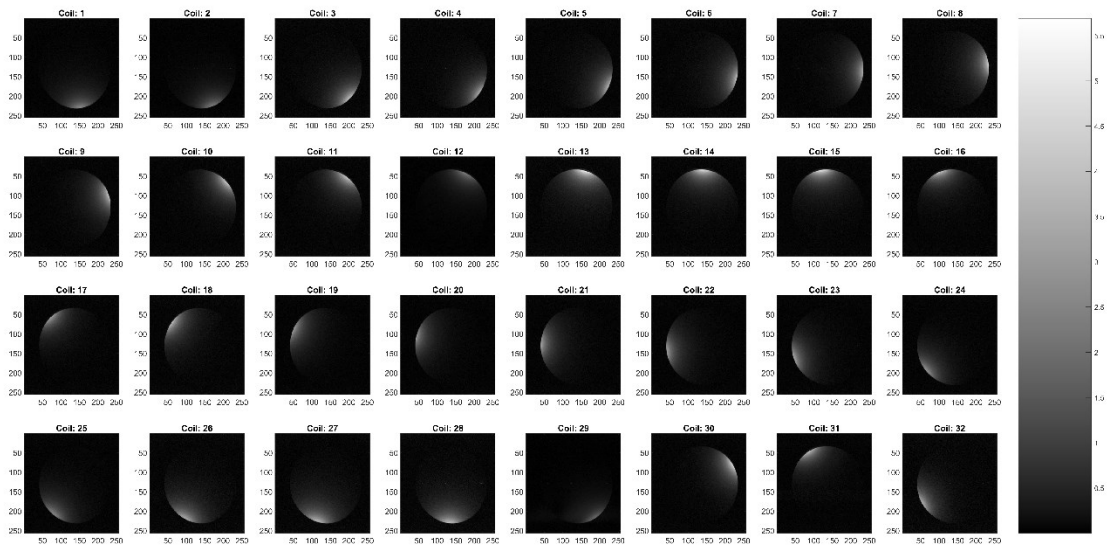


**Figure 25. Transverse images from all 32 array elements of a uniform canola oil phantom.**

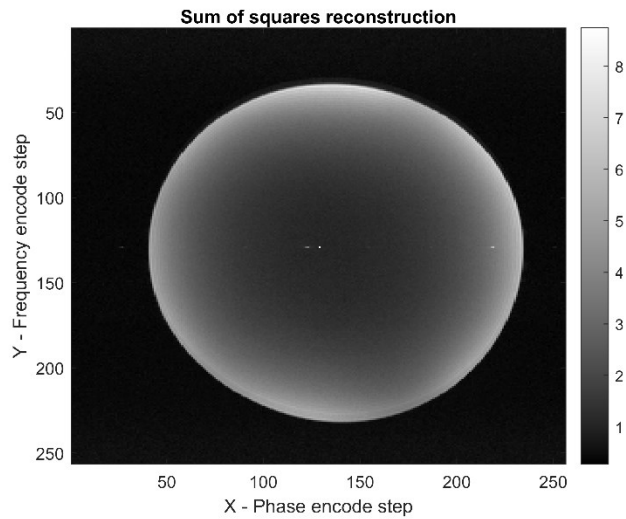


**Figure 26. Transverse slice, sum of squares reconstruction of a canola oil phantom.**

The sagittal images from the receive coils are shown in Figure 27, and the sum of squares reconstructed image is shown in Figure 28. It is peculiar that the receive coils, which only have a z-directed width of 6.2 mm would be able to resolve the entire length of the 18 cm long phantom. This indicates that transmit coil, which is actively detuned during receive, may require additional detuning on the lengths of the rungs rather than just on the end rings. Regardless, the highest intensity within the image was localized where the receive coils were present.

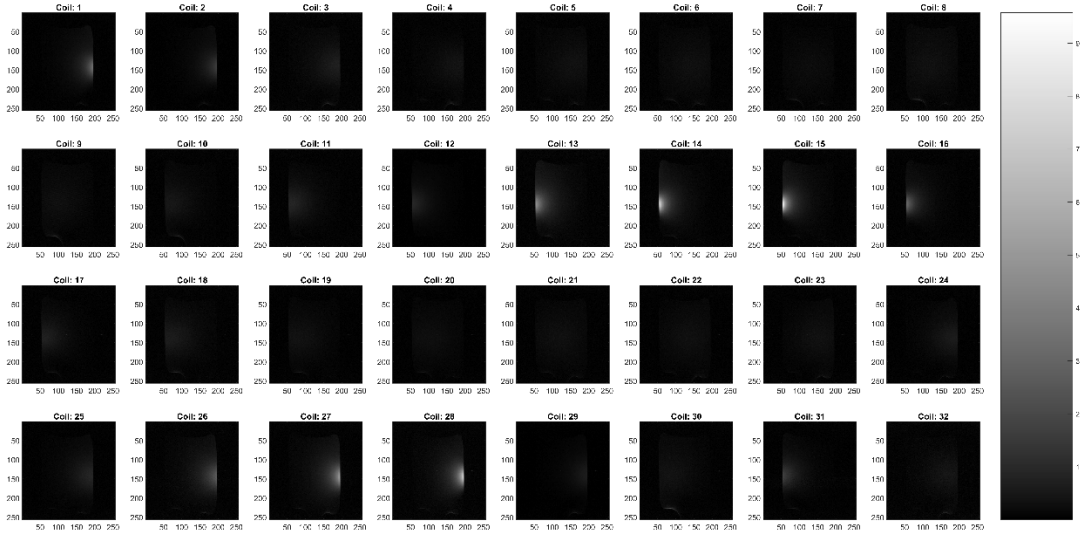


**Figure 27. Sagittal images from all array elements of a uniform canola oil phantom.**

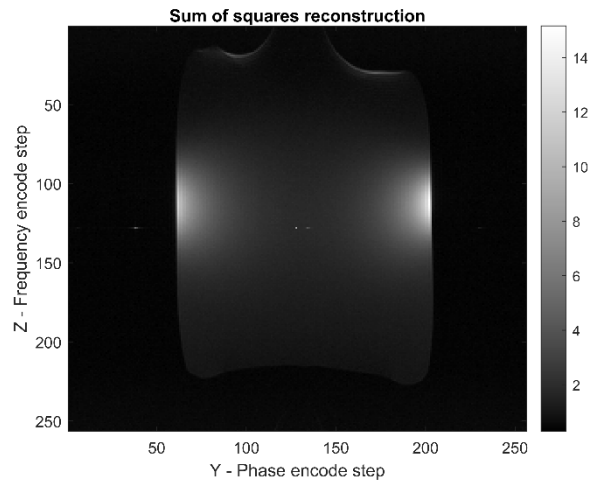


**Figure 28. Sagittal slice, sum of squares reconstruction of a canola oil phantom.**

### **III.5 Conclusion**

A custom 32-element ring array was developed with the associated preamplifier module for enabling translation experiments mimicking a 32x32 element array. Validation tests of the array system showed that active detuning and preamplifier decoupling were properly working, sensitivity at the middle of the phantom was obtainable, and that the system could be physically translated in the bore in conjunction with the transmit coil. Although sagittal images showed influence of the birdcage coil during receive, the performance of the single ring array for mimicking the 32x32 element array should not be impeded for transverse acquisitions. Changes to the detuning network of the birdcage coil, which were outside of the scope of this project, could be pursued for improved isolation for sagittal acquisitions. The simplified system provides a means for testing Hutchinson and Raff's theory for fast MRI with multiple receivers. Full implementation of the theory would revolutionize full body, MR image acquisition to where it could be implemented in

a matter of seconds rather than on the order of tens of minutes. Such a breakthrough would enable higher patient throughputs at clinics and expand the utility of MRI. Therefore, future work at the MRSL will include utilizing the experimental setup and equipment described in this chapter to acquire data for Hutchinson and Raff's theory validation.

CHAPTER IV  
MULTI-CHANNEL MAGNETIC RESONANCE SPECTROSCOPY GUI  
(MCMRSGUI)

**IV.1 Synopsis**

The use of radiofrequency coil arrays for magnetic resonance spectroscopy enables higher sensitivity over a larger field-of-view to be obtained. As the concentration of metabolites in the body can be quite low, the improved sensitivity is required to adequately distinguish the MRS signal from the noise. The proper combination of the array data without adding any unnecessary spectral distortion is important for quantification of *in vivo* metabolites. As open-source processing programs have mainly focused on the quantification of the already combined signal, this work details an open-source multi-channel MRS GUI for the combination of multi-channel MRS data using literature-based methods. As the different combination methods make different assumptions about the data and require different conditions or additional data in order to properly work, a decision tree was incorporated into the design of the code to aid researchers in determining the method that is best for their data. The incorporation of a spectral distortion simulation alongside the GUI enables the different combination techniques to be evaluated for the combined SNR at which distortions become prevalent. This can improve the quality of spectra and reduce distortions within results, which has implications for quantification accuracy.

## IV.2 Introduction

Magnetic resonance spectroscopy is a noninvasive method that provides access to important biochemical information from biological pathways and diseases in the body. Challenges associated with MRS of all nuclei involve detecting small concentrations, varying natural abundance and sensitivities of different nuclei relating to the overall obtainable signal intensity, and the balance between feasible scan times and appropriate localization.

One of the methods for alleviating some of these problems involves array coils and their increased sensitivity over a larger field of view. Roemer's seminal work described how an array of coils could be optimally combined with complex weighting factors for an improved result using the  $B_1^-$  receive fields and the noise covariance [140], but obtaining the requisite information required for the formulation isn't necessarily feasibly determined within a clinical setting. The "optimal" method for combining experimental spectroscopy data from multiple channels has been an active topic of discussion within literature [58, 59, 141], resulting in multiple combination technique options [54, 58, 59, 141-145]. Some of the techniques require either additional noise scans for obtaining noise correlation or covariance maps [58] or prior unsuppressed water reference scans [59, 141, 142], to obtain weighting factors. Others simply require the SNR or variations of subcomponents of the SNR with regards to a certain metabolite [57, 141, 146].

The tradeoff of using more scanner time for acquiring additional data and increasing the degree of post-processing results in either a better understanding of the noise correlation and covariance amongst the channels or an improved estimation of the



field maps of the channels through the increased sensitivity of  $^1\text{H}$  data. Regardless of the technique, the end goal of the combination is to improve the spectral SNR for reliability of quantification and fitting without introducing significant bias or spectral distortion. Spectral distortion directly results in inaccurate findings for quantification of metabolites. As the goal for spectroscopy processing is to minimize user interaction, spectral distortion can go unnoticed. Therefore, the selection of the combination technique should be determined based on the available additional clinical data, noise correlation between channels, degree of user interaction for phasing data, and the relative SNR of the combined spectra to ensure that the combined result is as accurate as possible.

MR vendors each have their own processing software, which often performs combination and some pre-processing operations on multi-channel data before allowing access to the “raw” data. Per a recent experts’ consensus report, it is recommended that individual transient data be accessible for preprocessing and RF coil combination, as well as effectively communicating all actions performed on the data to increase reproducibility of results [147].

Several groups have put forth open-source software to enable the processing of MRS data from the initial data loading all the way through data quantification [116, 148-151] or simply handle loading and preprocessing of data and transfer processed data to existing programs for quantification [152]. Variations exist among the programs as to the coding language, whether the source code is openly available (OSPNEY, OXSA, FSL-MRS, FID-A), or if they are packaged in a manner to make the program accessible amongst different computer architectures (jMRUI, INSPECTOR). Benefits arise from

both types of systems as modularity, visibility, and flexibility to add or modify code as newer methods become available is a key argument for making the source code available, while providing a packaged program can enable a more sequenced progression, platform-independence, and wider potential use. Regardless, both methods still require programming that is specific to a certain niche application and will require continued updates as newer processes become available. Therefore, open-source MRS code requires readability, low-entry to understanding, and transparency to be truly effective in an ever-changing field.

This work presents an additional alternative for processing of MRS data; presenting users with literature-based options to best combine and phase their multi-channel data in a format that can be presented as a standalone program or be accessible via a coding language commonly used by those in the field. Although it was designed specifically for use with single voxel, x-nuclei data, it also incorporates methods that can be utilized for  $^1\text{H}$  spectra.

### **IV.3 Methods**

The McMRSGUI was developed in MATLAB (Mathworks, Natick, MA) using App Designer to allow the graphical user interface (GUI) to be published in a stand-alone capacity or be used within MATLAB's coding environment for research use. This platform enables flexibility as the template code can be adjusted to specific research needs and then be compiled and shared with fellow researchers. The compiled GUI can be run on any computer that has the MATLAB Runtime environment installed, which is free and available for download from the MathWorks website [153].

### IV.3.1 Data Loading

The program is configured to load time domain spectroscopy data within three file types: Varian (.fid), jMRUI Data Textfile (.txt), or a MATLAB structure (.mat). Time domain data must represent baseband or digitally demodulated spectroscopy data. Necessary information for loaded files includes the complex FID data, center frequency, and spectral bandwidth. Multiple files or acquisition sets can be loaded at once and will be treated as if they are a continuation of the previously loaded file(s) acquisitions.

Two matrix structures can be loaded within the program for MATLAB file types: structure “Starting” for the starting structure and structure “Processed” for data previously processed with the program. The structure “Starting” must have fields labeled: “Filename” of the character data type of the filename, “Data” for the complex time domain FIDs in the format of a double matrix ( $N\_channels \times N\_acquisitions \times N\_datapts$ ), “F0” for the double representing the center frequency in hertz, and “BW” for the double representing the bandwidth in hertz. The structure, “Processed,” stores a single processed channel with information regarding the spectra: 0-order and 1<sup>st</sup>-order phasing, number of sliding window averages selected, line broadening (Hz), zero-padding factor, baseline correction selection, linewidth (Hz), SNR, time domain data ( $N\_acquisitions \times N\_datapts$ ), spectral data ( $N\_acquisitions \times N\_datapts$ ), frequency axis (MHz), center frequency (MHz), bandwidth (Hz), noise region selection limits (MHz), real noise (standard deviation within noise region selection limits), peak maximum intensity, peak location (MHz), acquisition file names, source file names, and channel selection. Data that is processed and exported from the program will be stored in the “Processed” structure format.

### **IV.3.2 Preprocessing**

Functionality for preprocessing of individual channel data, such as averaging transients with a sliding window average of user-defined length, automatic or manual 0-order and 1<sup>st</sup>-order phasing [154], baseline correction [155], zero-padding, subtraction of another file for removal of the water peak or broad baseline macromolecules, and different viewing configurations either in the time domain or frequency domain, are built into the program. Additionally, line broadening is included for data viewing but is not recommended for data quantification. Inspection of the data for data quality can be performed through viewing the FID, noise-normalized spectra, or a waterfall plot. Spectral evaluation of linewidth and SNR are performed using the maximum peak or on a user-defined frequency region. Noise selection limits and frequency axis viewing limits are manually set by the user. Fully preprocessed data can be exported in two different formats: either in the .mat structure “Processed” or in the jMRUI Data Textfile format. Both formats can be reloaded and preprocessed as necessary.

### **IV.3.3 Multi-channel Combination**

The preprocessed multi-channel data is combined in the spectral domain by multiplying each channel by a weighting factor before summation with the other weighted channel data. Selection of the combination method can be chosen directly by the user or the decision tree matrix, shown in Figure 29, will assist the user in selecting an appropriate method. Six weighting options are available within the program: equal weighting, SNR-weighting [54, 57], S/N<sup>2</sup>-weighting [141], whitened value singular-value decomposition (WSVD) with or without apodization [58, 156], and adaptively optimized combination

(AOC) [59]. The first three methods assume that the noise between channels is not correlated. Phasing of the spectra is necessary to adequately estimate the signal and noise components for the first two methods, while the  $S/N^2$  method utilizes complex weighting factors obtained from the fitting of a reference peak within the data. Additionally, the alignment of peak frequencies is an option afforded to the user to correct for frequency shifts amongst the channels due to positioning of the array for the equal and SNR weighing methods. The WSVD method requires the calculation of a noise covariance matrix obtained from a user-defined noise free region in the spectral domain or a separate noise scan obtained with the transmitter turned off. In scenarios where the SNR of the data is low, utilizing the WSVD+Apod method can improve the estimation of the weighting factors through the application of linebroadening or apodization. The quality of the estimate of the WSVD weighting factors displays in a range from 0 to 1, with 1 representing the highest quality estimation. The AOC method incorporates an unsuppressed water scan into the weighting factors and the inversion of the full noise correlation matrix. The full noise correlation matrix incorporates the coil covariances onto the diagonal components of the noise correlation, enabling this method to better estimate the influences from intrinsic and extrinsic noise sources. Like the WSVD method, the

quality of the full noise correlation is determined by the number of data points used to calculate the correlation matrix.

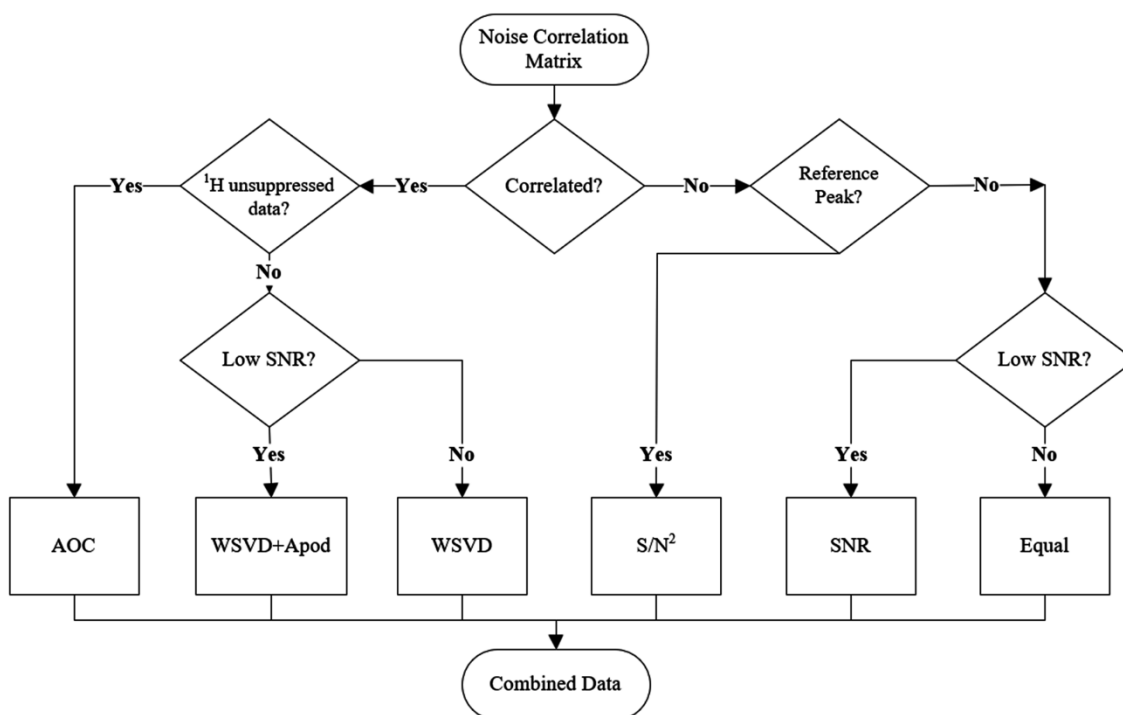


**Figure 29. Combination method decision tree.**

Multi-channel spectroscopy combination method decision tree logic utilized within the McMRS GUI. The user has the option to specifically select a method or use the program as a guide for selecting an appropriate combination method. Utilization of supplemental <sup>1</sup>H unsuppressed water data for determining weighting factors improves the accuracy of the combination method(s) in scenarios of low SNR combination. The weighting methods are arranged from left to right in order of literature-recommended order for the scenario of correlation between channels.

To validate the McMRS GUI processing code, two Lorentzian resonance peaks were modeled according to the simulation by Wu et al. for measuring distortion introduced

by multi-channel combination techniques [59]. The Lorentzian peaks were modeled according to Eq. IV.1

$$x(p) = \sum_{q=1}^2 a_q e^{j\theta_q} e^{(-d_q + j2\pi f_q) \frac{p}{f_s}} \quad \text{Eq. IV.1}$$

where  $f_s$  is the sampling frequency, and  $a_q$ ,  $\theta_q$ ,  $d_q$ , and  $f_q$  denote the amplitude, phase, damping factor, and resonance frequency of the  $q$ th sinusoid, respectively. Parameters used for the simulation and the associated scaling of the eight generated coils elements are in Table 17. Distortion was measured as the difference between the ratio of the areas underneath the two peaks from the original model spectrum and the combined spectrum. jMRUI and the AMARES algorithm were utilized for calculating the areas under both peaks following data combination [29, 116].

**Table 17. Parameters for simulation of two Lorentzian peaks and coil element scaling factors.**

Peak q	$a_q$	$\Theta_q/\text{rad}$	$d_q$	$f_q/\text{Hz}$			
1 (creatine, CH <sub>3</sub> )	15	0	10	132			
2 (creatine, CH <sub>2</sub> )	15	0	10	56			
Coil Element Scaling Factors							
1	0.8	0.7	0.6	0.5	0.65	0.9	0.93

For the simulation, the noise content was varied between levels corresponding to high SNRs and low SNRs, where the SNR was defined as the signal amplitude of the

highest peak over the standard deviation of the noise after the application of a matched filter [157]. The noise region was selected as the last 400 points of the simulated spectra where there were no peaks. As each combination method produced a different SNR for the same added noise level, the noise level was used as the common variable to compare the overall distortion level between the methods. Monte Carlo simulations were utilized to generate 300 variations of the eight-element noise data for each noise level utilizing Matlab's white gaussian noise function with a 50 Ohm impedance. The results of the Monte Carlo simulations enabled the comparison of the mean and standard deviation for each noise level and associated combination method. The assumption that the AOC method could adequately determine the coil sensitivities and spatial phase shifts of the individual coil elements from an unsuppressed water resonance was utilized, as per Wu et al.'s simulation [59]. The  $S/N^2$  method's signal amplitude factors were calculated using the AMARES algorithm in jMRUI [29, 116].

#### **IV.4 Results**

The fully constructed Matlab GUI for the McMRSGUI is shown in Figure 30. The WSVD+Apod combined data of the simulated data case with 37.5 dB of noise added is shown as an example to illustrate the functionality of some of the preprocessing and spectral evaluation tools. Further examples of the functionality and utilization of the program can be found in the Appendix B.



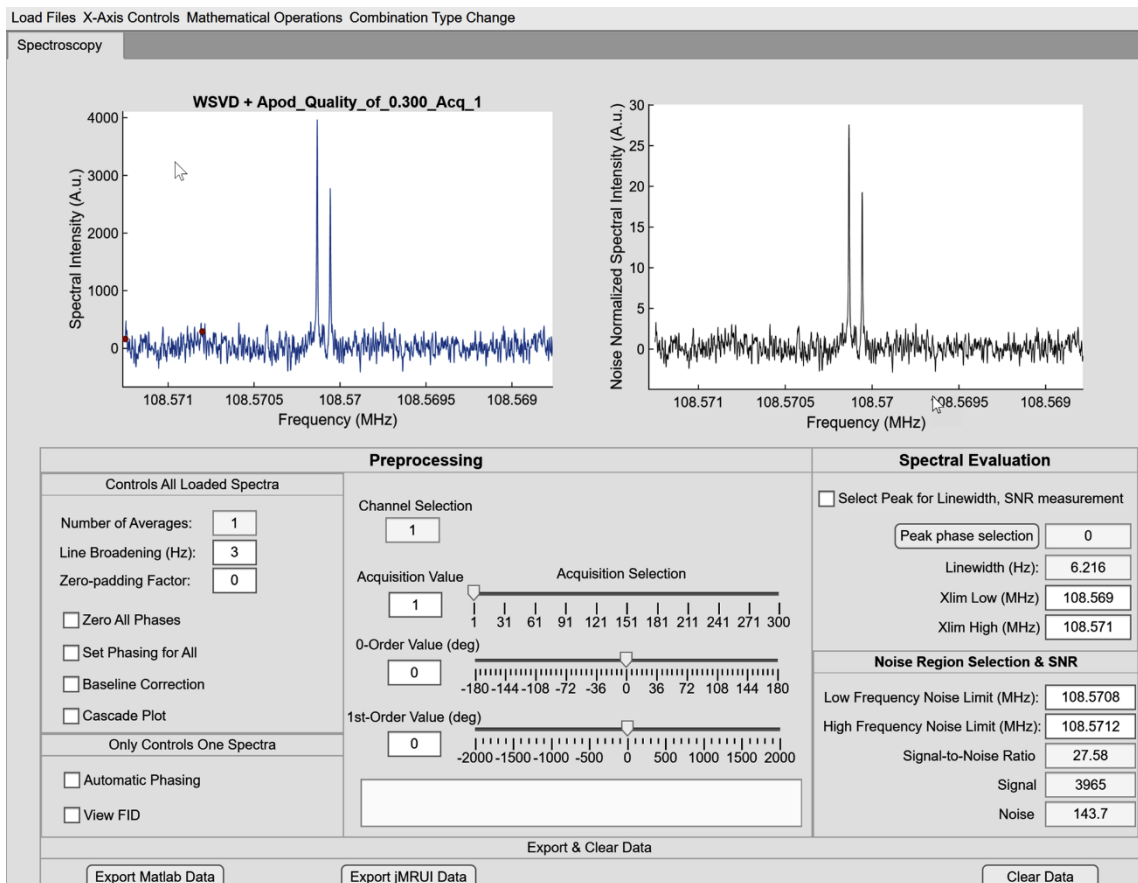


**Figure 30. McMRSGUI front panel.**

McMRSGUI front panel showing the first acquisition of the WSVD+Apod combined spectra from the simulated dataset with 37.5 dB of noise added. The preprocessing controls are shown in the leftmost tab group and the spectral evaluation tools are shown on the right. The quality of the WSVD+Apod fitting is shown with the title above the spectrum.

Figure 31 and Figure 32 show the mean and standard deviation of the combined spectrum's ratio of the area of the two peaks from that of the original model spectrum following Monte Carlo simulations at different noise levels. The corresponding mean SNR of each method is shown in Figure 33. At lower added noise levels, corresponding to higher SNR levels, all the methods combine the spectrum with little to no mean distortion.

Increasing levels of distortion occur as higher levels of noise are added, making the signal more difficult to distinguish from the noise. The WSVD+Apod method outperforms the original WSVD method at lower SNR levels due to its reduction in high frequency noise from linebroadening when estimating the weighting factors. Overall, the AOC method had the lowest or one of the lower levels of distortion for the tested noise ranges. All of the above results represent a similar performance to the simulation completed by Wu et al. [59], validating that the combination methods are accurately implemented. Due to the simulation being run with no phase distortion on the channels, this represented the best-case scenario and mitigated the requirement to manually phase the spectra for the equal and SNR methods. This resulted in an improved performance for these methods at lower SNR values than would normally be expected, as these methods rely on manual phasing before the calculation of the scalar weights.

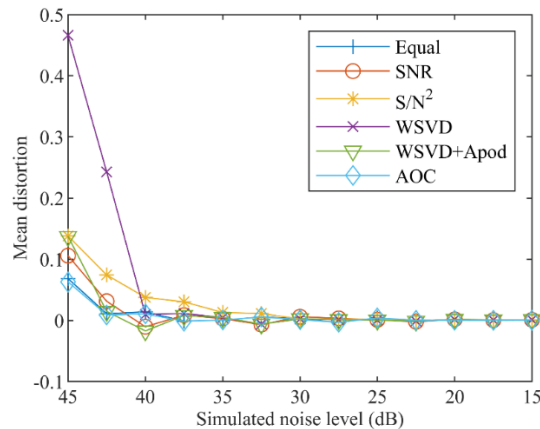


**Figure 31. Mean distortion as a function of simulated noise.**

The mean distortion of the combined spectrums' peaks ratio resulting from the Monte Carlo simulation. Due to the signal content remaining constant and the associated SNR of the combined spectrum varying due to the different combination methods, the mean distortion is shown as a function of the simulated noise level.

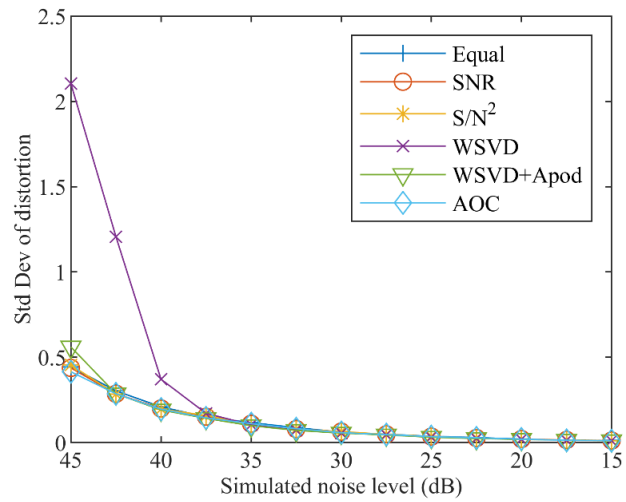


**Figure 32. The standard deviation of the distortion as function of the simulated noise level.**

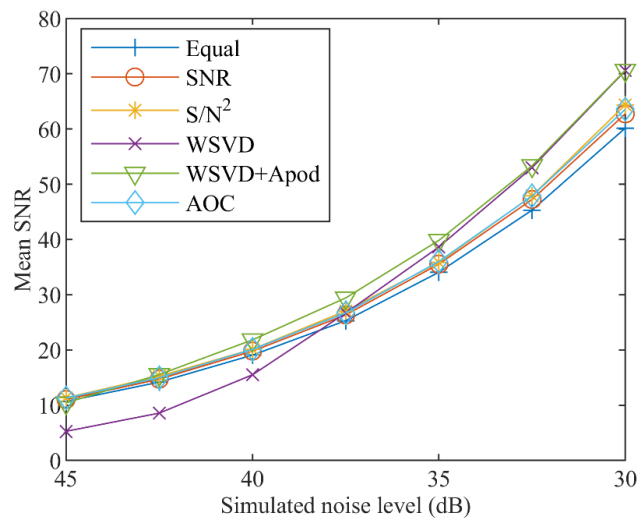


**Figure 33. The mean SNR as a function of simulated noise**

The SNR of each combination derived from the highest peak's amplitude over the standard deviation of the noise in the range of the highest simulated noise levels. A matched filter was applied before the SNR calculate was taken.

## IV.5 Discussion

For multi-channel MRS data, the selection of the combination type has implications for the quality and relative distortion from the absolute spectra that is obtainable. As the absolute result cannot be adequately inferred from the limited information obtained within a clinical setting, the best estimation represents the highest achievable standard for MRS combination. The estimations for all the combination methods converge to a similar result for cases where the SNR is adequately high. As high SNR is rarely the case for clinical spectroscopy due to the need for localization, limited scan times, physiological concentrations, and decreased sensitivity for x-nuclei, the selection choice for the combination of multi-channel data becomes weightier. The methods that utilize an unsuppressed water scan benefit from the much higher sensitivity within the body for determining phases and scaling factors. As x-nuclei studies do not have the luxury of the higher sensitivity from water, a prominent metabolite, such as PCr for  $^{31}\text{P}$ , can be used. Solely utilizing the water content or prominent metabolite for determining the scaling coefficients disregards the influence of the noise correlation between channels. Ideally, the receive array being used would have little to no correlation between channels due to good design, sufficient decoupling from preamplifiers, and no development of eddy current signals from the patient or surrounding MR components. In this case, the noise correlation matrix could be disregarded and one of the SNR-based methods could be used. With the advent and use of higher channel count arrays, correlation between channels will undoubtedly increase. Therefore, an understanding of the noise correlation should be factored into the selection for combination method.

In their work, Rodgers et al. provided an SNR guideline of 35, 15, and 60 at which the WSVD, WSVD+Apod, and  $S/N^2$  methods, respectively, began to produce higher SNR values than what Rodgers et al. called Roemer's (BS B<sub>1</sub>) combination [58]. To verify the validity of this threshold, a 3 Hz matched filter was applied to the output of the combined spectra and found that the WSVD, WSVD+Apod, and  $S/N^2$  methods produce similar SNR values to those reported by Rodgers et al. at simulated noise levels of ~35 dBm, ~42.5 dBm and ~30 dBm, respectively. These simulated noise levels were all above the point at which the combination methods began to introduce distortions into the combined spectrum in Figure 31, thus supporting the conclusion by Rodgers et al.

An extension of the above validation can be applied by researchers to their in vivo data sets by utilizing the same simulation performed in this work. The full noise correlation matrix and approximate coil amplitudes from the in vivo data can be inputted into the simulation for spectral distortion proposed by Wu et al [59]. The addition of noise levels, as performed in this paper, can then be run through Monte Carlo simulations to verify when the ratio of peak areas of the combined spectrum departs from the absolute ratio, providing validation for the SNR at which the clinical data were combined with regards to distortion and the combination selection. This can provide researchers a method to mitigate distortion in their data as well as increase the SNR and associated confidence in the fitting of the metabolites within their data.

#### **IV.6 Conclusion**

The McMRSGUI consolidates literature-based, multi-channel combination techniques within a single, flexible GUI for utilization in determining the proper technique

based on the available additional scan information, noise correlation between channels, and combined SNR. The decision tree provides a simplified approach for the selection of the various techniques. Data can then be exported for quantification with other open-source software. The software was validated using a spectral peak distortion simulation that both verified SNR values presented by Rodgers et al [58] and provides insight into the point at which distortion is likely to be introduced due to the combination method. This can be utilized by researchers to reduce the likelihood that the chosen combination technique will introduce distortion.

#### **IV.7 Notes**

The open-source GUI and scripts utilized for data simulation are openly available at: GitHub at <https://zenodo.org/badge/latestdoi/466353310>, along with the McMRSGUI manual.

## CHAPTER V

### CONCLUSION AND FUTURE WORK

#### V.1 Contributions to the Field

The compilation of projects addressed in this work were targeted at several facets of the issue of accessibility within MRI/MRS. The first facet involved addressing a need to both demonstrate and deliver hardware for conducting x-nuclei studies with a low-cost scanner. The coils, protocol, post-processing software, and associated hardware for foot flexion exercises were developed specifically for the 1.0T,  $^{31}\text{P}$  study. This represented an area where clinical scanners did not provide services beyond the standard  $^1\text{H}$  imaging capabilities. Retrofitting the scanner with these capabilities allowed for us to assess the feasibility of dynamic  $^{31}\text{P}$  for metabolic studies with a 1.0T extremity scanner. Extending capabilities of this type of magnet beyond  $^1\text{H}$  imaging would allow additional utility and convenience to the method. The smaller size allows for this technology to be accessible in a small clinic and is less intimidating to patients with fears of being in a cramped bore.

The second facet concerned the evaluation of coil designs and hardware for increasing the sensitivity and access to different x-nuclei. To eliminate the need to move patients between coil matching/tuning, as well as providing the ability to co-register  $^1\text{H}$  information, a three-element, tripled-tuned receive array was developed. This has the potential for benefiting clinical evaluation for x-nuclei studies. This particular design mitigated the need for preamplifier decoupling between receive elements and enabled switchable matching and tuning to frequencies spanning the range of common clinical

nuclei. Although the individual Q for each element were degraded below that of a single tuned coil, the switchable, triple-tuned phased array attempted to rectify these losses through the combined sensitivity improvement from the array while maintaining the ability to change between three separate frequencies.

In addition to the triple-tuned array, the work evaluating the Pentek® broadband receiver presented another hardware solution for improving accessibility for multi-nuclear studies. Limitations in the number of x-nuclei receiver channels prevents novel coil designs from ever being built, which is especially hindering for nuclei that require additional coils to improve detection sensitivity. Evaluation of the Pentek® card ensured that comparable SNR's could be had with it as compared to its predecessor. The additional functionality and possibility of receiving with 32 different channels for non-<sup>1</sup>H nuclei greatly improves capabilities for single and multi-nuclei studies with high channel count. Although having no bearing on the sensitivity, the increased capabilities of this card enables evaluation of decimated data file sizes for multi-channel, multi-acquisition studies without overwhelming the MR console computer.

The final hardware solution that was accomplished in this work involved the development and evaluation of the 32-channel ring array. The potential to verify the theory posited by Hutchinson and Raff for whole body imaging in a matter of seconds has large implications for accessibility and the entire MRI field. The ability to keep a patient in the scanner for a matter of seconds rather than several 10s of minutes for a whole-body scan would drastically improve the ability to increase patient throughput in clinical settings. Although the presented hardware was not the full realization of Hutchinson's design, it



was a novel design for mimicking the full realization of the 32-ring by 32-elements array. It represents a step forward in the field of MRI for the ultimate goal of realizing fast MRI, thus enabling the potential for higher throughput of patients.

The software approach was geared toward increasing the usability of multi-channel combination techniques for multi-channel MR spectroscopy. Several literature-based methods exist for combining MR spectroscopy, but they each have their own strengths and assumptions. While this algorithm relies on previously reported combination techniques, it aims at helping users to select an appropriate combination method for their application while minimizing spectral distortion in their data. Guidelines can be developed for which combined SNR values that the respective combination methods begin to introduce additional distortion. The posting of this code as an open-source GUI is aimed at increasing reliability of MR spectroscopy and providing researchers a tool to best combine their data before quantification.

This work has expanded the capabilities of existing scanner technologies through multi-nuclear coil and hardware design/evaluation, along with the development of specialized software to improve accessibility to MRI and MRS.

## **V.2 Future Work**

As the nature of research is ongoing, there are still areas to be further pursued from the aforementioned projects. One of the largest areas that had potential for clinical relevance was the evaluation of a COPD cohort using the system retrofitted to the 1T ONI magnet. We had just begun patient trials and were unable to continue evaluating patients due to the unfortunate quenching of the 1T magnet. Evaluation of both healthy and COPD

cohorts would have given the utility of the method more significance in our evaluation. Provided that the magnet could be brought back online, the incorporation of the new digitizer card with the broadband system would enable shorter repetition times resulting in higher SNR per unit time. Further reworking of the receive array to become more patient noise-dominated in addition to the higher channel capabilities of the digitizer card could prove useful in either better targeting of the gastrocnemius region through additional  $^{31}\text{P}$  coils or providing the potential for a dual-nuclei evaluation provided the transmit coil was double-tuned as well.

For the three-element, triple-tuned array project, evaluation into a different matching mechanism to reduce loss in the matching network could prove fruitful. As the realized gain was roughly equivalent of a single coil based on the Q, we gained a larger field of view and the ability to have a three-element, triple-tuned array and not the sensitivity enhancement from surface coils. The exploration into a design of a triple-tuned volume coil could have utility as there are very few, if any, published papers about this topic for volume coils. Integration of a multi-tuned, multi-element array with the accompanying multi-tuned volume coil could provide the potential for multi-nuclear, interleaved studies. The current switching design incorporating PIN diodes prevents us from obtaining simultaneous multi-nuclear data. The limiting factor would be the speed of the PIN diode driver and the duration of the signal decay for each respective nuclei.

Future work surrounding the 32-element ring array could involve improving the detuning of the accompanying birdcage coil or developing an alternative volume coil with better isolation during receive. Isolation between the birdcage and the ring array during

power transmission was adequate for achieving a 90° tip with only a slight increase in the overall power requirement, but the ability to isolate signal from the opposite side of the bottle indicated that signal was coupling through the birdcage rungs during reception. Removal of this signal would render the full 32-step experiment as a better representation of Hutchinson et al.'s original theory. Cable management was a challenge for this design given the constraint of the 40 cm bore size. As the preamplifiers were mounted in a box instead of directly on the coil, this accounted for some additional copper close to the MR experiment. If given a larger bore, the preamplifiers could be mounted directly above the coils and the cables bundled and ran outside of the bore as a unit with some floating baluns and grounding shields. Full realization of the 32-ring x 32-element array will need to find an appropriate solution for sheer volume of cables coming from the bore, potentially through miniaturized fiber-optic transmission systems.

The final area for future work involves further improving the McMRSGUI. Areas for improvement involve adding additional loading capabilities from clinical scanners. This would improve usage of the program as it is currently limited to the Varian format, Matlab structures, and jMRUI Textfiles. The code could also be modified to load in data from the new broadband receiver card to streamline spectroscopy analysis for the multi-channel capabilities that are being developed around the broadband system at MRSL. As the broadband system doesn't have a dedicated processing environment, the GUI could be extended to imaging applications, QA scan protocols, etc.

## REFERENCES

- [1] G. E. Uhlenbeck and S. Goudsmit, "Spinning electrons and the structure of spectra," (in English), *Nature*, vol. 117, no. 2938, pp. 264-265, Jan-Jun 1926, doi: DOI 10.1038/117264a0.
- [2] J. W. Verhoeven, "Glossary of terms used in photochemistry (IUPAC Recommendations 1996)," *Pure and Applied Chemistry*, vol. 68, no. 12, pp. 2223-2286, 1996, doi: doi:10.1351/pac199668122223.
- [3] J. Larmor, "LXIII. On the theory of the magnetic influence on spectra; and on the radiation from moving ions," *The London, Edinburgh, and Dublin Philosophical Magazine and Journal of Science*, vol. 44, no. 271, pp. 503-512, 1897/12/01 1897, doi: 10.1080/14786449708621095.
- [4] P. Zeeman, "The Effect of Magnetisation on the Nature of Light Emitted By a Substance," *Nature*, pp. 347-347, 1897, doi: 10.1080/14786449708620985.
- [5] G. K. von Schulthess, "The Physical Basis of Magnetic Resonance Imaging," in *Morphology and Function in MRI: Cardiovascular and Renal Systems*, G. K. von Schulthess Ed. Berlin, Heidelberg: Springer Berlin Heidelberg, 1989, pp. 3-32.
- [6] F. Bloch, "Nuclear induction," vol. 70, ed, 1946, pp. 460-474.
- [7] Department of Chemistry Instrumentation Facility. MIT. "NMR Frequency Table." <https://chemistry.mit.edu/wp-content/uploads/2018/08/NMR-Frequency-Table.pdf> (accessed 10/28, 2021).
- [8] F. Bloch, "The Principle of Nuclear Induction," *Science*, vol. 118, no. 3068, pp. 425-30, Oct 16 1953, doi: 10.1126/science.118.3068.425.
- [9] E. A. Barberi, J. S. Gati, B. K. Rutt, and R. S. Menon, "A transmit-only/receive-only (TORO) RF system for high-field MRI/MRS applications," *Magn Reson Med*, vol. 43, no. 2, pp. 284-9, Feb 2000, doi: 10.1002/(sici)1522-2594(200002)43:2<284::aid-mrm16>3.0.co;2-c.
- [10] J. J. H. Ackerman, T. H. Grove, G. G. Wong, D. G. Gadian, and G. K. Radda, "31P NMR using surface coils," *Nature*, vol. 283, no. January, pp. 2-5, 1980.
- [11] P. B. Roemer, W. A. Edelstein, C. E. Hayes, S. P. Souza, and M. Mueller, "The NMR Phased Array," *Magnetic Resonance in Medicine*, no. 16, pp. 192-225, 1990.

- [12] C. E. Hayes and P. B. Roemer, "Noise correlations in data simultaneously acquired from multiple surface coil arrays," *Magn Reson Med*, vol. 16, no. 2, pp. 181-91, Nov 1990, doi: 10.1002/mrm.1910160202.
- [13] M. A. Griswold, "Characterization of Multichannel Coil Arrays on the Benchtop," in *RF Coils for MRI*, J. T. Vaughan and J. R. Griffiths Eds.: Wiley, 2012.
- [14] A. Reykowski, S. M. Wright, and J. R. Porter, "Design of matching networks for low noise preamplifiers," *Magn Reson Med*, vol. 33, no. 6, pp. 848-52, Jun 1995, doi: 10.1002/mrm.1910330617.
- [15] M. Wilcox, S. M. Wright, and M. McDougall, "A Review of Non-1H RF Receive Arrays in Magnetic Resonance Imaging and Spectroscopy," *IEEE Open Journal of Engineering in Medicine and Biology*, vol. 1, pp. 290-300, 2020, doi: 10.1109/ojemb.2020.3030531.
- [16] J. Mispelter, M. Lupu, and A. Briguet, *NMR Probeheads for Biophysical and Biomedical Experiments*. IMPERIAL COLLEGE PRESS, 2015, p. 756.
- [17] M. D. Schnall, V. Harihara Subramanian, and J. S. Leigh, "The application of overcoupled tank circuits to NMR probe design," *Journal of Magnetic Resonance*, vol. 67, no. 1, pp. 129-134, 1986, doi: 10.1016/0022-2364(86)90416-6.
- [18] M. Meyerspeer, E. Seres Roig, R. Gruetter, and A. W. Magill, "An improved trap design for decoupling multinuclear RF coils," *Magn Reson Med*, vol. 72, no. 2, pp. 584-90, Aug 2014, doi: 10.1002/mrm.24931.
- [19] S. B. Bulumulla, K. J. Park, E. Fiveland, J. Iannotti, and F. Robb, "MEMS switch integrated radio frequency coils and arrays for magnetic resonance imaging," *Review of Scientific Instruments*, vol. 88, no. 2, 2017, doi: 10.1063/1.4975181.
- [20] C. H. Choi, J. M. Hutchison, and D. J. Lurie, "Design and construction of an actively frequency-switchable RF coil for field-dependent Magnetisation Transfer Contrast MRI with fast field-cycling," *J Magn Reson*, vol. 207, no. 1, pp. 134-9, Nov 2010, doi: 10.1016/j.jmr.2010.08.018.
- [21] J. C. Lindon and A. G. Ferrige, "Digitisation and data processing in Fourier transform NMR," (in English), *Progress in Nuclear Magnetic Resonance Spectroscopy*, vol. 14, no. 1, pp. 27-66, 1980, doi: 10.1016/0079-6565(80)80002-1.

- [22] T. A. Gallagher, A. J. Nemeth, and L. Hacin-Bey, "An introduction to the Fourier transform: relationship to MRI," *AJR Am J Roentgenol*, vol. 190, no. 5, pp. 1396-405, May 2008, doi: 10.2214/AJR.07.2874.
- [23] J. B. Lambert, C. D. Ridge, and E. P. Mazzola, *Nuclear Magnetic Resonance Spectroscopy : An Introduction to Principles, Applications, and Experimental Methods*. Newark, UNITED KINGDOM: John Wiley & Sons, Incorporated, 2019.
- [24] M. Karplus and J. A. Pople, "Theory of Carbon Nmr Chemical Shifts in Conjugated Molecules," (in English), *J Chem Phys*, vol. 38, no. 12, pp. 2803-&, 1963, doi: Doi 10.1063/1.1733605.
- [25] R. K. Harris, E. D. Becker, S. M. De Cabral Menezes, P. Granger, R. E. Hoffman, and K. W. Zilm, "Further Conventions for NMR shielding and chemical shifts (IUPAC recommendations 2008)," *Magnetic Resonance in Chemistry*, vol. 46, no. 6, pp. 582-598, Jun 2008, doi: 10.1002/mrc.2225.
- [26] S. W. Provencher, "Estimation of metabolite concentrations from localized in vivo proton NMR spectra," *Magn Reson Med*, vol. 30, no. 6, pp. 672-9, Dec 1993, doi: 10.1002/mrm.1910300604.
- [27] M. Wilson, G. Reynolds, R. A. Kauppinen, T. N. Arvanitis, and A. C. Peet, "A constrained least-squares approach to the automated quantitation of in vivo <sup>1</sup>H magnetic resonance spectroscopy data," *Magnetic resonance in medicine : official journal of the Society of Magnetic Resonance in Medicine / Society of Magnetic Resonance in Medicine*, vol. 65, no. 1, pp. 1-12, 2011, doi: 10.1002/mrm.22579.
- [28] B. J. Soher, P. Semanchuk, D. Todd, J. Steinberg, and K. Young, "VeSPA: Integrated applications for RF pulse design, spectral simulation and MRS data analysis," in *Intl. Soc. Mag. Reson. Med.*, 2011, 2011, p. 19.
- [29] L. Vanhamme, A. van den Boogaart, and S. Van Huffel, "Improved Method for Accurate and Efficient Quantification of MRS Data with Use of Prior Knowledge," (in English), *Journal of Magnetic Resonance*, vol. 129, no. 1, pp. 35-43, Nov 1997, doi: 10.1006/jmre.1997.1244.
- [30] G. J. Kemp, M. Meyerspeer, and E. Moser, "Absolute quantification of phosphorus metabolite concentrations in human muscle in vivo by <sup>31</sup>P MRS: a quantitative review," *NMR Biomed*, vol. 20, no. 6, pp. 555-65, Oct 2007, doi: 10.1002/nbm.1192.
- [31] M. Rata, S. L. Giles, N. M. deSouza, M. O. Leach, and G. S. Payne, "Comparison of three reference methods for the measurement of intracellular pH

- using  $^{31}\text{P}$  MRS in healthy volunteers and patients with lymphoma," *NMR Biomed*, vol. 27, no. 2, pp. 158-62, Feb 2014, doi: 10.1002/nbm.3047.
- [32] M. Meyerspeer *et al.*, " $^{31}\text{P}$  magnetic resonance spectroscopy in skeletal muscle: Experts' consensus recommendations," *NMR Biomed*, no. August 2019, p. e4246, Feb 10 2020, doi: 10.1002/nbm.4246.
- [33] J. Frahm, K. D. Merboldt, and W. Hanicke, "Localized Proton Spectroscopy Using Stimulated Echoes," (in English), *Journal of Magnetic Resonance*, vol. 72, no. 3, pp. 502-508, May 1987, doi: Doi 10.1016/0022-2364(87)90154-5.
- [34] P. A. Bottomley, "Selective volume method for performing localized NMR spectroscopy," United States Patent 4 480 228, 1987.
- [35] T. W. Scheenen, D. W. Klomp, J. P. Wijnen, and A. Heerschap, "Short echo time  $^1\text{H}$ -MRSI of the human brain at 3T with minimal chemical shift displacement errors using adiabatic refocusing pulses," *Magn Reson Med*, <https://doi.org/10.1002/mrm.21302> vol. 59, no. 1, pp. 1-6, Jan 2008, doi: 10.1002/mrm.21302.
- [36] S. Posse, C. DeCarli, and D. Le Bihan, "Three-dimensional echo-planar MR spectroscopic imaging at short echo times in the human brain," *Radiology*, vol. 192, no. 3, pp. 733-8, Sep 1994, doi: 10.1148/radiology.192.3.8058941.
- [37] R. J. Ordidge, A. Connelly, and J. A. B. Lohman, "Image-selected in Vivo spectroscopy (ISIS). A new technique for spatially selective nmr spectroscopy," *Journal of Magnetic Resonance*, vol. 66, no. 2, pp. 283-294, 1986, doi: 10.1016/0022-2364(86)90031-4.
- [38] A. N. Garroway, P. K. Grannell, and P. Mansfield, "Image-Formation in Nmr by a Selective Irradiative Process," (in English), *J Phys C Solid State*, vol. 7, no. 24, pp. L457-L462, 1974, doi: Doi 10.1088/0022-3719/7/24/006.
- [39] H. Y. Carr and E. M. Purcell, "Effects of Diffusion on Free Precession in Nuclear Magnetic Resonance Experiments," (in English), *Physical Review*, vol. 94, no. 3, pp. 630-638, 1954, doi: DOI 10.1103/PhysRev.94.630.
- [40] J. Frahm, A. Haase, and D. Matthaei, "Rapid NMR imaging of dynamic processes using the FLASH technique," *Magn Reson Med*, vol. 3, no. 2, pp. 321-7, Apr 1986, doi: 10.1002/mrm.1910030217.
- [41] P. Mansfield and A. A. Maudsley, "Medical imaging by NMR," *Br J Radiol*, vol. 50, no. 591, pp. 188-94, Mar 1977, doi: 10.1259/0007-1285-50-591-188.

- [42] W. A. Edelstein, J. M. Hutchison, G. Johnson, and T. Redpath, "Spin warp NMR imaging and applications to human whole-body imaging," *Phys Med Biol*, vol. 25, no. 4, pp. 751-6, Jul 1980, doi: 10.1088/0031-9155/25/4/017.
- [43] R. S. Likes, "Moving Gradient Zeugmatography," Unites States Patent 4307343 Patent Appl. 67697, 1979.
- [44] C. B. Ahn and Z. H. Cho, "Analysis of the eddy-current induced artifacts and the temporal compensation in nuclear magnetic resonance imaging," *IEEE Trans Med Imaging*, vol. 10, no. 1, pp. 47-52, 1991, doi: 10.1109/42.75610.
- [45] D. K. Sodickson and W. J. Manning, "Simultaneous acquisition of spatial harmonics (SMASH): fast imaging with radiofrequency coil arrays," *Magn Reson Med*, vol. 38, no. 4, pp. 591-603, Oct 1997, doi: 10.1002/mrm.1910380414.
- [46] M. A. Griswold *et al.*, "Generalized autocalibrating partially parallel acquisitions (GRAPPA)," *Magn Reson Med*, vol. 47, no. 6, pp. 1202-10, Jun 2002, doi: 10.1002/mrm.10171.
- [47] K. P. Pruessmann, M. Weiger, M. B. Scheidegger, and P. Boesiger, "SENSE: sensitivity encoding for fast MRI," *Magn Reson Med*, vol. 42, no. 5, pp. 952-62, Nov 1999. [Online]. Available: <https://www.ncbi.nlm.nih.gov/pubmed/10542355>.
- [48] P. Mansfield, "Multi-Planar Image-Formation Using NMR Spin Echoes," (in English), *J Phys C Solid State*, vol. 10, no. 3, pp. L55-L58, 1977, doi: 10.1088/0022-3719/10/3/004.
- [49] F. Hennel, F. Girard, and T. Loenneker, "'Silent' MRI with soft gradient pulses," *Magnetic Resonance in Medicine*, vol. 42, no. 1, pp. 6-10, 1999, doi: 10.1002/(SICI)1522-2594(199907)42:1<6::AID-MRM2>3.0.CO;2-D.
- [50] H. J. Landau, "Sampling, data transmission, and the Nyquist rate," *Proceedings of the IEEE*, vol. 55, no. 10, pp. 1701-1706, 1967, doi: 10.1109/proc.1967.5962.
- [51] A. B. Carlson and P. B. Grilly, *Communication Systems: An Introduction to Signals and Noise in Electrical Communication: Fifth Edition*. McGraw Hill.
- [52] A. Abinaya and M. Maheswari, "A survey of digital down converter architecture for next generation wireless applications," *IOP Conference Series: Materials Science and Engineering*, vol. 872, no. 1, 2020, doi: 10.1088/1757-899x/872/1/012037.



- [53] W. He, X. Qin, R. Jiejing, and L. Gengying, "Four-channel magnetic resonance imaging receiver using frequency domain multiplexing," *Rev Sci Instrum*, vol. 78, no. 1, p. 015102, Jan 2007, doi: 10.1063/1.2424426.
- [54] S. M. Wright and L. L. Wald, "Theory and application of array coils in MR spectroscopy," *NMR Biomed*, vol. 10, no. 8, pp. 394-410, Dec 1997, doi: 10.1002/(sici)1099-1492(199712)10:8<394::aid-nbm494>3.0.co;2-0.
- [55] E. G. Larsson, D. Erdogmus, R. Yan, J. C. Principe, and J. R. Fitzsimmons, "SNR-optimality of sum-of-squares reconstruction for phased-array magnetic resonance imaging," *J Magn Reson*, vol. 163, no. 1, pp. 121-3, Jul 2003, doi: 10.1016/s1090-7807(03)00132-0.
- [56] D. Erdogmus, E. G. Larsson, R. Yan, J. C. Principe, and J. R. Fitzsimmons, "Asymptotic SNR-performance of some image combination techniques for phased-array MRI," (in English), *Signal Processing*, vol. 84, no. 6, pp. 997-1003, Jun 2004, doi: 10.1016/j.sigpro.2004.03.003.
- [57] L. L. Wald, S. E. Moyher, M. R. Day, S. J. Nelson, and D. B. Vigneron, "Proton spectroscopic imaging of the human brain using phased array detectors," *Magn Reson Med*, vol. 34, no. 3, pp. 440-5, Sep 1995, doi: 10.1002/mrm.1910340322.
- [58] C. T. Rodgers and M. D. Robson, "Coil combination for receive array spectroscopy: Are data-driven methods superior to methods using computed field maps?," *Magn Reson Med*, vol. 75, no. 2, pp. 473-87, Feb 2016, doi: 10.1002/mrm.25618.
- [59] M. Wu, L. Fang, C. E. Ray, Jr., A. Kumar, and S. Yang, "Adaptively Optimized Combination (AOC) of Phased-Array MR Spectroscopy Data in the Presence of Correlated Noise: Compared with Noise-Decorrelated or Whitened Methods," *Magn Reson Med*, vol. 78, no. 3, pp. 848-859, Sep 2017, doi: 10.1002/mrm.26504.
- [60] E. M. Purcell, H. C. Torrey, and R. V. Pound, "Resonance absorption by nuclear magnetic moments in a single crystal of CaF<sub>2</sub>," vol. 69, ed, 1946, pp. 37-38.
- [61] E. M. Purcell, H. C. Torrey, and R. V. Pound, "Resonance Absorption by Nuclear Magnetic Moments in a Solid," *Phys. Rev*, vol. 69, 1946.
- [62] P. C. Lauterbur, "Some Application of C<sup>13</sup> Nuclear Magnetic Resonance Spectra to Organic Chemistry," *Annals of the New York Academy of Sciences*, vol. 135, no. 1, pp. 841-857, 1966, doi: 10.1111/j.1749-6632.1966.tb45498.x.

- [63] A. D. Buckingham, "Chemical Shifts in the Nuclear Magnetic Resonance Spectra of Molecules Containing Polar Groups," (in English), *Can J Chem*, vol. 38, no. 2, pp. 300-307, 1960, doi: DOI 10.1139/v60-040.
- [64] J. L. Burdett and M. T. Rogers, "Keto-Enol Tautomerism in Beta Dicarboxyls Studied by Nuclear Magnetic Resonance Spectroscopy .1. Proton Chemical Shifts + Equilibrium Constants of Pure Compounds," (in English), *J Am Chem Soc*, vol. 86, no. 11, pp. 2105-&, 1964, doi: DOI 10.1021/ja01065a003.
- [65] S. Barcza, "Molecular Weight Determination by N.M.R. Spectroscopy," (in English), *J Org Chem*, vol. 28, no. 7, pp. 1914-&, 1963, doi: DOI 10.1021/jo01042a515.
- [66] P. C. Lauterbur, "Image Formation by Induced Local Interactions: Examples Employing Nuclear Magnetic Resonance," *Nature*, vol. 242, pp. 190-191, 1973, doi: 10.1038/242190a0.
- [67] P. C. Lauterbur, "Magnetic resonance zeugmatography," *Pure and Applied Chemistry*, vol. 40, no. 1-2, pp. 149-157, 1974, doi: 10.1351/pac197440010149.
- [68] G. C. Wiggins, J. R. Polimeni, A. Potthast, M. Schmitt, V. Alagappan, and L. L. Wald, "96-Channel receive-only head coil for 3 Tesla: design optimization and evaluation," *Magn Reson Med*, vol. 62, no. 3, pp. 754-62, Sep 2009, doi: 10.1002/mrm.22028.
- [69] M. P. McDougall and S. M. Wright, "64-channel array coil for single echo acquisition magnetic resonance imaging," *Magn Reson Med*, vol. 54, no. 2, pp. 386-92, Aug 2005, doi: 10.1002/mrm.20568.
- [70] C. J. Hardy *et al.*, "128-channel body MRI with a flexible high-density receiver-coil array," *J Magn Reson Imaging*, vol. 28, no. 5, pp. 1219-25, Nov 2008, doi: 10.1002/jmri.21463.
- [71] R. Lee *et al.*, "A 128-channel Helium-3 Phased Array at 3T for Highly Accelerated Parallel Imaging in Hyperpolarized Gas MRI," *Proceedings 16th Scientific Meeting, International Society for Magnetic Resonance in Medicine*, no. January, pp. 440-440, 2008.
- [72] M. Schmitt *et al.*, "A 128-channel receive-only cardiac coil for highly accelerated cardiac MRI at 3 Tesla," *Magn Reson Med*, vol. 59, no. 6, pp. 1431-9, Jun 2008, doi: 10.1002/mrm.21598.
- [73] J. P. Kuhn *et al.*, "Proton-density fat fraction and simultaneous R2\* estimation as an MRI tool for assessment of osteoporosis," *Eur Radiol*, vol. 23, no. 12, pp. 3432-9, Dec 2013, doi: 10.1007/s00330-013-2950-7.

- [74] H. Johansen-Berg and T. E. J. Behrens, *Diffusion MRI : From Quantitative Measurement to in Vivo Neuroanatomy*. San Diego, UNITED STATES: Elsevier Science & Technology, 2014.
- [75] M. Markl, A. Frydrychowicz, S. Kozerke, M. Hope, and O. Wieben, "4D flow MRI," *J Magn Reson Imaging*, vol. 36, no. 5, pp. 1015-36, Nov 2012, doi: 10.1002/jmri.23632.
- [76] N. K. Logothetis, "What we can do and what we cannot do with fMRI," *Nature*, vol. 453, no. 7197, pp. 869-78, Jun 12 2008, doi: 10.1038/nature06976.
- [77] D. L. Arnold, P. M. Matthews, and G. K. Radda, "Metabolic Recovery after Exercise and the Assessment of Mitochondrial Function in Vivo in Human Skeletal Muscle by Means of  $^{31}\text{P}$  NMR," *Magnetic Resonance in Medicine*, no. 1, pp. 307-315, 1984, doi: 10.1002/mrm.1910010303.
- [78] J. A. Bankson *et al.*, "Kinetic Modeling and Constrained Reconstruction of Hyperpolarized  $[1-^{13}\text{C}]$ -Pyruvate Offers Improved Metabolic Imaging of Tumors," *Cancer Res*, vol. 75, no. 22, pp. 4708-17, Nov 15 2015, doi: 10.1158/0008-5472.CAN-15-0171.
- [79] Z. Gan, P. Gor'kov, T. A. Cross, A. Samoson, and D. Massiot, "Seeking higher resolution and sensitivity for NMR of quadrupolar nuclei at ultrahigh magnetic fields," *J Am Chem Soc*, vol. 124, no. 20, pp. 5634-5, May 22 2002, doi: 10.1021/ja025849p.
- [80] P. S. Belton, I. Delgadillo, E. Holmes, A. Nicholls, J. K. Nicholson, and M. Spraul, "Use of High-Field  $^1\text{H}$  NMR Spectroscopy for the Analysis of Liquid Foods," *Journal of Agricultural and Food Chemistry*, vol. 44, no. 6, pp. 1483-1487, 1996, doi: 10.1021/jf950640z.
- [81] J. K. Nicholson, P. J. Foxall, M. Spraul, R. D. Farrant, and J. C. Lindon, "750 MHz  $^1\text{H}$  and  $^1\text{H}$ - $^{13}\text{C}$  NMR spectroscopy of human blood plasma," *Anal Chem*, vol. 67, no. 5, pp. 793-811, Mar 1 1995, doi: 10.1021/ac00101a004.
- [82] L. Mannina, M. Patumi, N. Proietti, and A. L. Segre, "Geographical Characterization of Italian Extra Virgin Olive Oils Using High-Field  $^1\text{H}$  NMR Spectroscopy," *Journal of Agricultural and Food Chemistry*, vol. 49, no. 6, pp. 2687-2696, 2001.
- [83] U. S. F. D. Administration. "FDA clears first 7T magnetic resonance imaging device." <https://www.fda.gov/news-events/press-announcements/fda-clears-first-7t-magnetic-resonance-imaging-device> (accessed 12/5/21, 2021).

- [84] E. Moser, E. Laistler, F. Schmitt, and G. Kontaxis, "Ultra-High Field NMR and MRI—The Role of Magnet Technology to Increase Sensitivity and Specificity," *Frontiers in Physics*, vol. 5, no. AUG, pp. 1-15, 2017, doi: 10.3389/fphy.2017.00033.
- [85] C. Obyn and I. Cleemput, "The capital cost and productivity of MRI in a Belgian setting," *JBR-BTR*, vol. 93, no. 2, pp. 92-6, Mar-Apr 2010, doi: 10.5334/jbr-btr.148.
- [86] L. L. Wald, P. C. McDaniel, T. Witzel, J. P. Stockmann, and C. Z. Cooley, "Low-cost and portable MRI," *J Magn Reson Imaging*, vol. 52, no. 3, pp. 686-696, Sep 2020, doi: 10.1002/jmri.26942.
- [87] G. B. N. A. Office, *Managing high value capital equipment in the NHS in England*. London, United Kingdom: TSO, 2011.
- [88] Centers for Medicare & Medicaid Services. (2004). *CAG-00141N, Magnetic Resonance Spectroscopy for Brain Tumors*. [Online] Available: <https://www.cms.gov/medicare-coverage-database/view/ncacal-decision-memo.aspx?proposed=N&NCAId=52&fromdb=true>
- [89] M. A. Griswold, P. M. Jakob, M. Nittka, J. W. Goldfarb, and A. Haase, "Partially parallel imaging with localized sensitivities (PILS)," *Magn Reson Med*, vol. 44, no. 4, pp. 602-9, Oct 2000, doi: 10.1002/1522-2594(200010)44:4<602::aid-mrm14>3.0.co;2-5.
- [90] Z. Argov and W. J. Bank, "Phosphorus Magnetic Resonance Spectroscopy (31P MRS) in Neuromuscular Disorders," *Annals of Neurology*, pp. 90-97, 1991.
- [91] S. Blüml, K. J. Seymour, and B. D. Ross, "Developmental Changes in Choline- and Ethanolamine-Containing Compounds Measured With Proton-Decoupled 31P MRS in in Vivo Human Brain," *Magnetic Resonance in Medicine*, no. 42, pp. 643-654, 1999, doi: 10.1002/(SICI)1522-2594(199910)42:4<643::AID-MRM5>3.0.CO;2-N.
- [92] J. D. de Certaines, V. A. Larsen, F. Podo, and G. Carpinelli, "In Vivo 31P MRS of Experimental Tumours," *NMR in Biomedicine*, vol. 6, pp. 3455-365, 1993.
- [93] G. J. Kemp and G. K. Radda, "Quantitative Interpretation of Bioenergetic Data from 31P and 1H Magnetic Resonance Spectroscopic Studies of Skeletal Muscle: An Analytical Review," *Magnetic Resonance Quarterly*, vol. 10, no. 1, pp. 43-63, 1994.
- [94] J. Zhang *et al.*, "Functional and bioenergetic consequences of postinfarction left ventricular remodeling in a new porcine model. MRI and 31 P-MRS study,"

*Circulation*, vol. 94, no. 5, pp. 1089-100, Sep 1 1996, doi: 10.1161/01.Cir.94.5.1089.

- [95] P. A. Bottomley *et al.*, "Nmr Imaging Spectroscopy System to Study Both Anatomy and Metabolism," (in English), *Lancet*, vol. 2, no. 8344, pp. 273-274, July 30, 1983 1983, doi: 10.1016/S0140-6736(83)90250-7.
- [96] S. Zanconato, S. Buchthal, T. J. Barstow, and D. M. Cooper, "31P-magnetic resonance spectroscopy of leg muscle metabolism during exercise in children and adults," *Journal of Applied Physiology*, vol. 74, no. 5, pp. 2214-2218, 1993. [Online]. Available: [www.physiology.org/journal/jappl](http://www.physiology.org/journal/jappl).
- [97] W. Bogner, M. Chmelik, A. I. Schmid, E. Moser, S. Trattinig, and S. Gruber, "Assessment of 31P relaxation times in the human calf muscle: A comparison between 3 T and 7 T in vivo," *Magnetic Resonance in Medicine*, no. 62, pp. 574-582, 2009, doi: 10.1002/mrm.22057.
- [98] J. Ren, A. D. Sherry, and C. R. Malloy, "Modular (31) P wideband inversion transfer for integrative analysis of adenosine triphosphate metabolism, T1 relaxation and molecular dynamics in skeletal muscle at 7T," *Magn Reson Med*, vol. 81, no. 6, pp. 3440-3452, Jun 2019, doi: 10.1002/mrm.27686.
- [99] J. Ren, B. Yang, A. D. Sherry, and C. R. Malloy, "Exchange kinetics by inversion transfer: integrated analysis of the phosphorus metabolite kinetic exchanges in resting human skeletal muscle at 7 T," *Magn Reson Med*, vol. 73, no. 4, pp. 1359-69, Apr 2015, doi: 10.1002/mrm.25256.
- [100] C. T. Rodgers, W. T. Clarke, C. Snyder, J. T. Vaughan, S. Neubauer, and M. D. Robson, "Human cardiac 31P magnetic resonance spectroscopy at 7 Tesla," *Magn Reson Med*, vol. 72, no. 2, pp. 304-15, Aug 2014, doi: 10.1002/mrm.24922.
- [101] A. Santos-Diaz, D. Harasym, and M. D. Noseworthy, "Dynamic (31) P spectroscopic imaging of skeletal muscles combining flyback echo-planar spectroscopic imaging and compressed sensing," *Magn Reson Med*, vol. 81, no. 6, pp. 3453-3461, Jun 2019, doi: 10.1002/mrm.27682.
- [102] S. Ghazinoor, J. V. Crues, and C. Crowley, "Low-field musculoskeletal MRI," *Journal of Magnetic Resonance Imaging*, no. 25, pp. 234-244, 2007, doi: 10.1002/jmri.20854.
- [103] T. Carrell, M. Gu, M. P. McDougall, and S. M. Wright, "Feasibility of Using a 1T Extremity Scanner with a Four-Element Array to Detect 31P in the Human Calf," in *2019 41st Annual International Conference of the IEEE Engineering in Medicine and Biology Society (EMBC)*

Berlin, DE, 2019, pp. 6806-6809, doi: 10.1109/EMBC.2019.8857122.

- [104] P. Jezzard and R. S. Balaban, "Correction for geometric distortion in echo planar images from B0 field variations," *Magn Reson Med*, vol. 34, no. 1, pp. 65-73, Jul 1995, doi: 10.1002/mrm.1910340111.
- [105] D. K. Deelchand, T. M. Nguyen, X.-H. Zhu, F. Mochel, and P.-G. Henry, "Quantification of in vivo 31P NMR Brain Spectra using LCMoDel," *NMR in Biomedicine*, vol. 28, no. 6, pp. 633-641, 2015, doi: 10.1016/j.physbeh.2017.03.040.
- [106] S. Ogier, J. C. Bosshard, and S. M. Wright, "A Broadband Spectrometer for Simultaneous Multinuclear Magnetic Resonance Imaging and Spectroscopy," in *International Society for Magnetic Resonance in Medicine*, Singapore, 2016. [Online]. Available: <https://archive.ismrm.org/2016/0546.html>. [Online]. Available: <https://archive.ismrm.org/2016/0546.html>
- [107] D. M. Peterson, B. L. Beck, C. R. Duensing, and J. R. Fitzsimmons, "Common mode signal rejection methods for MRI: Reduction of cable shield currents for high static magnetic field systems," (in English), *Concept Magn Reson B*, vol. 19b, no. 1, pp. 1-8, Oct 2003, doi: 10.1002/cmr.b.10090.
- [108] R. K. Mongia, I. J. Bahl, P. Bhartia, and J. Hong, *RF and Microwave Coupled-Line Circuits*, 2 ed. Artech House, 2007, pp. 230-233.
- [109] M. Gu, "Dynamic 31P MRS With a 1 Tesla Extremity Scanner," Master of Science, Department of Electrical and Computer Engineering, Texas A&M University, 2019. [Online]. Available: <https://hdl.handle.net/1969.1/186175>
- [110] F. D. Doty, T. J. Connick, X. Z. Ni, and M. N. Clingan, "Noise in high-power, high-frequency double-tuned probes," *Journal of Magnetic Resonance (1969)*, no. 77, pp. 536-549, 1988, doi: 10.1016/0022-2364(88)90011-X.
- [111] G. J. Kemp, M. Meyerspeer, and E. Moser, "Absolute quantification of phosphorus metabolite concentrations in human muscle in vivo by 31P MRS: A quantitative review," *NMR in Biomedicine*, vol. 20, pp. 555-565, 2007, doi: 10.1002/nbm.1192.
- [112] R. R. Ernst and W. A. Anderson, "Application of Fourier Transform Spectroscopy to Magnetic Resonance," *The Review of Scientific Instruments*, vol. 37, no. 1, pp. 93-102, 1966.
- [113] B. R. Newcomer and M. D. Boska, "T1 Measurements of 31 P Metabolites in Resting and Exercising Human Gastrocnemius/Soleus Muscle at 1.5 Tesla," *Magnetic Resonance in Medicine*, no. 41, pp. 486-494, 1999.

- [114] P. A. Bottomley, C. J. Hardy, and R. G. Weiss, "Correcting human heart  $^{31}\text{P}$  NMR spectra for partial saturation. Evidence that saturation factors for PCr/ATP are homogeneous in normal and disease states," *Journal of Magnetic Resonance*, vol. 95, no. 2, pp. 341-355, 1991, doi: 10.1016/0022-2364(91)90223-g.
- [115] S. M. Wright and L. L. Wald, "Theory and Application of Array Coils in MR Spectroscopy," *NMR in Biomedicine*, vol. 10, pp. 394-410, 1997.
- [116] D. Stefan *et al.*, "Quantitation of magnetic resonance spectroscopy signals: the jMRUI software package," *Meas Sci Technol*, vol. 20, no. 10, pp. 104035-104035, 2009, doi: 10.1088/0957-0233/20/10/104035.
- [117] J. M. Bonny and G. Pages, "Uncertainties of calculated Cramer-Rao lower bounds: implications for quantitative MRS," *Magn Reson Med*, vol. 81, no. 2, pp. 759-764, Feb 2019, doi: 10.1002/mrm.27415.
- [118] R. A. Meyer, "A linear model of muscle respiration explains monoexponential phosphocreatine changes," *Am J Physiol*, vol. 254, no. 4 Pt 1, pp. C548-53, Apr 1988, doi: 10.1152/ajpcell.1988.254.4.C548.
- [119] A. Kumar, W. A. Edelstein, and P. A. Bottomley, "Noise figure limits for circular loop MR coils," *Magnetic Resonance in Medicine*, no. 61, pp. 1201-1209, 2009, doi: 10.1002/mrm.21948.
- [120] B. Chance, J. Im, S. Nioka, and M. Kushmerick, "Skeletal muscle energetics with PNMR: Personal views and historic perspectives," *NMR in Biomedicine*, vol. 19, no. 7, pp. 904-926, Nov 2006, doi: 10.1002/nbm.1109.
- [121] A. Santos-Diaz, D. Harasym, and M. D. Noseworthy, "Dynamic  $^{31}\text{P}$  spectroscopic imaging of skeletal muscles combining flyback echo-planar spectroscopic imaging and compressed sensing," *Magn Reson Med*, vol. 81, no. 6, pp. 3453-3461, Jun 2019, doi: 10.1002/mrm.27682.
- [122] E. D. Becker, J. A. Ferretti, and P. N. Gambhir, "Selection of Optimum Parameters for Pulse Fourier Transform Nuclear Magnetic Resonance," (in English), *Anal Chem*, vol. 51, no. 9, pp. 1413-1420, 1979, doi: 10.1021/ac50045a016.
- [123] A. W. Overhauser, "Polarization of Nuclei in Metals," *Physical Review*, vol. 92, no. 2, pp. 411-415, 1953, doi: 10.1103/PhysRev.92.411.
- [124] L. Darrasse and J. C. Ginefri, "Perspectives with cryogenic RF probes in biomedical MRI," *Biochimie*, vol. 85, no. 9, pp. 915-37, Sep 2003, doi: 10.1016/j.biochi.2003.09.016.

- [125] P. Styles, N. F. Soffe, and C. A. Scott, "An Improved Cryogenically Cooled Probe for High-Resolution NMR," *Journal of Magnetic Resonance*, vol. 84, no. 2, pp. 376-378, 1989, doi: 10.1016/0022-2364(89)90383-1.
- [126] L. T. Muftuler, G. Gulsen, K. D. Sezen, and O. Nalcioglu, "Automatic tuned MRI RF coil for multinuclear imaging of small animals at 3T," *J Magn Reson*, vol. 155, no. 1, pp. 39-44, Mar 2002, doi: 10.1006/jmre.2002.2510.
- [127] S. B. Bulumulla, E. Fiveland, K. Park, and J. Iannotti, "MEMS Reconfigurable Coils," *Proc. Intl. Soc. Mag. Reson. Med.*, no. 23, pp. 1797-1797, 2015, doi: 10.1002/mrm.25156.
- [128] C. H. Choi, S. M. Hong, Y. Ha, and N. J. Shah, "Design and construction of a novel (1)H/(19)F double-tuned coil system using PIN-diode switches at 9.4T," *J Magn Reson*, vol. 279, pp. 11-15, Jun 2017, doi: 10.1016/j.jmr.2017.04.005.
- [129] S. Ha, M. J. Hamamura, O. Nalcioglu, and L. T. Muftuler, "A PIN diode controlled dual-tuned MRI RF coil and phased array for multi nuclear imaging," *Physics in Medicine and Biology*, vol. 55, no. 9, pp. 2589-2600, 2010, doi: 10.1088/0031-9155/55/9/011.
- [130] A. Maunder, M. Rao, F. Robb, and J. Wild, "RF coil design for multi-nuclear lung MRI of 19F fluorinated gases and 1H using MEMS," *Proc. Intl. Soc. Mag. Reson. Med.*, no. 24, pp. 3504-3504, 2016.
- [131] M. Fuentes, E. Weber, S. Wilson, B. Li, and S. Crozier, "Micro-Electromechanical Systems ( MEMS ) based RF-switches in MRI – a performance study," *Proc. Intl. Soc. Mag. Reson. Med.*, no. 18, pp. 422-422, 2010, doi: 10.1002/pds.
- [132] A. Maunder, M. Rao, F. Robb, and J. M. Wild, "Comparison of MEMS switches and PIN diodes for switched dual tuned RF coils," *Magnetic Resonance in Medicine*, vol. 80, no. 4, pp. 1746-1753, 2018, doi: 10.1002/mrm.27156.
- [133] D. Spence and A. Macro, "Custom MEMS switch for MR surface coil decoupling," *Proc. Intl. Soc. Mag. Reson. Med.*, no. 23, pp. 704-704, 2015.
- [134] S. E. Ogier *et al.*, "A Frequency Translation System for Multi-Channel, Multi-Nuclear MR Spectroscopy," *IEEE Trans Biomed Eng*, vol. 68, no. 1, pp. 109-118, Jan 2021, doi: 10.1109/TBME.2020.2997770.
- [135] M. Hutchinson and U. Raff, "Sub-second MRI Data Acquisition Using Multiple Detectors," in *Society for Magnetic Resonance in Medicine, 6th Annual Meeting*, New York, 1987, p. 459.



- [136] M. Hutchinson and U. Raff, "Fast MRI data acquisition using multiple detectors," *Magn Reson Med*, vol. 6, no. 1, pp. 87-91, Jan 1988, doi: 10.1002/mrm.1910060110.
- [137] V. Ramachandran, "Impedance Matching by Uniform Transmission Lines," *IETE Journal of Education*, vol. 3, no. 2, pp. 70-81, 1962, doi: 10.1080/09747338.1962.11467669.
- [138] M. Corp., *The PIN Diode Circuit Designers' Handbook*.
- [139] D. G. Brown, M. P. McDougall, and S. M. Wright, "Receiver design for parallel imaging with large arrays," in *10th Annual Meeting of ISMRM*, Honolulu, 2002, p. 863.
- [140] P. B. Roemer, W. A. Edelstein, C. E. Hayes, S. P. Souza, and O. M. Mueller, "The NMR phased array," *Magn Reson Med*, vol. 16, no. 2, pp. 192-225, Nov 1990, doi: 10.1002/mrm.1910160203.
- [141] E. L. Hall, M. C. Stephenson, D. Price, and P. G. Morris, "Methodology for improved detection of low concentration metabolites in MRS: optimised combination of signals from multi-element coil arrays," *Neuroimage*, vol. 86, pp. 35-42, Feb 1 2014, doi: 10.1016/j.neuroimage.2013.04.077.
- [142] L. An, J. Willem van der Veen, S. Li, D. M. Thomasson, and J. Shen, "Combination of multichannel single-voxel MRS signals using generalized least squares," *J Magn Reson Imaging*, vol. 37, no. 6, pp. 1445-50, Jun 2013, doi: 10.1002/jmri.23941.
- [143] M. A. Brown, "Time-domain combination of MR spectroscopy data acquired using phased-array coils," *Magn Reson Med*, vol. 52, no. 5, pp. 1207-13, Nov 2004, doi: 10.1002/mrm.20244.
- [144] Z. Dong and B. Peterson, "The rapid and automatic combination of proton MRSI data using multi-channel coils without water suppression," *Magn Reson Imaging*, vol. 25, no. 8, pp. 1148-54, Oct 2007, doi: 10.1016/j.mri.2007.01.005.
- [145] N. Sandgren, P. Stoica, F. J. Frigo, and Y. Selen, "Spectral analysis of multichannel MRS data," *J Magn Reson*, vol. 175, no. 1, pp. 79-91, Jul 2005, doi: 10.1016/j.jmr.2005.03.019.
- [146] N. Maril and R. E. Lenkinski, "An automated algorithm for combining multivoxel MRS data acquired with phased-array coils," *J Magn Reson Imaging*, vol. 21, no. 3, pp. 317-22, Mar 2005, doi: 10.1002/jmri.20261.

- [147] J. Near *et al.*, "Preprocessing, analysis and quantification in single-voxel magnetic resonance spectroscopy: experts' consensus recommendations," *NMR Biomed*, vol. 34, no. 5, p. e4257, May 2021, doi: 10.1002/nbm.4257.
- [148] L. A. B. Purvis, W. T. Clarke, L. Biasioli, L. Valkovic, M. D. Robson, and C. T. Rodgers, "OXSA: An open-source magnetic resonance spectroscopy analysis toolbox in MATLAB," *PLoS One*, vol. 12, no. 9, p. e0185356, 2017, doi: 10.1371/journal.pone.0185356.
- [149] W. T. Clarke, C. J. Stagg, and S. Jbabdi, "FSL-MRS: An end-to-end spectroscopy analysis package," *Magn Reson Med*, vol. 85, no. 6, pp. 2950-2964, Jun 2021, doi: 10.1002/mrm.28630.
- [150] M. Gajdosik, K. Landheer, K. M. Swanberg, and C. Juchem, "INSPECTOR: free software for magnetic resonance spectroscopy data inspection, processing, simulation and analysis," *Sci Rep*, vol. 11, no. 1, p. 2094, Jan 22 2021, doi: 10.1038/s41598-021-81193-9.
- [151] G. Oeltzschner *et al.*, "Osprey: Open-source processing, reconstruction & estimation of magnetic resonance spectroscopy data," *J Neurosci Methods*, vol. 343, no. February, p. 108827, Sep 1 2020, doi: 10.1016/j.jneumeth.2020.108827.
- [152] R. Simpson, G. A. Devenyi, P. Jezzard, T. J. Hennessy, and J. Near, "Advanced processing and simulation of MRS data using the FID appliance (FID-A)-An open source, MATLAB-based toolkit," *Magn Reson Med*, vol. 77, no. 1, pp. 23-33, Jan 2017, doi: 10.1002/mrm.26091.
- [153] *MATLAB Runtime*. (2021). [Online]. Available: <https://www.mathworks.com/products/compiler/matlab-runtime.html>
- [154] T. P. Zielinski, K. Duda, and K. Ostrowska, "Fast MinMax energy-based phase correction method for NMR spectra with linear phase distortion," *J Magn Reson*, vol. 281, pp. 104-117, Aug 2017, doi: 10.1016/j.jmr.2017.05.014.
- [155] Y. Xi and D. M. Rocke, "Baseline correction for NMR spectroscopic metabolomics data analysis," *BMC Bioinformatics*, vol. 9, p. 324, Jul 29 2008, doi: 10.1186/1471-2105-9-324.
- [156] C. T. Rodgers and M. D. Robson, "Receive array magnetic resonance spectroscopy: Whiten singular value decomposition (WSVD) gives optimal Bayesian solution," *Magn Reson Med*, vol. 63, no. 4, pp. 881-91, Apr 2010, doi: 10.1002/mrm.22230.
- [157] R. R. Ernst, G. Bodenhausen, and A. Wokaun, *Principles of Nuclear Magnetic Resonance in One and Two Dimensions*. Oxford, UK: Clarendon Press, 1987.

## APPENDIX A

Summary: The following material contains the protocol and checklist that was utilized for the volunteer study performed in Chapter II.1. This protocol includes the steps to be performed before the arrival of any patient, steps to be performed to acclimate the patient to the exercise protocol, parameters and settings for the protocol, and the initial post-processing and data handling of patient data.

### **A. 1 Protocol for $^{31}\text{P}$ & $^1\text{H}$ Patient Calf Test**

*Steps 1-7 should be completed before the patient arrives at the USB lab.*

#### **A.1.1 Transmit coil tuning and placement**

The transmit coil should be placed inside the magnet bore where the distance from the front laser to the face of the transmit coil is 6.3 cm (rubber stoppers will already be placed in the bore). Using the bias tee and 5 V of direct current, the RF+DC line should be attached to the leftmost port (90° port) of the transmit coil whenever the baluns are rotated to be at the bottom of the transmit coil, as shown in Figure 34. The rightmost port (0° port) should be terminated in a 50 ohm load while tuning the 90° port to at least -20 dB. A phantom is not required to be present during tuning. In order to properly tune the 0° port, +5V DC must be fed to the 90° port through the bias tee while tuning the 0° port with only the RF signal from the network analyzer. DC current should not be inputted into the 0° port. The quadrature combiner should then be attached to the coil. The cables coming from the quadrature combiner should be crossed so that the labeled 0-degree port on the quadrature combiner connects to the rightmost balun and the 90-degree port on the

quadrature combiner connects to the leftmost balun on the transmit coil, as seen in the figure below. This configuration ensures quadrature operation of the transmit coil. While terminating the isolation port of the quadrature combiner in 50 ohms, check the S11 of the input port to ensure -20 dB or less. Note: if the network analyzer reads greater than -20 dB, be sure to check proper calibration with the entire length of cable used in the measurement. Calibration can also be checked by verifying the signal levels received from the physiological phantom.

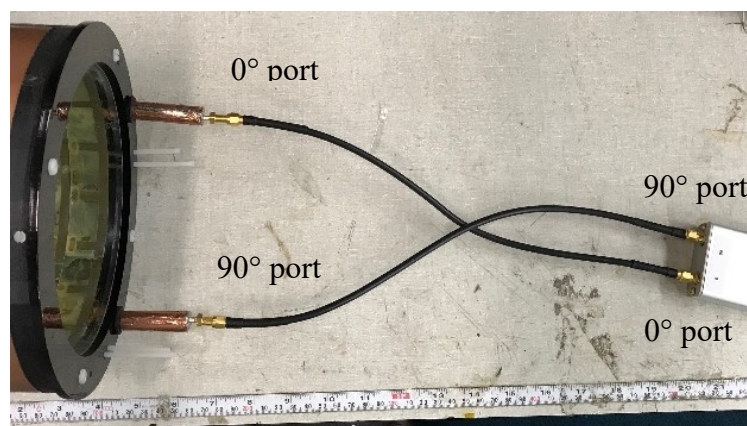


**Figure 34. Transmit coil cable attachment guide.**

### **A.1.2 Receive coil placement**

The transmit coil should be detached and removed from the bore. The receive elements should then be slid into the transmit coil and be bolted onto the back face of the transmit coil along with the balun cover, shown in the Figure 35, prior to insertion into the bore. The coil system should then be reinserted into the bore up to the 6.3 cm mark. The

torque stopper should then be turned to hold the transmit coil in place. Rubber stoppers should then be placed on the bore on the patient side of the transmit coil to ensure the coil system doesn't shift within the bore. The cables for the transmit coil should be reattached as in Step 1. Following placing the physiological phantom on the receive former, all four receive coils should be verified to be tuned to approximately -20 dB (Note: the power on the network analyzer should be turned down to -15 dBm).



**Figure 35. Proper receive coil insertion and balun cover attachment to the transmit coil.**

### **A.1.3 1st Stage Preamplifier**

There are four receive coil cables to be attached to their respective balun and cable. Starting on the righthand side and working to the left, the cables coming off of the receive should be hooked up to F2 (Figure-8 #2), F1 (Figure-8 #1), L1 (Loop #1), and L2 (Loop #2), as shown in . The cables and baluns coming from the receive coil should be directed between the layers of acrylic of the foot flexor stand. Blue foam should then be placed underneath the balun cover and over the cables until the foot flexor stand. No cable should be visible to the patient. The DC input signal of 15 V should be inputted into the left most

port on the input side of the preamplifier box. Cables coming from the output of the preamplifier box should be attached to the connector panel of the magnet room.

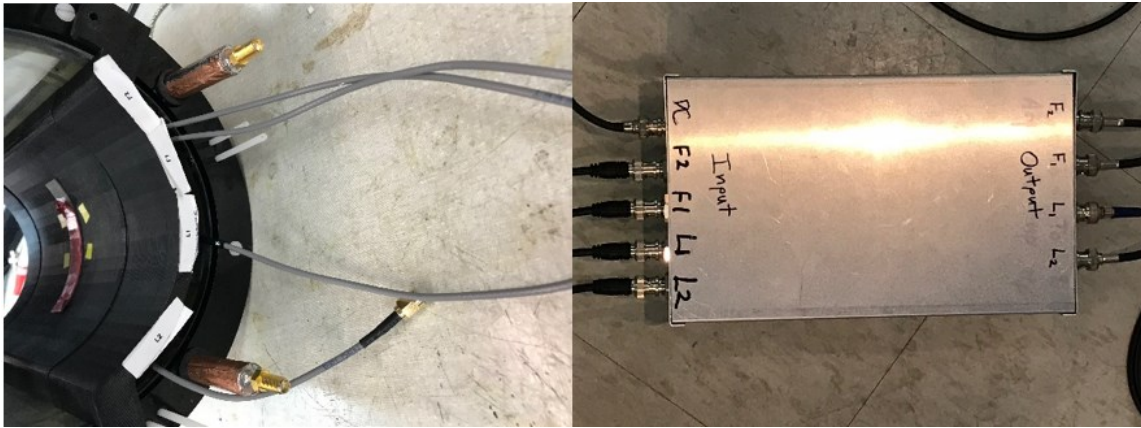


**Figure 36. Receive coil and preamplifier box attachment guide.**

#### **A.1.4 Second stage preamplifiers**

Once outside of the magnet room, the cables corresponding to F2 (Figure-8 #2), F1 (Figure-8 #1), L2 (Loop #2), and L1 (Loop #1) should be connected to their corresponding second stage preamplifier. The preamplifiers should be powered with the same +15 V DC as the first stage amplifier box. After each amplifier, there should be a series low and high pass filter (bandpass filter) for the correct frequency band, in this case 17.24 MHz should be encompassed, as shown in Figure 37.

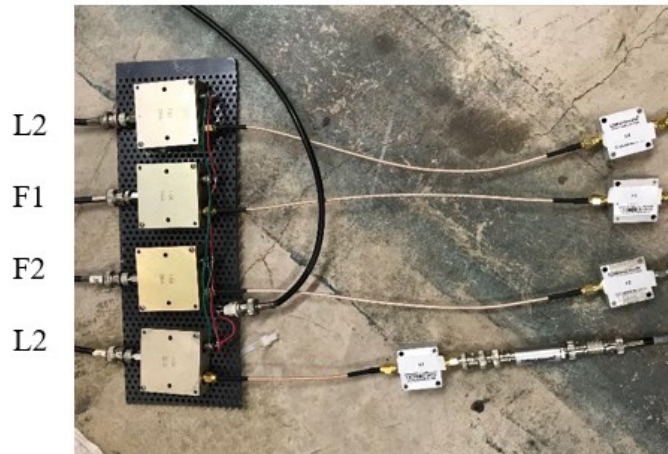


**Figure 37. Second stage preamplifiers with respective low and high pass filters.**

1. Digitizer/computer input – The output of the bandpass filter should be inputted into the following input ports to be digitized: IN0 = L1 (Loop #1), IN1 = F1 (Figure-8 #1), IN2 = L2 (Loop #2), IN3 = F2 (Figure-8 #2). A limiter should be present in between the cables coming from the second stage amplifiers and the cables running to the digitizer, as shown in Figure 38.



**Figure 38. Proper coil attachment with limiters shown.**

### **A.1.5 Foot flexor stand placement**

The foot flexor stand should be inserted so that the two acrylic sheets are on either side of the metal foot plate coming off of the magnet. In placing the stand, ensure that no wires are compressed underneath the legs. Using a piece of foam in between the acrylic clamp (on the bottom sheet of acrylic) and metal foot plate, tighten the clamp until the foam is compressed and the table has no lateral movement. The inserts for the foot pedal will be adjusted to the appropriate distance based on measurements gathered during the CTRLAL screenings.

### **A.1.6 Calibration Verification Steps**

The pure phosphoric acid phantom should be placed on the receive coils with the lid of the bottle being 9 cm from the laser. Open the **'Pulse Sequence\_Case\_structure.vi'** (Figure 39), which controls the pulse sequence parameters. All files for the  $^{31}\text{P}$  scans are accessible through a folder on the desktop labeled "CTRLAL protocol." Set the parameters within the VI to those in Figure 39 and in Table 18.



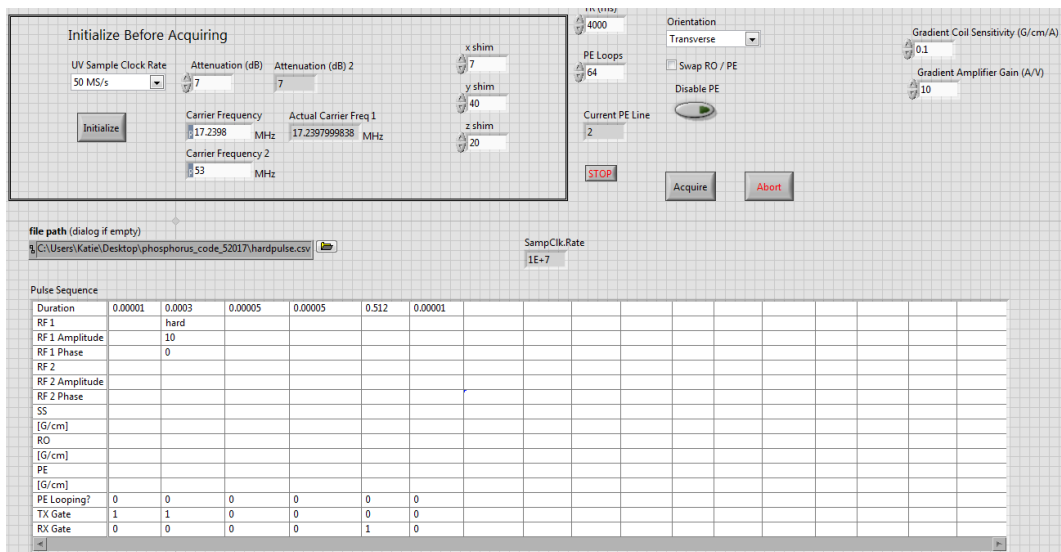


**Figure 39. Front panel view of the Pulse Sequence\_Case\_structure.vi.**

**Table 18. Scan parameters for the shimming calibration.**

UV Sample Clock Rate	50 MS/s
Attenuation	7 dB
Carrier Frequency	17.2398 MHz
Carrier Frequency 2	53
X shim	7
Y shim	40
Z shim	20
TR	4000 ms
PE Loops	64
Orientation	Transverse

If the pulse sequence has not updated to the desired parameters of 300 us pulse duration and 0.512 seconds for the acquisition time, then open ‘**hardpulse.csv**’ and manually change the .csv file to match Figure 40.

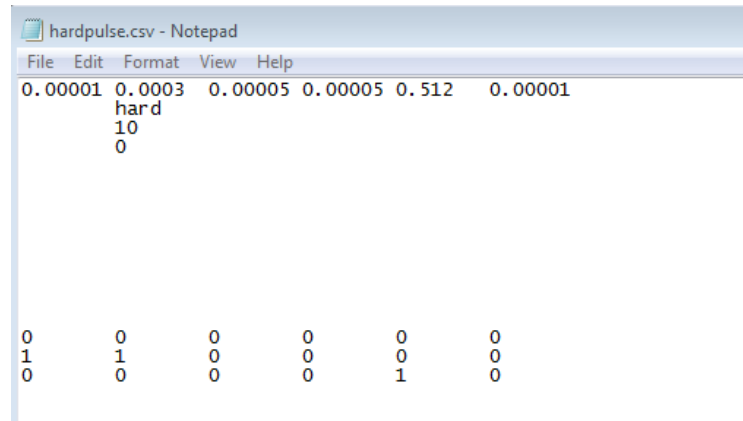


**Figure 40. CSV file for a 300 us pulse duration.**

The pulse duration is represented by the 1st row, 2nd column and the 0.512 acquisition time is shown in the 1st row, 5th column.

### Using the UltraVIEW software for power calibration and shimming.

Open 'LabVIEW\_Acquire\_Data\_x64.exe'. Two LabVIEW files, 'PCIe DAQ.lvlib:ReadandGraph.vi' and 'PCIe DAQ.lvlib:SetupandControl.vi', will open as a result (Figure 41). First, click the TTL and Time buttons on the ReadandGraph.vi so that the buttons become a light gray. Click the "dB on" button so that it is no longer green. Then change the "Spectrum Window" to "None." Click the "Acquire and Display" tab. Then, match the parameters found in the SetupandControl.vi to those in Figure 41. These settings are selecting Loops 1 & 2 for reception. Save the parameters after inputting everything. Note: Be sure that the "Trigger Mode" says "sync selective" after all changes have been made. If the ADC Clock Freq setting doesn't update to 50, then in the 'Pulse Sequence\_Case\_structure.vi,' run the VI and click initialize. After this, the clock should update.

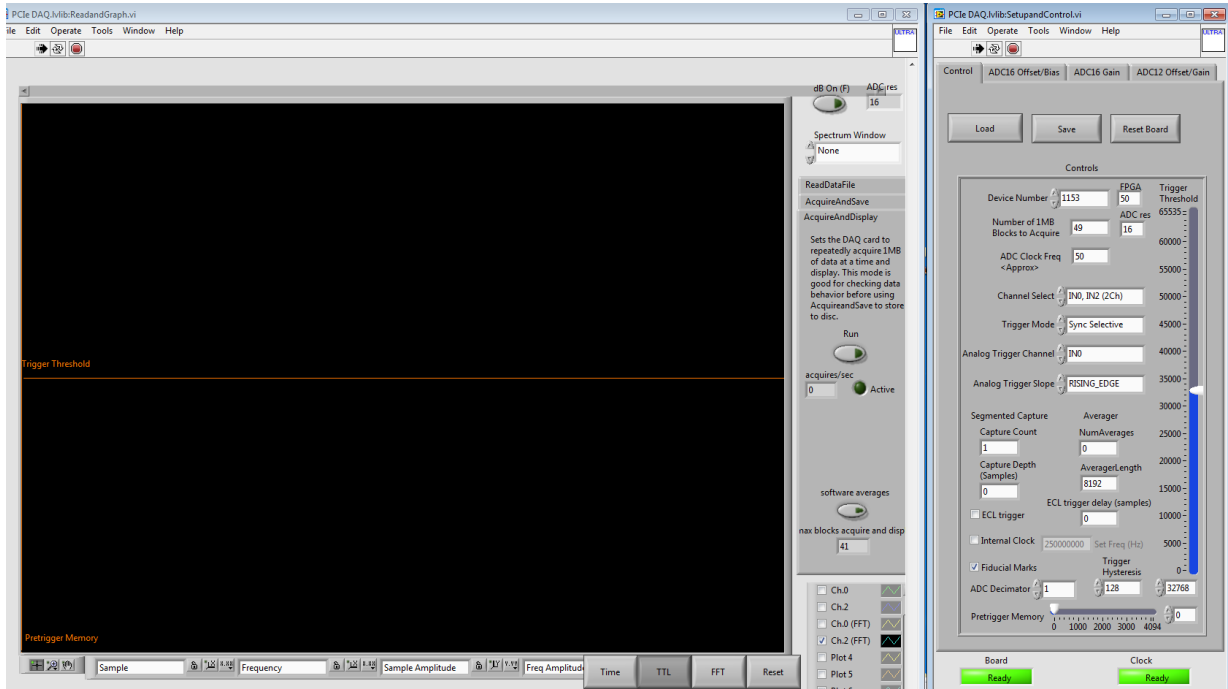


**Figure 41. Ultraview card control vi.**

Uncheck the internal clock to make the UV card use external clock frequency 50 MHz and change capture counts to 1, check the fiducial marks for separating each average's data, input Num. of Blocks as 49, choose channels IN0 and IN2 for shimming calibrations, select Trigger mode as 'sync selective' to active the external Rx gate.

On the '**ReadandGraph.vi**' window, click the "run" button. Then run the '**Pulse Sequence\_Case\_structure.vi.**' The graph on the '**ReadandGraph.vi**' will need to be rescaled before the spectrum is visible. To do this, click the button shown on the left of Figure 42 highlighted in red, which will be at the bottom left-hand corner of the graph. This will zoom the window completely out. Then click on the top number on the y-scale of the graph and type in the number 1. This will adjust the scale so that the spectrum should be visible. Then select the zoom button, shown on the side of Figure 42, which will allow

the frequencies of choice to be boxed in order to zoom to that particular region. The spectrum will be around 17.23 MHz.

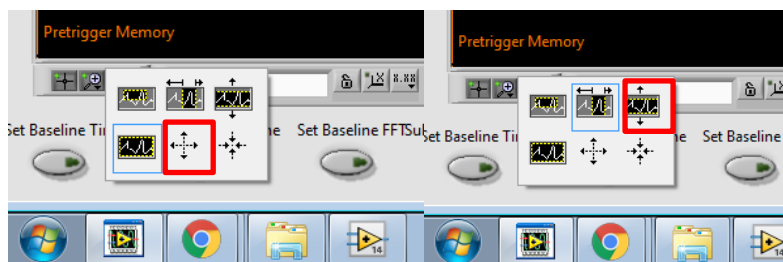


**Figure 42. Ultraview ‘ReadandGraph.vi’ controls for zooming out (left) and selecting a region to which to zoom (right).**

Manually alternate the shim values on the ‘**Pulse Sequence\_Case\_structure.vi**’ until both Loops 1 and 2 have similar narrow linewidths. Typically, the signal level for each peak will be above the y-scale setting of 1. Once a maximum is found that results in a strong signal with a narrow linewidth for both channels, proceed to the power calibration. Keep these shim values for the duration of the experiment day. Note: shim settings typically take one or two pulses in order to update.

Following adjusting the shim, sweep the attenuation from 16 dB to 6 dB in the ‘**Pulse Sequence\_Case\_structure.vi**’ while observing the peak signal strength on the frequency domain graph to find the maximum signal level and thus optimal power. Use one acquisition (PE loop = 1) for each power level and wait for more than 6 seconds for all the spins to relax. 7 dB is the typical value for a 90 degree tip. The value found in this

section will be used for the physiological phantom test and the first *in vivo* steady state test.

In addition to the full phosphoric acid phantom, the physiological phantom should be used to verify the proper working of the Ultraview card. Remove the phosphoric acid phantom and replace it with the physiological phantom where the laser to the cap of the bottle is 10.5 cm. On the '**Pulse Sequence\_Case\_structure.vi**', change the number of PE loops to 17 (16 averages). Adjust the values of the '**SetupandControl.vi**' to where the number of 1 MB blocks is 3125, capture count is 16, channel select is IN0, IN1, IN2, and IN3, and the trigger is sync selective. Press the "save" button on the VI. Then on the '**ReadandGraph.vi**,' press the "AcquireandSave" tab. Using the file explore button, name the file where the data is to be stored "phys\_test\_date.dat". Unclick the FFT button. Now press the run button on the VI to get it ready to save after the first pulse of the '**Pulse Sequence\_Case\_structure.vi**'. Then click the "Acquire" button within the '**Pulse Sequence\_Case\_structure.vi**'.

Using the Matlab file "UVload\_spectfor31p\_4channels\_individual\_averages\_T.m", enter the name of the file (phys\_test\_date.dat) and click run. Using a 3 Hz line broadening factor should give a combined 4-channel SNR of 44.4 ( $c_1 = 24.5$ ,  $c_2 = 23.9$ ,  $c_3 = 18.8$ ,  $c_4 = 16.0$ ). The physiological sample PCr, which is the metabolite being used to calculate the SNR, will decrease over time due to decaying of the compounds in the sample. The main outcome of this test is to ensure that the Ultraview card is working correctly and all the channels have a similar SNR.

### A.1.7 Scan Parameters

Change the settings of the ‘Pulse Sequence\_Case\_structure.vi’ to those shown in Figure 43 and in Table 19 to get ready for the steady state acquisition. Change the pulse duration within the ‘hardpulse.csv’ from 0.003 to 0.00205 (second column on the first row).

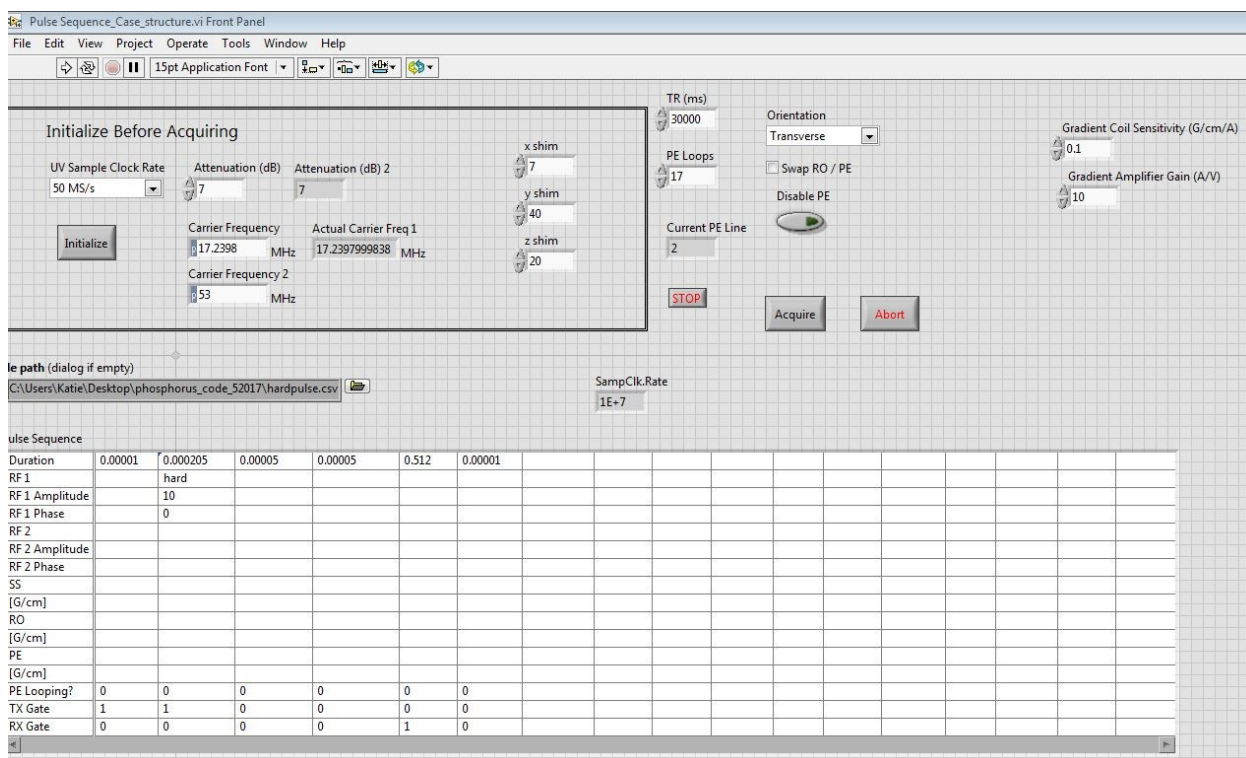


**Figure 43. Pulse sequence settings for the steady state acquisitions with a long TR of 30000 ms and 90 degree tip angle.**

**Table 19. Scan parameters for performing the steady state acquisition with 12 averages and a TR of 30 sec.**

TR	30000 ms
PE loops	13
Pulse duration	205 $\mu$ s

Match the parameters found in the SetupandControl.vi to those in Figure 44. Save the parameters after inputting everything. Next, click the open folder button on the ReadandGraph.vi next to the save to file dialog box. Input the correctly de-identified labelling system for the specified patient, e.g. '26\_patient\_id\_steady\_state.dat'. Note: Be sure to include the .dat file extension in the name.

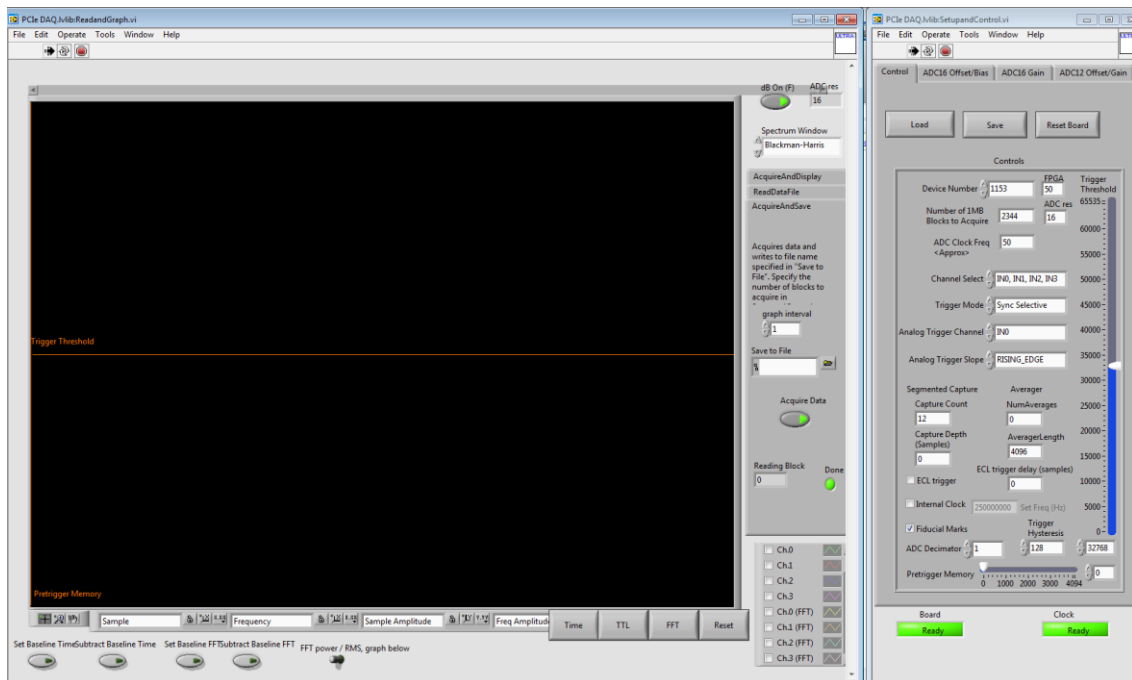


**Figure 44. Ultraview card control vi.**

Uncheck the internal clock to make the UV card use external clock frequency 50MHZ and change capture counts to 12, check the fiducial marks for separating each average's data, input Num. of Blocks calculated from your scan parameters, choose channels IN0, IN1, IN2, and IN3 for acquiring four channel data, select Trigger mode as 'sync selective' to active the external Rx gate.

### **A.1.8 Patient Preparation and Placement**

Following the power calibration steps, remove the phantom and ensure all cables are covered. Greet the patient outside of the magnet room and ensure that proper attire is being worn (no Lululemon yoga pants or baggie pants). The patient must remove all metal jewelry and verify that they have no pacemakers or other implanted electronic device. If the patient has any joint implants, their doctor's approval is required before scanning.

Prior to the patient coming in to the magnet, two measurements need to be made on the patient. First, a piece of tape should be placed on the thigh 21.3 cm from the middle of the calf. Placement of the tape should correspond to the bottom of the tape (closest to the floor) being at the desired distance. This will be used for placement of the patient in the magnet with the use of the laser. Upon insertion, as soon as the laser touches the tape, proper alignment can be assured. Second, the length from the middle of the patient's calf to the bottom of his/her foot. This measurement will verify that the foot flexor pedal is at the appropriate distance prior to the patient entering the scan room. Additionally, a piece of tape will be placed on the middle of the patient's calf and marked so as to note where the other measurements are stemming from, as shown in Figure 45. On the same part of the leg but on top of the patient's calf, a cod liver oil pill will be taped. This will be used for verifying correct patient placement during the  $^1\text{H}$  scan.





**Figure 45. Proper taping and placement of cod liver on patient's leg.**

The cod liver pill should be placed to the left and underneath the marked position on the tape.

After preparing the patient, he/she will be escorted into the magnet room and be shown where to sit. The procedure for inserting the patient's leg into the bore will be explained prior to actual placement. One person will help slide the patient's chair into position while another person will direct the patient's foot. The patient's leg will be inserted into the bore until the laser touches the tape on the patient's leg. Then the patient will be slid back slightly in order to insert/adjust the foot pedal to the desired height. Note: the height of the foot pedal should ensure that the patient's calf not lift off of the 3D printed receive coil piece. Instruct the patients to perform the exercise and scans while keeping his/her calf on the 3D printed piece. The strap on the foot pedal can then be tightened around the patient's foot. After verifying that the piece of tape on the patient's leg is at the laser line, have him/her do a few practice repetitions of the exercise protocol with no

weight in the bucket. Note: the patient may feel more comfortable if he/she is helped out of the magnet and then repeats the process of re-inserting his/her leg.

#### **A.1.9 Scan Protocol**

Note: Each patient will have an identification number and/or letter. The number 26 refers to the study number, NOT the patient number. Be sure to correctly identify the patient in the naming system. The first scan will use a long TR in order to ensure that all of the phosphorous compounds have had adequate time to fully relax. The remaining scans of the protocol will use the same shorter TR. No parameters will change between steps 2-4 below. Make sure that the number of PE loops is set to 2000 in the **Pulse Sequence\_Case\_structure.vi** to ensure that the followings scans are acquired at steady state. The **Pulse Sequence\_Case\_structure.vi** should not be stopped between steps 2-4 below.

1. The first scan will include 12 averages with a long TR of 30 seconds. Change the number of PE loops in the **Pulse Sequence\_Case\_structure.vi** to 13. Set the proper NB (2344) and capture counts (12) within the '**PCIe DAQ.lvlib:SetupandControl.vi**.' Within the **ReadandGraph.vi**, name the file name '**26\_patient\_id\_steady\_state.dat**.' Then click the "Acquire Data" button on the **ReadandGraph.vi** once until it turns green. After verifying the scan parameters ensuring proper patient placement in Step 8, click the "Acquire" button on the **Pulse Sequence\_Case\_structure.vi** to start the scan.
2. The remaining scans will be performed with 90 averages and a TR of 4000 milliseconds. Change the number of PE loops in the **Pulse**

**Sequence\_Case\_structure.vi** to 2000 and the TR to 4000 ms. Hit the “Initialize” button in the VI to update the parameters. Set the proper NB (17578) and capture counts (90) within the ‘**PCIe DAQ.lvlib:SetupandControl.vi**.’ Within the **ReadandGraph.vi**, change the name of the new data file to ‘**26\_patient\_id\_baseline.dat**’. Then click the “Acquire” button on the **Pulse Sequence\_Case\_structure.vi** to start the scan. After allowing 3 dummy scans to be recorded, click the “Acquire Data” button on the **ReadandGraph.vi** once until it turns green and data begins to store.

3. After the scan, change the name of the next acquisition to ‘**26\_patient\_id\_exercise.dat**’ in the **ReadandGraph.vi**. Then click the “Acquire Data” button on the **ReadandGraph.vi** once until it turns green.
4. After the scan is over, inform the MRSL or CTRLAL helper in the magnet room so that he/she can remove the weight so that tension is off of the patient. Quickly change the name of the next acquisition to ‘**26\_patient\_id\_post\_exercise.dat**’ in the **ReadandGraph.vi**. Then click the “Acquire Data” button on the **ReadandGraph.vi** once until it turns green.

**Note: This needs to be done as quickly as possible so that the physiological changes are seen in the recovery phase.**

5. After the scan, stop the LabVIEW program from running. Remove the patient from the bore and have him/her sit in a chair outside of the magnet room while the coils are changed out. Remove the  $^{31}\text{P}$  coils and insert the commercial  $^1\text{H}$  coil. Change the gradient cable from the back of the  $^{31}\text{P}$  custom transceiver to

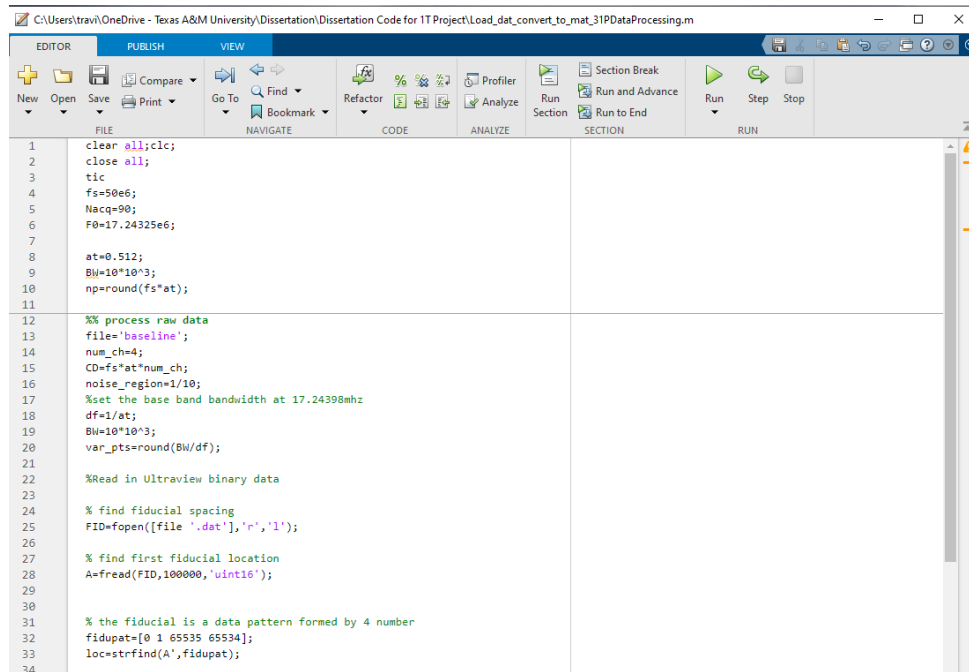
the ONI system. Then reposition the patient in the magnet using the laser and tape that was pre-marked on the patient.

6. Change the ONI system from “Overnight Mode” to “Full On.” Insert the patients ID, height, weight, and date of the scan into the ONI system. Then setup the scan protocol to “CTRAL 1-H Protocol 1” within the anatomy category of “Right Leg.” This should have one pulse sequence. The user will need to click on the #1 next to the name “CTRAL Scout Study.” Inform the patient that during the scan he/she will hear a slight humming noise and that it is perfectly normal. Let the patient know that a scan is about to be run and to remain still during the time of the scan. Run the pulse sequence. View the results by clicking the Series Number 1 in the bottom left-hand side of the screen and note the position of the slice where the fish oil pill is present in the image. Write down this number, as it will be used in the “CTRAL 1-H Protocol 2.”
7. Change the protocol to “CTRAL 1-H Protocol 2.” If the value of the center slice is much different than H 10.0 mm, change the center of the slice selection to the number that was found in the previous step. An alternate way of doing this would be to select the slice in the previous image in the image view and select the slice shift to be “Selected slice.” Ensure that the three marker dots (green, red, and yellow) are positioned in the center of the leg on the image. Inform the patient to remain still for 4:35 minutes and begin the protocol. Check the images after acquisition to ensure there aren’t any motion artifacts.

8. The images can be transferred off of the ONI system by clicking on the “Viewing” button at the top right of the page. Then click “Archive” --- “Transfer”. The Destination must be orthanc (orthanc). Find the study patient information by one of the search options. Highlight the images that you desire to export. Then click “Transfer.” The files will be sent to Dr. John Bosshard’s computer. The Dicom images can then be transferred securely to the CTRLAL group.

#### **A.1.10 Data Processing**

9. After the scans, open Matlab file ‘Load\_dat\_convert\_to\_mat\_31PDataProcessing.m’ to process the saved data, shown in Figure 46. You will need to copy the name of each respective file into the ‘file’ variable. After the file has run, it will save a .mat with the name of the file that was inserted. This .mat file can then be transferred to the CTRLAL group for further processing with the McMRSGUI.



The image shows a screenshot of a MATLAB script editor window. The title bar indicates the file path: C:\Users\travi\OneDrive - Texas A&M University\Dissertation\Dissertation Code for 1T Project\Load\_dat\_convert\_to\_mat\_31PDataProcessing.m. The editor has tabs for EDITOR, PUBLISH, and VIEW. The script content is as follows:

```
1 clear all;clc;
2 close all;
3 tic
4 fs=50e6;
5 Nacq=90;
6 F0=17.24325e6;
7
8 at=0.512;
9 BW=10*10^3;
10 np=round(fs*at);
11
12 %% process raw data
13 file='baseline';
14 num_ch=4;
15 CD=fs*at*num_ch;
16 noise_region=1/10;
17 %set the base band bandwidth at 17.24398mhz
18 df=1/at;
19 BW=10*10^3;
20 var_pts=round(BW/df);
21
22 %Read in Ultraview binary data
23
24 % find fiducial spacing
25 FID=fopen([file '.dat'],'r','l');
26
27 % find first fiducial location
28 A=fread(FID,100000,'uint16');
29
30
31 % the fiducial is a data pattern formed by 4 number
32 fidupat=[0 1 65535 65534];
33 loc=strfind(A,fidupat);
34
```

**Figure 46. Matlab script for post signal post-processing script.**

## A.2 Checklist for <sup>31</sup>P Protocol

- Proper placement of the coil system (6.3 cm from laser to face of transmit coil) (Step 1)
- Coil tuning verified – Physiological phantom placed 10.5 cm from laser to bottle cap (Step 1-2)
  - Receive elements tune to <-15 dB
    - L1 - \_\_\_\_\_
    - F1 - \_\_\_\_\_
    - L2 - \_\_\_\_\_
    - F2 - \_\_\_\_\_
  - Transmit tuning and function will be assessed with phantom calibration
- Cable attachment verified (Refer to Steps 3-4 in the Completed Protocol for images)
- Pure phosphoric acid phantom calibration test – bottle cap positioned 9 cm from the laser and parameters set according to Table 20. (Step 6) –

**Table 20. Calibration settings for phantom calibration test.**

UV Sample Clock Rate	50 MS/s
Attenuation	7 dB
Carrier Frequency	17.2398 MHz
Carrier Frequency 2	53
X shim	7
Y shim	40
Z shim	20
TR	4000 ms
PE Loops	1
Orientation	Transverse

- Iterate through shim settings until both Loops 1 & 2 have narrow linewidths and strong signals. Typical signal levels will be above the y-scale value of 1. Iterate to verify that the setting results in a signal maximum for both values.
- Power calibration should be swept from 6 dB of attenuation to 16 dB to verify 90 degree tip is achieved.

- Physiological phantom calibration tested – bottle cap positioned 10.5 cm from the laser – position of the phantom greatly influences SNR (Step 6). Software settings according to Table 21.

**Table 21. LabVIEW and Ultraview settings for averaging test.**

TR	4000 ms
PE Loops	17
Orientation	Transverse
Ultraview Settings	
Capture Count	16
NB	3125

- Use Matlab file:  
UVload\_spectfor31p\_4channels\_individual\_averages\_T.m, to process the data. The combined 4-channel SNR should be around 44.4 ( $c_1 = 24.5$ ,  $c_2 = 23.9$ ,  $c_3 = 18.8$ ,  $c_4 = 16.0$ ) The physiological sample PCr will decrease over time due to decay. Main objective is to verify performance of the Ultraview card and ensure SNR is similar among channels.
- LabVIEW parameters set and verified to those in Table 22 (Step 7)

**Table 22. LabVIEW and Ultraview settings for TR of 30 second experiment.**

TR	30000 ms
PE Loops	13
Orientation	Transverse
Pulse duration	205 $\mu$ s
Ultraview Settings	
Capture Count	12
NB	2344

- Foot flexor pedal properly set for the expected patient: \_\_\_\_\_ cm from laser to foot pedal (Step 8)



- Patient verifies that MRI consent form (Step 8)
- Markers have been properly placed on the patient: tape placed 21.3 cm on the thigh from middle of calf, fish oil pill placed on top side of the calf in the middle position, as shown in Figure 47 (Step 8)

Proper placement of cod liver  
oil pill.



**Figure 47. Proper placement of cod liver oil pill.**

- Patient properly placed in the magnet room (Step 8)
- Locked the patient chair into place
- Parameters set for the steady state acquisition and file properly named with patient ID number (Step 9 sub-section 1)
- The file name should be '**26\_patient\_id\_steady\_state.dat**'.
- Scan 1 run
- Changed the file name to '**26\_patient\_id\_baseline.dat**' and imaging parameters changed to 90 averages, TR of 4 seconds, PE loops to 2000, NB to 17578, and capture counts to 90, as shown in Table 23. (Step 9 sub-section 2)

**Table 23. LabVIEW and Ultraview settings for baseline portion of protocol.**

LabVIEW Settings	
TR	4000 ms
PE Loops	2000
Ultraview Settings	
Capture Count	90
NB	17578

- Run Scan 2
- Changed the file name to ‘**26\_patient\_id\_exercise1.dat.**’
- Run Scan 3
  - Average value at which patient was unable to complete exercise: \_\_\_\_\_
- Quickly, change the file name to ‘**26\_patient\_id\_post\_exercise.dat.**’
- Run Scan 4
- Stopped the LabVIEW program from pulsing.
- Escorted the patient out of the room.
- Changed the coil to the <sup>1</sup>H commercial coil. Switched the gradient coil cable from the <sup>31</sup>P transceiver hardware to the ONI system. Turned the ONI system on (Step 9 sub-sections 5-6)
- Inputted the patients ID number into the ONI scanner and found the proper pulse sequence underneath Anatomy: Right Leg, CTRLAL 1-H Protocol 1 (Step 9 sub-section 6)
- Clicked the “CTRLAL Scout Study.”
- Inserted the patient into the magnet and informed him/her that the system will make a noise during the scans.
- Locked the patient chair into place
- Run the pulse sequence
- Verified and wrote down the slice selection where the fish oil pill is in view.
- Changed to the “CTRLAL 1-H Protocol 2” protocol and verified the correct slice selection center of the first pulse sequence: CTRLAL Study FSE T1 Ax...
- Inform the patient that a scan is about to be run and to stay still for 4:35 minutes.
- Run the sequence.
- Verify the results before removing the patient.

**Table 24. Timing protocol for patient protocol.**

Steps	Time	Things to do	Parameters	Expected values
1.	2 mins	Inserting the coil		
2.	8 mins	a) Tuning the receive array b) Calibrating Tx Power	a) S11 b) Attenuation (dB)	a) <-15 dB, which should be tuned before the test
3.	15 mins	Pure phosphoric phantom and Physiological Phantom	See step 6.	Combined 4 channel SNR of 65±8.
4.		Install the pedal for contraction		
5.	5-10 mins	Put the volunteers' leg inside the magnet		
6.	6 mins	Scan steady state	TR = 30 s Avg 12 times	
7.	6 mins	Scan baseline	TR=4s Sampling rate 50MHZ/S Avg 90 times	See the screen shot of UV card GUI
8.	2 mins	Add weights to bucket		
9.	6 mins	Patient exercise	TR=4s Sampling rate 50MHZ/S Avg 90 times	
10.	6 min	Scan post-exercise	TR=4s Sampling rate 50MHZ/S Avg 90 times	
11.	5 min	Remove Patient and 31-P Coils. Insert 1-H Commercial Coil and switch gradient cable from 31-P system to ONI system		

**Table 24** Continued.

Steps	Time	Things to do	Parameters	Expected values
12.	3 min	Position patient with his/her leg in the same position as the 31-P scan		
13.	3 min	Run CTRL Protocol 1 scan to find the location of the fish oil pill. Use this slice location as the center of imaging for the CTRL Protocol 2 scans		
14.	4.35 min	Run CTRL Protocol 2 scan, which is an FSE T1-weighted scan.		
Total Time	76.35 min	Total Patient Time: 51.35 min		

## APPENDIX B

### MULTI-CHANNEL MAGNETIC RESONANCE SPECTROSCOPY GUI (MCMRSGUI) USER MANUAL

Summary: The McMRS GUI is a MATLAB-based graphical user interface that is utilized for evaluating and determining the proper multi-channel combination technique based on the spectra and additional information/scans that are available. A decision tree that is based on literature recommendations is available for the user to expedite the selection of the proper multi-channel combination between equal weighting, SNR weighting,  $S/N^2$ , WSVD, WSVD+Apod, and AOC. The program currently accepts Varian, .mat, and jMRUI text files as inputs. It can likewise export data files in .mat files for recording keeping of operations performed on data, or it can be exported in a jMRUI text format for quantification with jMRUI or other 3<sup>rd</sup> party software. It provides the user with several pre-processing steps: averaging, linebroadening, zero-padding, automatic/manual 0-order and 1<sup>st</sup>-order phasing, linewidth calculation, and viewing of spectra/free induction decays.

#### **B.1 Data Loading**

The GUI has two main menus for loading of data: preprocessing data (Figure 48-left) and multi-channel combination (Figure 48-right). For the methods that don't account for the phasing of the spectra (equal and SNR weighting), preprocessing of data to account for 0-order and 1<sup>st</sup>-order phases is necessary. Data can be loaded in via three different formats:

1. Matlab structure with the name “Starting.” The requisite fields and data types are shown in Figure 49. Note: Data is composed of free induction decay data in the matrix form (Num\_channels x Num\_acquisitions x Num\_datapts).
  2. Varian format with the .fid folder organization.
  3. jMRUI TextFile format with subsequent acquisitions labeled below (Figure 50).
- Note: this method requires separation of channel data into different files as this format can only display multiple acquisitions.

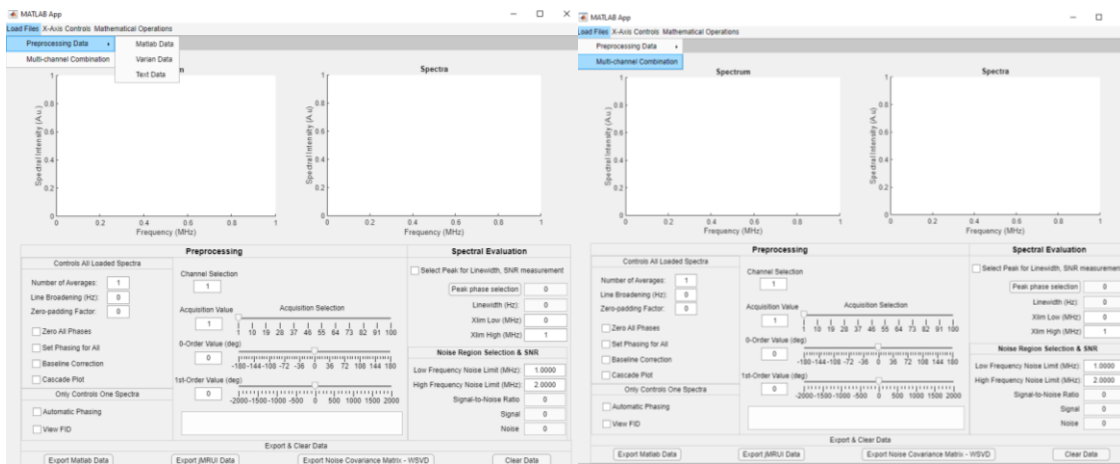


**Figure 48. Data input loading options for pre-processing and multi-channel combination options.**

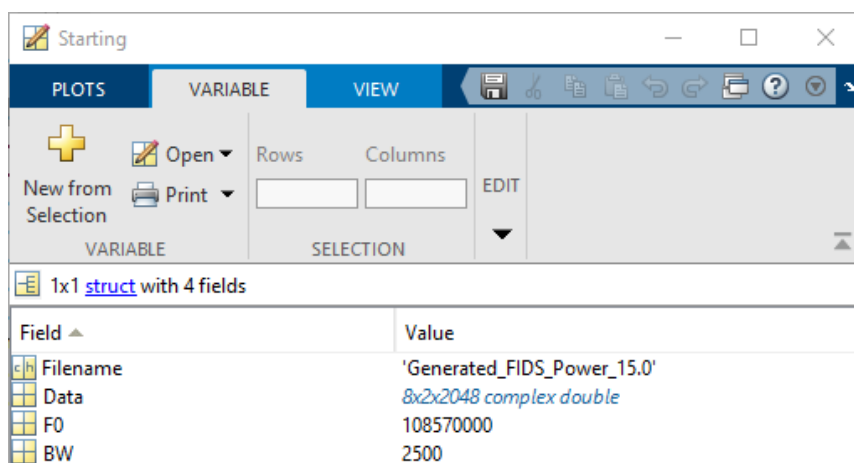


Figure 49. “Starting” structure used to initially load in data into the pre-processing menu or data-combination.

```

1  jMRUI Data Textfile
2
3  Filename: a.txt
4
5  PointsInDataset: 2048
6  DatasetsInFile: 2
7  SamplingInterval: 4.0000e-01
8  ZeroOrderPhase: 0E0
9  BeginTime: 0E0
10 TransmitterFrequency: 1.0857e+08
11 MagneticField: 0E0
12 TypeOfNucleus: -1E0
13 NameOfPatient:
14 DateOfExperiment:
15 Spectrometer:
16 AdditionalInfo:
17 SignalNames: AOC_No peak shifting combination_Acq_1;AOC_No peak shifting combination_Acq_2
18
19
20 Signal and FFT
21 sig(real)  sig(imag)  fft(real)  fft(imag)
22 Signal 1 out of 2 in file
23 4.8719e-02  1.0856e-04  4.9996e-02  -3.5887e-02
24 4.5780e-02  1.2542e-02  -5.9260e-03  -4.8040e-02
25 4.1559e-02  2.2677e-02  6.8303e-02  -6.1316e-02
26 3.2846e-02  3.0935e-02  4.9140e-03  -5.4880e-02
27 2.3149e-02  3.8705e-02  6.5260e-02  2.4192e-02
28 1.1215e-02  4.1442e-02  4.7465e-02  2.2246e-02
29 1.6106e-03  3.9560e-02  -2.0693e-02  3.8457e-02
30 -8.0924e-03  3.7110e-02  4.0934e-02  6.3387e-02
31 -1.7700e-02  3.0805e-02  4.8270e-02  -3.0141e-02
32 -2.3250e-02  2.3522e-02  3.7792e-02  1.0866e-01
33 -2.5667e-02  1.2050e-02  3.3093e-02  -8.7072e-02
34 -2.3950e-02  6.8929e-03  5.4783e-02  -2.0550e-02
35 -2.0589e-02  -2.5314e-03  4.0878e-04  -3.2301e-02
36 -1.5907e-02  -8.7015e-03  5.6513e-02  2.6439e-02
37 -7.3176e-03  -9.3210e-03  2.7653e-03  -1.2152e-02
38 -9.2471e-04  -9.4661e-03  -2.3529e-02  3.9240e-03
39 4.5122e-03  -8.5700e-03  7.7741e-02  -5.5003e-02
40 8.3108e-03  -5.2405e-03  5.7922e-02  -3.0334e-02
41 1.1310e-02  2.6905e-03  1.0950e-01  -2.6663e-02
42 1.0354e-02  8.0200e-03  5.2784e-02  1.6930e-02
43 9.4427e-03  1.3819e-02  1.5344e-01  -4.3939e-02
44 3.6808e-03  1.9484e-02  7.4505e-02  1.3286e-02
45 -6.1067e-03  2.2570e-02  2.8005e-02  3.1115e-02
46 -1.3417e-02  2.4680e-02  2.2622e-02  -3.0032e-02
47 -2.0455e-02  2.2739e-02  9.8131e-02  -9.3966e-02
48 -2.7771e-02  1.7837e-02  5.3568e-02  -2.1626e-02

```

Figure 50. jMRUI TextFile format for export option.

After the file is selected for the structure “Starting,” a dialog box will appear with the total number of channels for selection, as shown in Figure 51. Only one channel of data can be pre-processed at a time. Following the requisite pre-processing, the processed data will need to be saved through the “Export Matlab Data” button or the batch processing menu option, shown in Figure 52. This feature allows for the automatic or manual phasing to be set and quickly iterate through each channel.

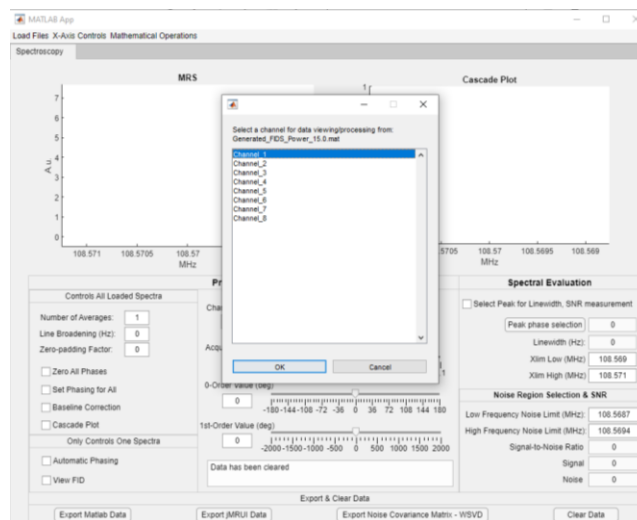


**Figure 51. Individual channel selection for pre-processing.**



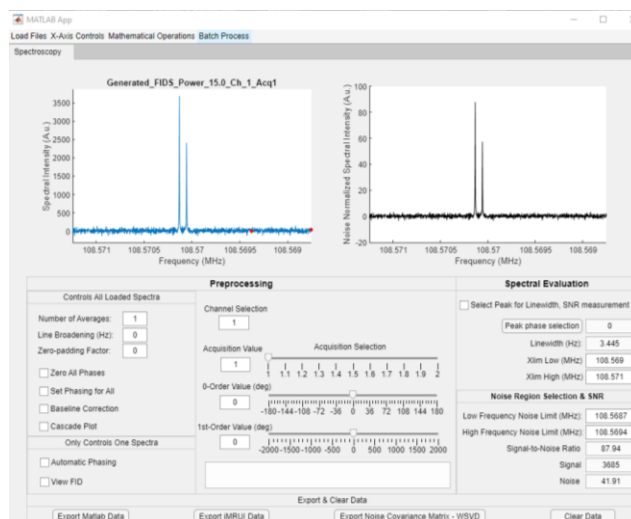


**Figure 52. Batch Process option becomes available after data is loaded into the program and will guide the user through a short series of questions.**

Pre-processing features:

1. Number of averages – for data that requires averaging of acquisitions to obtain a higher SNR. This option applies a sliding window average of length determined by the user.
2. Line broadening (Hz) – best if used for visualization purposes only, as this cuts off high frequency noise and signal content by applying a decaying exponential function to the free induction decay. A “matched-filter” or filter with the same linewidth as that of the peak of interest can be applied to evaluate the highest achievable SNR. This function is not recommended for spectral quantification.
3. Zero-padding factor – Zeros can be added to the end of the free induction decay in the time domain to interpolate datapoints in the spectral domain. This gives an

increased spectral resolution from the interpolation. Data sizes can quickly become large from this.

4. Manual and Automatic Phasing – Spectra can be manually or automatically phased using the bottom two sliders or the checkbox in the lower left of Figure 52. The automatic phase algorithm utilizes the maximum real peak as a starting guess for the correction of the spectra.
5. The FID for an acquisition can be viewed, or subsequent spectra can be plotted in a cascade plot for visual evaluation of trends and metabolite progression over time.
6. The peak linewidth, phase, and SNR are incorporated through the default maximum peak calculation or through user-defined regions for signal and noise.
7. The units of the x-axis can be switched between MHz and parts-per-million interchangeability for easier isolation of compounds from known chemical shifts. The options are highlighted in Figure 53.
8. File subtraction is an included feature, shown in Figure 54, for removing macromolecule signals or baseline roll. Note: the subtraction file must be a single acquisition (1 x Num\_datapts vector).

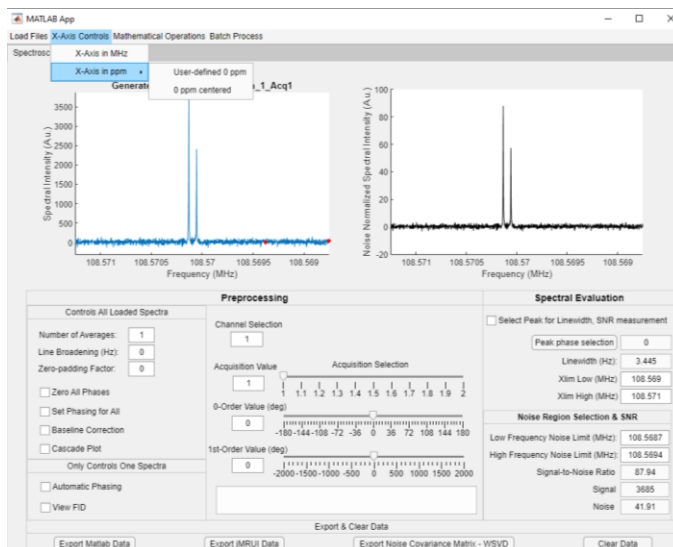


**Figure 53. X-axis adjustment options of MHz and parts-per-million.**

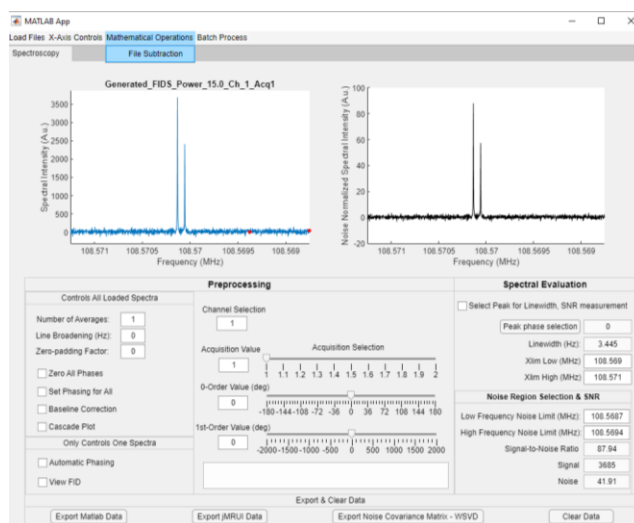


**Figure 54. The file subtraction function allows for a single file to be subtracted from a file to remove a macromolecule or baseline distortion.**

The multi-channel combination load file's tab allows either the Matlab structure "Starting" with multi-channel data ( $N_{\text{channels}} \times N_{\text{acquisitions}} \times N_{\text{data\_pts}}$ ) or the Matlab structure "Processed." The additional information stored within "Processed"

comes from the pre-processing step where peak information, such as the SNR and linewidth can be calculated. All other pre-processing options are stored within “Processed” to help with data traceability. The overall structure of “Processed” is shown in Figure 55. Note: If the structure “Starting” is loaded with this option, the user will be prompted for a region selection for both the noise and the signal content before the program goes back and calculates the SNR-related parameters.

Field	Value
Filename	2x1 string
Spectrum	2x2048 complex double
Time_domain	2x2048 complex double
Freq_axis	1x2048 double
F0_MHz	[108.5700;108.5700]
Linewidth_Hz	[3.4118;3.4118]
Peak_location_MHz	[108.5701;108.5701]
Peak_Maxes	[8.1842e+03;8.1842e+03]
SNR	[192.1178;192.1178]
a0	[0;0]
a1	[0;0]
Number_averages	1
Line_broadening	0
Zero_padding	0
Baseline_correction	0
Real_noise	[42.6000;42.6000]
BW_Hz	[2500;2500]
Noise_region_limits_MHz	[108.5688,108.5694]
Source_files	8x1 string
Channel_selection	[]
Operations	1x2 string

**Figure 55. Processed structure information that is stored by the program.**

## B.2 Data Combination Tree

Following successful data loading and/or preprocessing, the multi-channel MRS data will need to be combined in a manner based on the available SNR, additional information, and noise characteristics. The decision tree, shown in Figure 56, helps to guide users through the selection process. The program will prompt the user for a noise region that will be used for the calculation of the noise correlation. Evaluation of the data correlation levels for noise correlation between channels, shown in Figure 57, will help to determine if certain methods can be disregards based on their foundational assumptions. The  $S/N^2$ ,  $S/N$ , and equal weighting all make the assumption that the channels are not correlated.

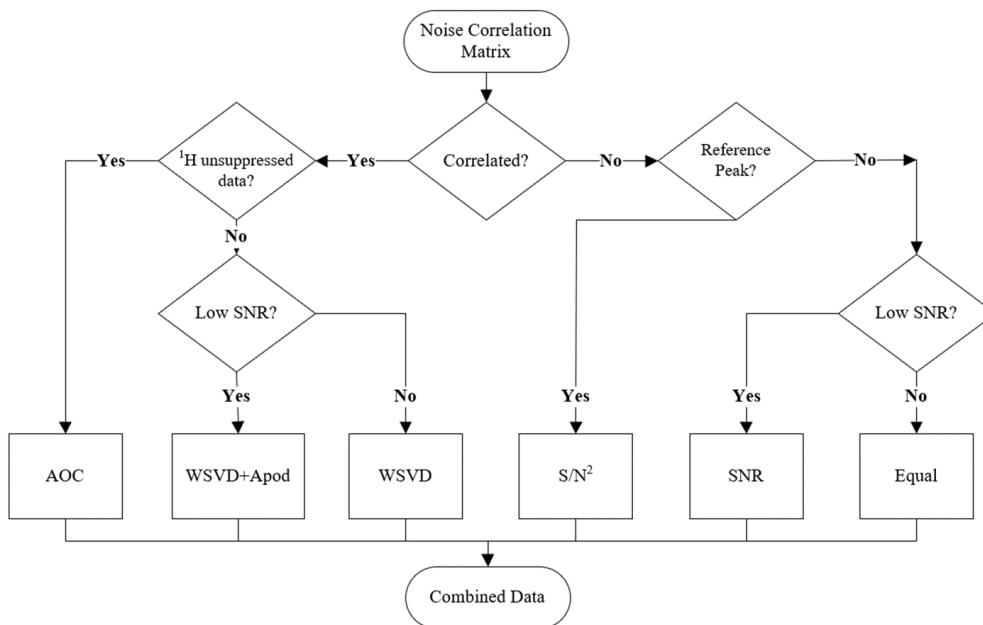


**Figure 56. Multi-channel spectroscopy combination method decision tree logic utilized within the McMRS GUI.**

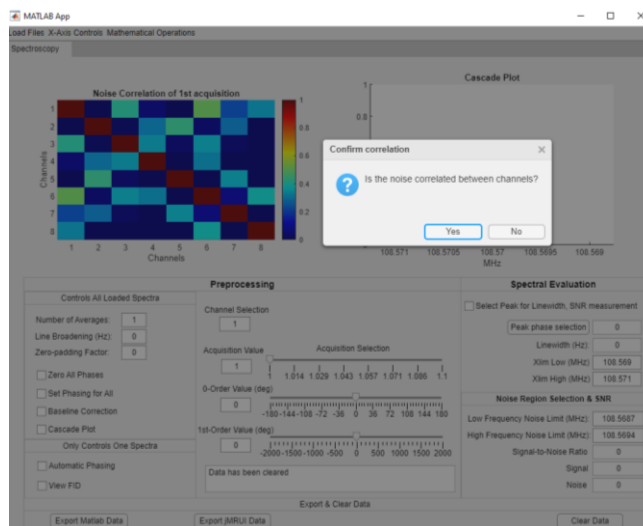


**Figure 57. Decision tree for determination of noise correlation between channels.**

Next, the program will prompt the user for any  $^1\text{H}$  unsuppressed data scaling factors, as shown in Figure 58. The unsuppressed water peak has a high SNR and better estimates the weighting coefficients between channels. Although this is not the sole factor in determining the complex weighting factors, it does play a significant role along with the noise correlation and covariance. Methods that utilize the  $^1\text{H}$  unsuppressed water scan typically better estimate the weighting factors at lower SNR when compared to their counterparts that don't utilize it. Alternatively, a reference peak that is ever-present within the spectra can be utilized for obtaining complex weighting factors.

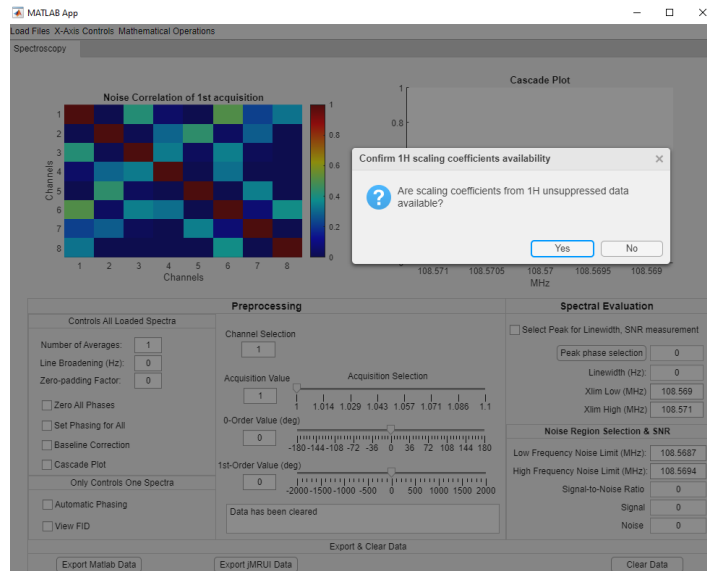


**Figure 58. Question dialog for determination of 1H data availability.**

At this point, the recommended combination has either been selected or a question about whether the combined spectra is expected to be low is asked. The WSVD+Apod method performs better at lower SNR values due to the application of linebroadening for the estimation of the weighting factors. On the opposite side of the decision tree, the SNR weighting performs slightly better than the equal weighting for this scenario.

### B.3 Data Exporting

As previously mentioned, the “Export Matlab Data” button, shown in Figure 59, exports a structure named “Processed.” This stores all the associated pre-processing values utilized. Data that has been combined will also be exported within “Processed” with the selection and associated additional files recorded within the structure. Alternatively, the “Export jMRUI Data” button, shown in Figure 60, will export individual acquisition data

within the jMRUI Textfile format from Figure 50. This data can then be loaded in to jMRUI for quantification.

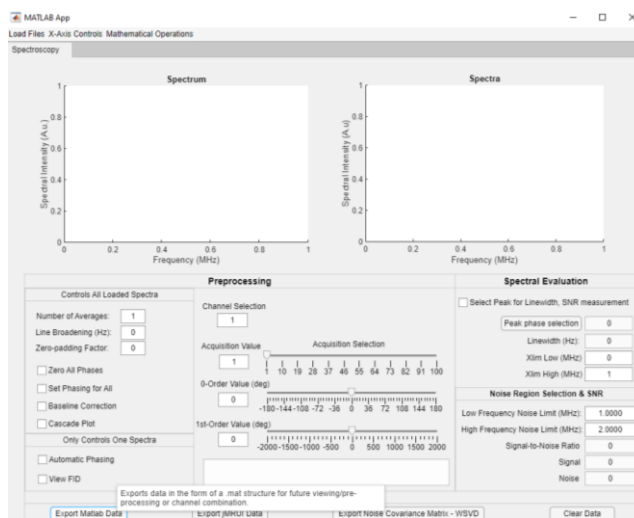


**Figure 59.** The "Export Matlab Data" button exports the loaded data and any associated pre-processing or combination steps for traceability.

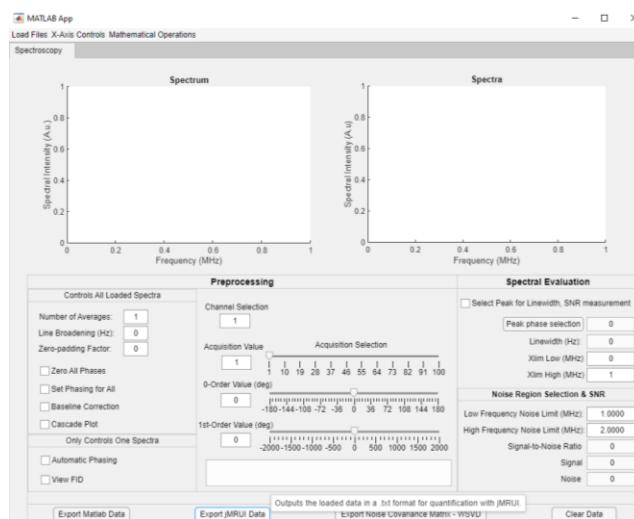


**Figure 60.** The "Export jMRUI Data" button exports individual acquisition data within a jMRUI Textfile format.



## B.4 Resetting of the Program

To reset the GUI, the “Clear Data” button, shown in Figure 61, clears the memory of the main structure used to pass data between functions and resets the graphs.

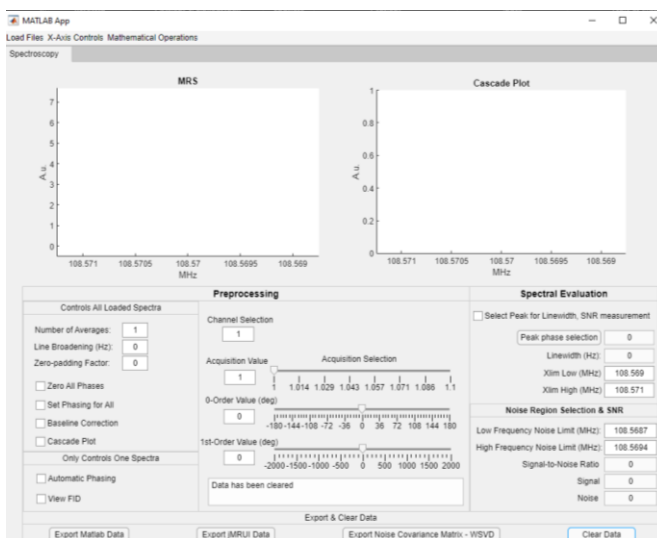


**Figure 61. The clear button cleans out the information stored within the app structure.**

## B.5 Accompanying Programs for Simulations

1. McMRSGUI\_MonteCarlo\_data\_simulation\_creation\_file.m – script utilized to create 8-channel data with correlated noise for distortion simulation.
2. McMRSGUI\_noise\_covariance\_creation\_file.m – script that can be utilized for creating a noise covariance file for the WSVD method. An example covariance matrix produced by the code is shown in Figure 62. Alternatively, a text file (.txt)

can be created with a single row of headers and then a comma-separated matrix of size Num\_channel x Num\_channel of the covariance values (Figure 63).

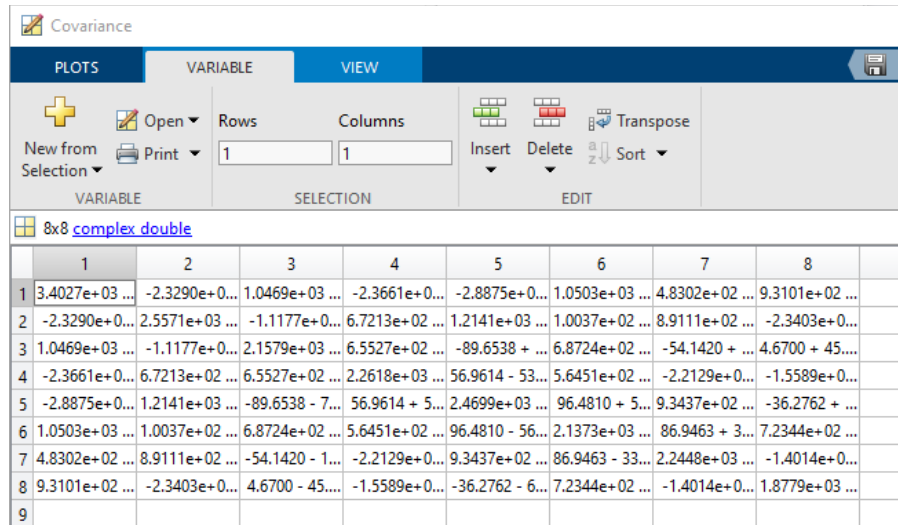


Figure 62. Example complex covariance matrix of size Num\_channels x Num\_channels.

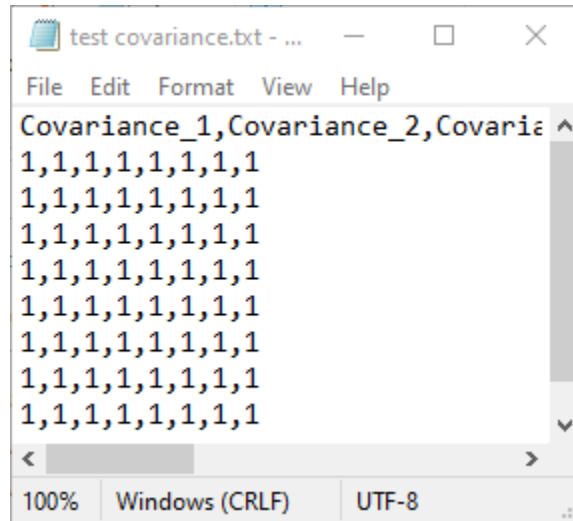


Figure 63. Example covariance matrix shown in the .txt format

- McMRS GUI\_Read\_jMRUI\_for\_S\_N2\_peak\_amplitudes.m – script that loads in jMRUI AMARES results that were saved as a .txt file. The fitted amplitude values are then saved in the proper format for use with the McMRS GUI for the S/N<sup>2</sup> combination method reference peak amplitudes. An example of the weighting factors is shown in Figure 64. Alternatively, a text file (.txt) can be saved with a single row header and then a comma separated (Num\_channel x Num\_acquisitions) matrix of the weights.

	1	2	3	4	5	6	7	8	9
1	18.0410	15.1910	14.0170	18.9510	14.2930	15.4510	17.6670	14.8530	13.1410
2	15.7820	6.5206	10.0710	5.8835	14.6770	3.9175	8.5795	14.6590	10.1250
3	9.8149	7.2697	10.9700	12.4720	5.7352	13.1130	7.2210	8.2904	11.6600
4	8.5154	8.0986	13.0110	5.1433	10.4550	12.4820	5.5371	10.1850	6.8355
5	8.1495	3.6212	10.6960	2.3340	15.3740	7.7800	7.4731	6.6382	9.6858
6	9.6366	8.8003	13.1470	5.2931	7.0825	7.1584	11.9160	10.3030	8.5732
7	16.9380	9.8690	18.5240	15.8350	12.9530	11.7150	16.6340	18.9690	14.6740
8	12.7860	17.4820	17.4050	13.7380	19.5000	11.6260	19.8280	14.9040	16.3860

**Figure 64. Weighting factors for S/N<sup>2</sup> method saved in a Num\_channel x Num\_acquisitions matrix.**